1 FLUORESCENCE DETECTOR

1.1 Fluorescence Detector System

1.1.1 Physics Objectives

The Auger fluorescence detector (FD) is expected to operate always in conjunction with the surface detector (SD). Its primary purpose is to measure the longitudinal profile of showers recorded by the SD whenever it is dark and clear enough to make reliable measurements of atmospheric fluorescence from air showers. The integral of the longitudinal profile is used to determine the shower energy, and the speed of shower development is indicative of the primary particle's mass. The hybrid detector will also have better angular resolution than the surface array alone, and this may be of value in studying tightly clustered arrival directions.

The longitudinal shower profile measured by the fluorescence detector provides a model-independent measure of the electromagnetic shower energy. The primary energy can be estimated as 10% greater than the electromagnetic shower energy, and simulations show that this estimate is systematically in error at most by 5%, regardless of the type of primary particles.

The FD requirements are driven by the required resolution in measurements of the atmospheric depth where the shower reaches its maximum size, X_{max}. Reasonable resolution is needed to evaluate the composition of the cosmic ray primaries. The resolution should be small compared to the (approximately 100 g/cm^2) difference expected between the depth of maximum for a proton shower and for an iron shower of the same energy. Moreover, the experimental resolution should not significantly increase the spread of values for any one component of the composition by itself. The width of the expected X_{max} distribution for any nuclear type decreases with mass A, and the distribution of iron depth of maximum values has an rms spread of approximately 30 g/cm^2. We will therefore require that the experimental X_{max} resolution be no greater than 20 g/cm^2.

An accurate longitudinal profile (achieving 20 g/cm^2 depth of maximum resolution) requires good geometric reconstruction of the shower axis. At large zenith angles, a small error in zenith angle causes a significant error in atmospheric slant depth. Averaging over the range of hybrid shower zenith angles (0-60^O) leads to a rule of thumb that an error of one degree in zenith angle leads to an error of 20 g/cm^2 in X_{max}. The angular resolution of the hybrid showers must therefore be significantly better than 1^O, since other uncertainties also contribute to the depth of maximum uncertainty.

The longitudinal profile of each shower will be well measured if the X_{max} is determined to an accuracy of 20 g/cm^2. In particular, the profile will then be well enough measured that the profile integral (proportional to the total shower electromagnetic energy) will contribute less than a 10% fitting uncertainty to the uncertainty in shower energy. Good energy resolution is therefore implicit in the X_{max} resolution requirement.

1.1.2 Detector performance

1.1.2.1 Aperture

Simulations have been performed to calculate the triggering aperture of the FD baseline design, with the arrangement of eyes shown later in this chapter (Figure 1.21). The simulations require a hybrid trigger *i.e.* triggers in at least one FD eye and at least two surface detectors. The design requirement is that the efficiency be near 100% at 10^{19} eV. This is achieved (Figure 1.1). In this figure it is clear that the FD will have a large stereo aperture at energies well above the threshold. Because we have access to SD timing information, stereo views are not vital for geometric reconstruction of the shower axis, but stereo views will assist in cross checks of our atmospheric transmission measurements. Also stereo triggers will yield some well measured showers (at large zenith angles or with cores outside the array) that are not recorded by the surface array.

There will be a large set of hybrid showers with energies below 10^{19} eV. The number of such showers will exceed the number recorded with energies above 10^{19} eV, even though the aperture is not that of the entire surface array. Such showers are measured by the FD only if they land within some radius of one of the eyes, where the radius is energy dependent.

The arrangement of four eyes at the Argentinian site reduces our dependence on a precise knowledge of light transmission through the atmosphere. The mean impact parameter from the closest triggering eye is 13 km at 10^{19} eV, compared with the effective Rayleigh scattering attenuation length (averaged over all light paths) of 19.5 km at 350nm.

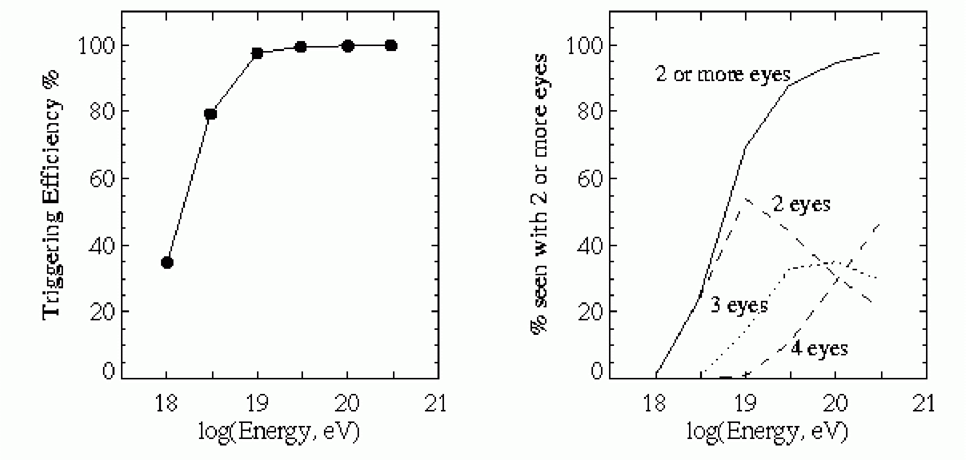

Figure 1.1 Left panel: The hybrid triggering efficiency as a function of energy for showers (with zenith angles less than 60^{O}) falling at random positions within the surface array boundary. At lease one fluorescence eye and two surface detectors are required to trigger. Note the acceptable aperture at energies lower than the nominal turn-on energy at 10^{19}eV. The triggering aperture can be obtained by multiplying the efficiency by 7375 km^2sr. Right panel: The fraction of events triggering more than one fluorescence station.

1.1.2.2 Reconstruction precision

As discussed above, the angular resolution of the detector must be small compared with 1^O, and the reference design will achieve an angular resolution of 0.5^O. There are two aspects of the angular resolution: the shower-detector plane determination and the angle of the shower axis within that plane. The shower-detector plane is determined by the set of pixels that see the shower axis. The need to resolve the shower-detector plane to better than 0.5^O has led to the constraint that the pixel size cannot be larger than 1.5^o in effective diameter. Determining the shower axis within the track-detector plane is done exclusively with timing information. The angular velocity of the shower front image moving through the FD field of view does not uniquely determine the shower axis. It does reduce the 2-parameter family of lines in the shower-detector plane to a 1-parameter family of possible axes. Each hypothetical axis makes a specific prediction for the arrival time of the shower front at each surface detector. The measured arrival times at one or more surface detectors thereby determines the correct shower axis. The need for good timing information is a primary reason for using sampling ADC electronics rather than simply recording a charge integral for triggering pixels. The ADC trace in each pixel allows an accurate determination of the time at which the shower front passed the center of the pixel. Analytic arguments and simulations show that time slices of 100 ns will yield the necessary timing accuracy to achieve the required angular resolution.

Simulation results on the expected performance of the hybrid detector are given in Table 1.1.

	Δdir (^{o})		ΔR_P (m)		$\Delta E/E$ (%)		ΔX_{max} (g/cm^2)	
Confidence limits	50%	90%	50%	90%	50%	90%	50%	90%
E=10^{18}eV	0.50	1.55	20	97	9.5	20.5	21	74
E=10^{19}eV	0.35	1.10	16	76	4.5	12.5	14	62
E=10^{20}eV	0.35	0.90	13	64	2.5	16.5	12	69

Table 1.1 Summary of hybrid reconstruction resolution for a single Auger eye, for events with zenith angles < 60^O landing inside the surface array boundary. If more than one eye triggers on an event we use information from the eye with the longest angular track length. The detector is optimized for energies above 10^{19}eV but acceptable reconstruction is expected at energies down to 10^{18}eV. The values of the parameter bracketing 50% and 90% of the error distribution is given. The table lists errors in the arrival direction, impact parameter, energy and depth of maximum. Only statistical errors are considered here.

1.1.3 Overview of the reference design

A prominent innovation in the Auger FD design is the adoption of Schmidt optics. The proposal to use a Schmidt diaphragm (aperture stop) came from Alberto Cordero at Puebla. The problem had been posed at a FD workshop at Utah in March, 1996: How can we achieve a uniform spot (optical point spread function) over a large field of view? It had been recognized that coma aberration is a significant analysis problem even for a 15x15-degree field of view, and we had a desire to reduce the number of telescopes by increasing the field of view of each mirror. The problem with coma aberration is not only the analysis inconvenience of treating pixels differently depending on their angle from the telescope axis. It is also a signal-to-noise issue. Coma spreads the signal to neighboring pixels. To recover all of the signal, one must include the neighboring pixels, and that increases the noise. The Puebla proposal was to use the Schmidt diaphragm to eliminate coma aberration. The telescope optics becomes almost completely spherically symmetric, so pixels far from the telescope's axis are equivalent to pixels on the axis.

There are numerous advantages of the Schmidt optics design:

(a) Clean and simple analysis, since all pixels are the same.

(b) Wide field of view (30^o x 30^o) requiring fewer telescope units.

(c) Small aperture, so simpler and more reliable shutters.

(d) Fewer telescopes of compact design allows housing in one building.

(e) The diaphragm window can be covered by the optical filter, so we gain

- clean mirrors and camera (much less desert dust)
- temperature stability by interior heating and cooling
- the possibility of humidity control
- less fire risk since only UV light reaches the mirror
- the option of an interference filter, since there is a smaller range of incident angles at the filter

It should be noted that the motivation for Schmidt optics is primarily to make a superior detector that is free of coma aberration. There is not a great cost advantage. Although the number of telescopes is reduced by ¼, each has roughly 4 times greater mirror area. (The light collecting area is defined by the diaphragm which is small compared to the mirror when the field of view is large.) The Schmidt optics requires a curved focal surface (spherical symmetry). This is more difficult (and expensive) than a flat focal surface. We end up with one-fourth as many telescopes, but each is much larger and less simple. Having said this, it should also be noted that the reduced number of telescope units does save on certain costs which scale with the number of units. These can include calibration equipment, high voltage supplies, electronics crates and processors, conduits and wiring, etc. The overall cost of the detector is not greatly changed by the Schmidt optics. The number of pixels is the same, and it is the invariant pixel costs (PMT and pixel electronics) that are the major expense in either case.

The Schmidt optics is only the front end of an exciting and innovative fluorescence telescope design. We have designed a camera with excellent light collection efficiency, achieved by using *mercedes star* reflectors between photomultipliers. A new electronics system has been developed with a large dynamic range and 10MHz ADC sampling, to provide good quality pulse timing and amplitude information, and futhermore a flexible and very efficient hardware trigger scheme. We are also pioneering new techniques in detector calibration and atmospheric monitoring, two difficult tasks that are crucial for accurate shower profile measurements.

1.1.4 Detector System

1.1.4.1 Design Specifications

1.1.4.1.1 General Considerations

One observatory eye with a field of view of 180° in azimuth and 30° in elevation is built from 6 telescopes each covering 30° x 30°. To achieve this large field of view with a reasonable effort and good optical quality the layout of a Schmidt telescope is adapted. The elements of a telescope are the light collecting system (diaphragm and mirror) and the light detecting camera (a PMT array).

The detailed design of the optics contains a large spherical mirror with radius of curvature R=3.4m, having a field of view of 30° x 30° with a diaphragm at the center of curvature whose outer radius is 0.85m. These parameters are the result of signal/noise calculations for extensive air shower events at the experimental threshold, taking into account the amount of night sky background at the southern site of the Auger project and the obscuration by the PMT camera and its support structures.

The diaphragm will eliminate coma aberration while guaranteeing an almost uniform spot size (circle of least confusion) over a large field of view. With the above configuration the spot diameter (containing 90% of the mirror-reflected light) is kept under 0.5° [1, 2].

The sensitivity of the telescope can be improved by enlarging the diaphragm to an outer radius of 1.1m. This choice determines the light collection efficiency (which is nearly doubled) and the size of the mirror surface, about 3.8 x 3.8 m (square with rounded corners). The corresponding increase in spherical aberration can be fully compensated by a corrector lens annulus covering the additional area between $0.85\text{m} < r < 1.1\text{m}$.

This lens is connected to the wall of the building by an adjustable mechanical structure (aperture box) which keeps out the weather and stray light. This box also holds an optical filter transmitting in the nitrogen fluorescence wavelength range (300 to 400 nm) and blocking most of the night sky background. In addition, it acts as a protective window on the outside of the diaphragm.

Based on the considerations given above, we have set Rc =3.4 m. The (curved) focal surface is at approximately half that distance from the center of curvature, so the camera edge has a length of 1.70 x 30 ($\pi/180$) metres. The camera size and shape is therefore about 0.9m x 0.9m square.

Each pixel in the light detector should have a field of view small enough to measure accurately the light trajectory on the detector surface but large compared to the spot size. A diameter of about 1.5° (26.2 mrad) is a good compromise. It corresponds to a linear size on the detector surface of about 0.0262 x 170 cm = 4.5 cm, which can be easily matched to commercially available PMTs. The image on the camera surface has finite dimensions due to two effects: spherical aberration and blurring due to mirror imperfections or alignment inaccuracy. Blurring and additional light from the outer diaphragm area with the corrector annulus should not substantially increase the spot size as determined primarily by spherical aberration.

1.1.4.1.2 Aperture System

1.1.4.1.2.1 Optical Filter

The idea of an optical filter is to transmit most of the fluorescence signal in the near-UV while blocking other night sky background to which the PMTs are sensitive. A good reference for detailed considerations of filter optimization is the article by J.W. Elbert [3]. There you can find a tabulation of the nitrogen fluorescence spectrum, a plot of the PMT spectral response, the night sky spectrum at Dugway and Akeno, HiRes filter transmittance as a function of wavelength, etc. The night sky spectrum should be measured at Pampa Amarilla for a rigorous analysis applicable to this project.

The signal spectrum of interest for filter design is not the emitted nitrogen fluorescence spectrum. That is the signal spectrum for nearby showers whose light is not affected by atmospheric attenuation. Nearby showers are sufficiently bright, however, and will be no problem for FD measurements regardless of the filter optimization. The filter should be designed to maximize S/N for distant showers. Because Rayleigh scattering is strongly wavelength dependent (inversely proportional to the 4th power of wavelength), and aerosol attenuation is also stronger at smaller wavelengths, the nitrogen fluorescence spectrum is significantly "reddened" by atmospheric transmission from a distant shower. A good filter should transmit most of this reddened spectrum while attenuating as much as possible the sky background light.

We can adopt here a procedure for comparing the relative merits of competing filters along with some specifications for the required performance. The test procedure will use the XP3062 PMT that has been proposed for use in the Auger telescopes. Any filter transmittance measurement is here taken to be simply

(PMT response with filter)/(PMT response without filter)

The circumstances of our experiment must be taken into account. To verify that a filter has good transmittance to the nitrogen fluorescence spectrum, we should use a nitrogen flashlamp. To verify that it has good transmittance for a reddened nitrogen spectrum, we should use a narrow band filter to check that the strong 391nm fluorescence line has high transmittance. The other experimental test is then to check that the filter has a relatively low transmittance for the night sky (preferably tested at Pampa Amarilla).

Our proposal for the filter specification is the following:

(a) Transmittance > 0.80 at 391nm

(b) Transmittance > 0.72 for the full nitrogen spectrum

(c) R > 1.65, where R=(nitrogen transmittance)/sqrt(sky transmittance)

(d) These specifications to apply to all relevant incidence angles (0-21^{O})

Elbert found that the optimal filter for the HiRes aperture would be one that cuts off abruptly at 400nm (preserving most of the reddened nitrogen spectrum while significantly reducing the background). About 10% of the nitrogen spectrum photons are above 400nm, so the second condition above might mean 80% transmittance below 400nm and zero transmittance above 400nm, for example.

The ratio of transmittances R (in the third condition above) is a figure of merit that measures the increase in signal-to-noise effected by the filter. The numerator scales the signal and the denominator gives the scaling of the noise. (For distant showers, the signal is small and the noise is primarily the square root of the sky background.) The HiRes filter gives R slightly greater than 1.65, so the third condition is achievable. Comparing competing filters is done by comparing their figures-of-merit R, assuming the filters already satisfy the first two transmittance requirements. Relatively small improvement in R can be valuable. For example, increasing S/N by 10% would be the equivalent of increasing the collecting area by 21%, which is an expensive alternative. It is therefore worthwhile exploring methods for increasing R.

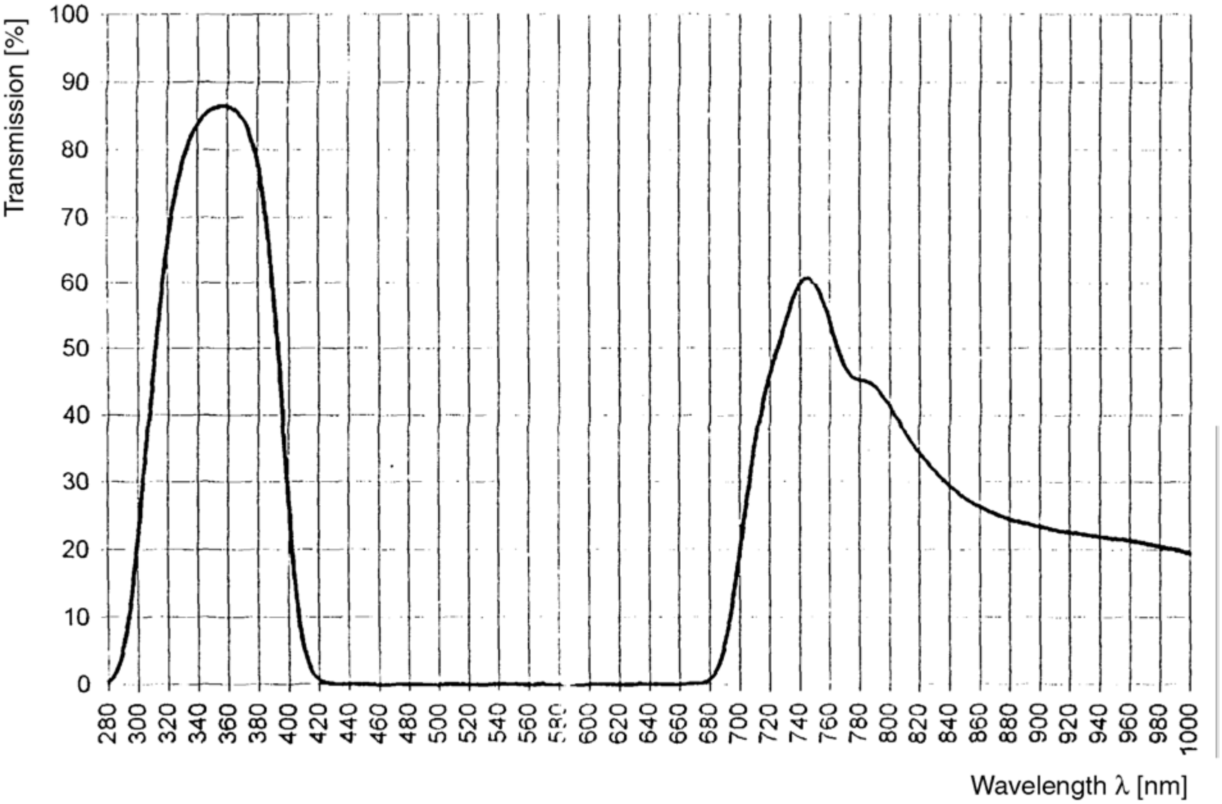

Figure 1.2 The transmission for Mug-6 glass, from 280 to 1000nm. The peak transmission is approximately 86% at about 355nm.

Such a study of filter requirements was performed [4] and recently extended focusing on the detection of fluorescence light above 350 nm - that light dominating the reddened spectrum from distant showers. Comparing samples of different absorption filters it was found that an adequate, cost-effective choice for the filter is Mug-6, manufactured by Schott-Desag. The transmittance spectrum of Mug-6 is given in Figure 1.2. It covers a wavelength range that overlaps well with the Nitrogen spectrum. With the techniques described in [4] the transmittance and the figure of merit R (as defined above) were measured for the region of the Nitrogen spectrum above 350 nm. The transmittance (for a ~3 mm thick sample) was measured to be 0.73 ± 0.03 and the figure of merit, R = 2.02 ± 0.06.

Filter specifications also need to include mechanical criteria and longevity requirements. The reference design calls for the optical filter to be the telescope window, exposed to outdoor temperatures and wind on one side, controlled indoor conditions on the other side. The recent progress in the development of construction techniques makes the corrector ring option (see section 1.1.5.1) appear very promising. The circular filter aperture should in this case be increased from the 1.70 m in the reference design to a 2.10 m diameter, making the construction of an adequate mechanical structure even more challenging.

The thickness of the filter should be chosen to optimize light transmission without losing the mechanical strength required. The use of tempered glass is recommended. The number and size of glass sections to cover the aperture should be chosen keeping in mind a compromise between the desire to make many pieces to increase the mechanical strength and the requirement of minimizing joins that affect the aperture obscuration. The fraction of area obscured should not exceed ~5% of the total aperture area.

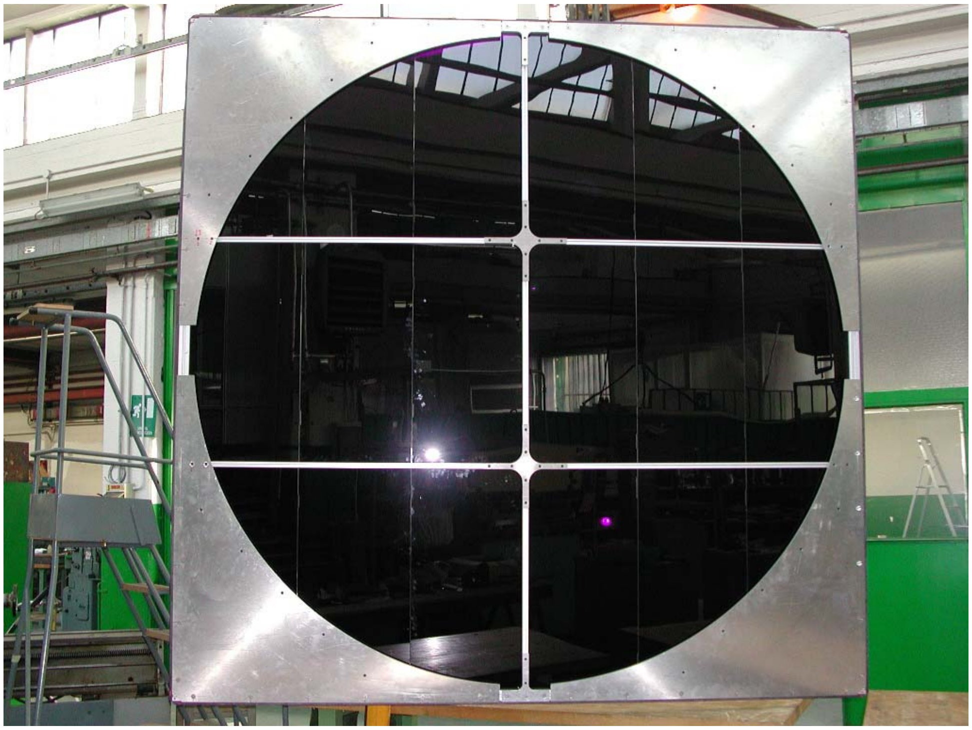

Figure 1.3: Filter prototype for the bays 4 and 5 at Los Leones.

The surfaces of filter sheets should be of sufficient quality not to introduce significant deterioration of the spot size. It is required that, with otherwise perfect optics, the effect of filter surface imperfections should not cause an increase greater than 5% in the radius of the circle containing 95% of the image light, for angles of incidence < 21^{O}.

The design of the mechanical support structure must be validated with a finite-element calculation to check for deformations under the structure's own weight and of external forces realistically mimicking those expected on the site.

The two prototype filters presently installed on bay 4 and 5 (Figure 1.3) at Los Leones were built out of 80 cm x 40 cm sheets of tempered Mug-6 glass. The thickness of each sheet is 3.25±0.02 mm. They fulfil most of the above requirements; however the field test is essential and will provide valuable lessons on what additional measures may be required to build a structure capable of surviving the 20 years of the experiment.

1.1.4.1.2.2 Corrector Ring

A corrector ring is being considered as an addition to the baseline design. One such ring is under test at the prototype system at Los Leones (Figure 1.4). This section is currently being written. For an earlier discussion, please see section 1.1.5.1.

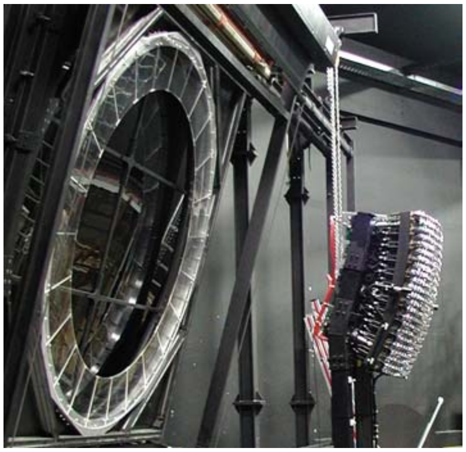

Figure 1.4 Prototype corrector ring in position at Los Leones.

1.1.4.1.3 Mirror System

1.1.4.1.3.1 Guidelines

The amount of light reaching the PMT array depends on :

(a) the coverage of the mirror surface which will have to be segmented,

(b) the reflectance of the coating,

(c) the transmittance of the filter in the nitrogen fluorescence band (300 to 400 nm)

The specifications are a cost effective solution to the problem of obtaining large light collection with small spot size, and uniformity over a large field of view. For all elements a major constraint will be the long operating time of the detector (about 20 years).

1.1.4.1.3.2 Mirror Segments

(a) **Segment shape:** a square shape optimizes the coverage of the quasi-square mirror surface (with less wasted surface at the perimeter of the mirror). Hexagons are favored from the point of view of mechanical stability of the corners of the segments. Both shapes will be used in different telescopes of the Auger fluorescence detector.

(b) **Tessellation:** from a logistics point of view it is desirable to deal with just a few mirror segments, all equal in shape. The maximum size of the segment that can be cheaply and easily built depends on the choice of the technique used in producing the mirrors, and is different for the two techniques chosen.

A tessellation easily realized with the proposed technique of diamond milling of aluminum alloy plates consists of 36 mirror segments of about 0.65 x 0.65 m^2 and 3 different (not exactly square) shapes. It will map the surface almost without cracks. The alternative solution of ground and polished glass mirrors calls for 60 hexagonal elements in 4 different shapes. Both methods can ensure:

i. Tolerance on the variation of the mean radius of curvature, R_c segment-to-segment: ±17mm, measured with an accuracy of ±1mm.
ii. Tolerance on mirror size (cutting inaccuracy): ±1 mm or better.
iii. Mirror substrate quality: 90% of the mirror-reflected light from the center of curvature returns to within 0.5 cm of the center of curvature.
iv. Quality of reflecting surface: the reflectance of the finished surface is about 90% for wavelengths between 300 and 400 nm.

Present plans are to build about 60% of the telescopes with aluminum mirrors and 40% with glass mirrors.

1.1.4.1.3.3 Aluminum mirrors

The production of mirror elements from solid aluminum alloy sheets is done in several steps. First a cast-aluminum backing with an approximate spherical shape is milled to an effective thickness of 18mm and the final radius of ~3400mm. Next, in a separate procedure, a 3mm AlMgSi0.5 sheet is glued to the backing with an appropriate epoxy using high temperature (150^{O} C) and a high-pressure piston.

Figure 1.5 An aluminum mirror element mounted on an optical test stand for the determination of the effective optical properties – radius of curvature and the intensity distribution of the reflected light.

Thereafter, the edges of the segments and a central hole are milled precisely. The final milling with high quality machines and diamond tools is done in a specialized commercial factory. Back in the Karlsruhe IK, the mirror surface is cleaned and finally protected by electrochemical anodization following a procedure developed by the MAGIC collaboration. A mounting ring flange is glued to the back and the mirror element is put on an optical bench for final testing.

The testing is performed using a point-like (0.2mm or 1mm diameter) light source. This is a blue LED (470nm) or a UV LED (370nm) with diffusers together with a reflective screen near the center of curvature of the mirror. A 12-bit cooled CCD camera is used for the measurement of the intensity distribution of the reflected light. The halo distribution can be measured with high sensitivity when the main intensity is put through a 10 mm diameter hole in the screen.

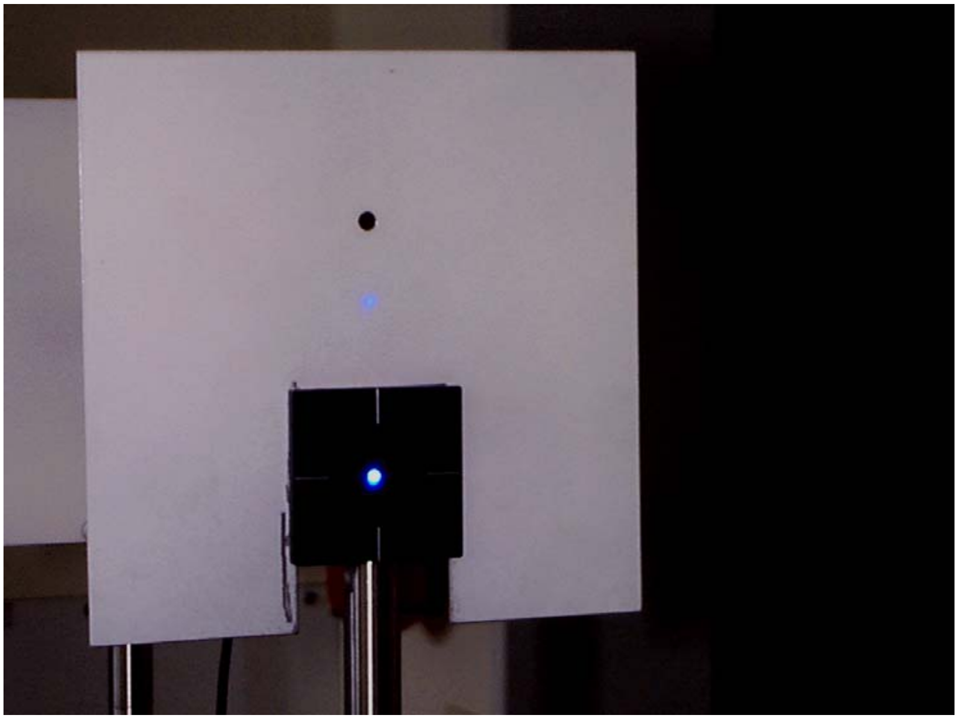

Figure 1.6 A "point-like" light source (LED at 470nm), and the spot of reflected light from a mirror segment. The screen is positioned close to the effective radius of curvature. The hole on the screen has a diameter of 10mm.

In the Engineering Array phase about 40 mirror elements were produced by diamond milling techniques using different methods of backing production. The tests clearly showed that the mirror optical properties easily match the specifications for the Auger FD telescopes. The mechanical stability of the segments has been improved considerably during this prototyping. The method of "hot" gluing will further improve the long-term behaviour of the mirrors. Simple mirror cleaning procedures need to be developed because of the large amount of dust in the telescope bays at Los Leones.

1.1.4.1.3.4 Glass Mirrors

The design of the glass mirrors stems from expertise and technological capabilities of the Joint Laboratory of Optics in Olomouc (JLO) and also from computer simulations of the influence of gravity, tilt and temperature changes on the geometrical shapes of mirrors. Other considerations taken into account are naturally the cost of production and the number of mirrors to be produced.

The rough shape of the mirrors is obtained by pressing molten glass into a mould. Moulding is done in a professional glass factory using a material with a trademark name of SIMAX. It is a borosilicate glass of a type similar to PYREX, with high tensile and bursting strengths (35 – 100 N mm^{-2} and 500 N mm^{-2} respectively), a low coefficient of thermal expansion (3.3 $x10^{-6}$ K^{-1}), and good machining properties using standard optical technology. The glass is melted and homogenized in an electric tank furnace. Liquid glass with a temperature of about 1,450^{O}C is injected into the mould. The pieces are pressed one by one under a mass of 15,000 kg. After pressing, these intermediate products are annealed in an electric conveyer furnace.

Figure 1.7 Mirror milling at JLO in Olomouc.

The semi-finished products are machined at JLO in Olomouc. The machining of mirrors is based on standard operations commonly used in the optical industry (cutting, drilling, milling, grinding and polishing). However, all the operations had to be adapted for producing these large and thick mirrors. The final mirror shape is a hexagon, cut from a circular intermediate mirror. The mirrors used for the FD Engineering Array have a size defined by a circumscribed circle of radius 500 mm. In order to decrease the number of mirror segments required and thus to ease the production burden, the final mirror design has a circumscribed circle radius equal to 630 mm. All the technological operations remain valid and the number of mirror segments per telescope decreases from 85 to 60. The change of radius also led to simpler tessellation (with 4 distinct shapes).

The next step in mirror production is the deposition of a reflecting layer. Before that, multiple washing and cleaning of the mirror surfaces is performed. A protective silicon oxide (SiO2) layer covers the reflecting aluminium layer. Standard vacuum equipment with an electron gun is employed for the deposition process.

The mirrors are subjected to rigorous control of the machined surface quality, and their geometrical and optical parameters. Final measurements are made of the reflectivity and the size of reflected light spot. For these operations a monochromator and a UV-sensitive camera are used.

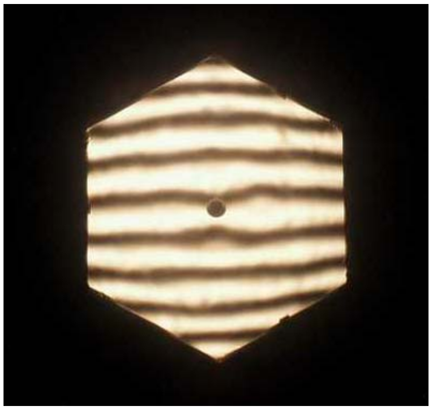

Figure 1.8 Ronchi test of a glass mirror surface. Parallelism of the fringes shows the regular spherical surface of the mirror. Irregularity in the shape would be seen as irregularity of the fringes.

1.1.4.1.3.5 Segment Alignment

Each mirror segment is supported by an adjustable mount clamped to the mechanical support structure. The mount is connected to a ring flange glued to the back of the mirror segment.

Two adjustment screws and a spring act together on a central ball bearing. This type of mount has been successfully tested in the prototype mirror system and the design was improved and simplified further taking into account all the experience gained.

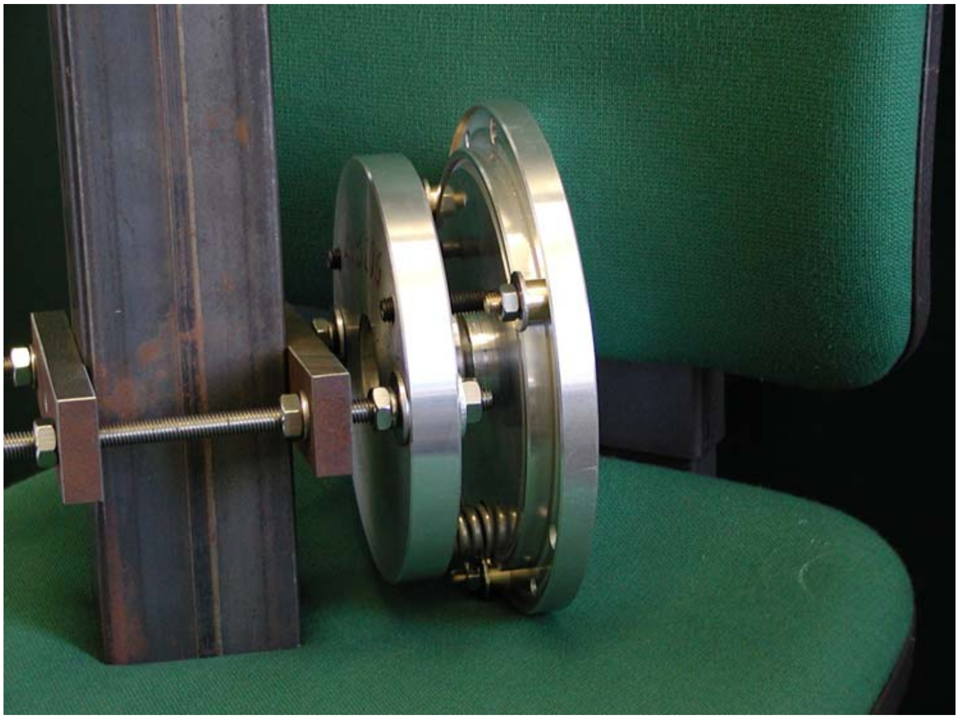

Figure 1.9 Photograph of a new prototype of the mirror mount to be used with both the aluminum and glass mirrors.

Specifications of the mounts include:

(a) Degrees of freedom and range of the adjustable variables: position along the mirror segment axis (±1 cm), polar angle (±5^o), and azimuth angle (±5^o)

(b) Adjustment and tolerance of position along axis: the tolerance of adjustment in the radial motion toward the center of curvature corresponds to a 1mm image shift. The precision achieved on the longitudinal position of the mirror segments is about ±1 mm.

(c) Adjustment and tolerance of azimuth and polar angle: one turn on the adjustment screw corresponds to 20 mrad, shifting the image by about 34 mm on the camera surface. The tolerance required (and easily achieved) is ±1mm. This must be compared with the 15 mm image size.

(d) Tolerance on the positioning of the adjustable mount on the main mechanical structure: in the plane tangent to the mechanical structure ±1mm, with full rotational freedom of the mirror segments.

(e) Mirror surface coverage: assume a tessellation without cracks. To guard against interference between adjacent mirrors coming either from differences in the radius of curvature or from lack of accuracy in cutting, a gap ($\delta_x = \delta_y = 4$mm) is allowed between mirrors. Central holes on each mirror segment proved to be useful during element production and mounting. In addition, for the aluminum mirror elements all corners are cut to enable easy access to calibration light sources on the mirror surface. All these losses add up to less than 2% of the mirror area.

The procurement and production of these mounts will be shared by several groups. Krakow will provide about 10% to 20% of the total, Karlsruhe (with the help of Prague with the mechanical production and assembly) and Puebla will together take care of the remaining mounts.

1.1.4.1.3.6 Mechanical Structure

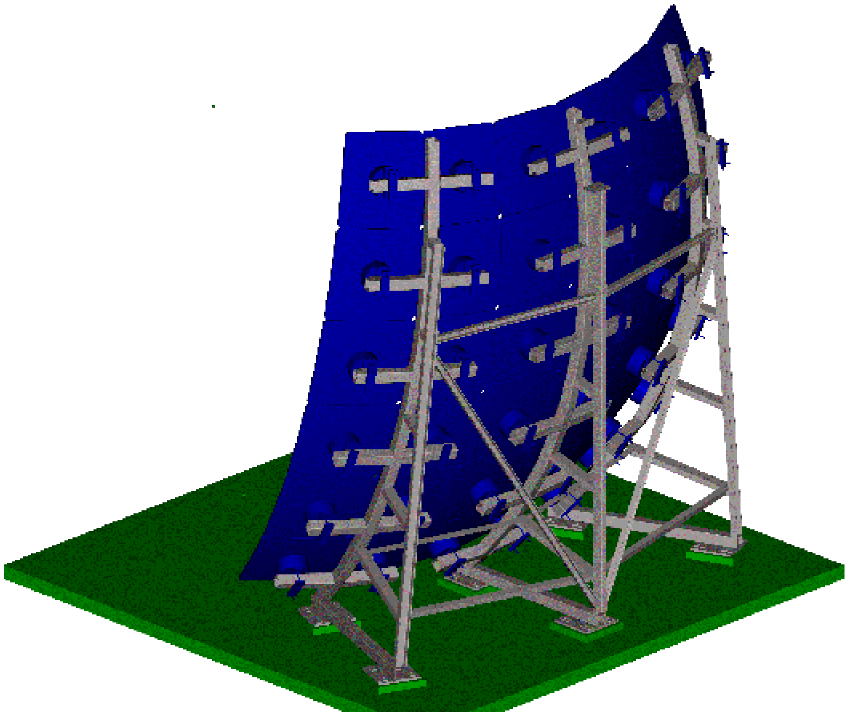

Figure 1.10 The new design of the support structure for the 36 aluminum mirror system for the Los Leones eye. The structure foreseen for the 60 glass mirror telescopes for the Coihueco eye is very similar.

The adjustable mirror mounts are clamped to a simple mechanical structure built from three nearly identical stands (80mm square steel tubes rolled to a radius of about 3.5m) bolted to the ground and connected by cross bars. These structures are aligned to about ± 10mm during installation.

The prototype system showed sufficient stability against external forces. A person climbing on different parts of the support after the mirror alignment produced an image shift of less than 1mm at the focal surface which was completely reversible. The new design will be as stable but easier to mount and align in the bays.

The top of each stand allows the mounting of a small pulley for an easy handling of the mirror elements during mirror installation.

The support structures for all telescopes will be provided by Karlsruhe.

1.1.4.1.3.7 Adjustment tools

To mark and identify the center of the mirror sphere and the diaphragm, a central reference point is mounted in front of the aperture box. It consists of a strong mechanical support which is bolted to the floor with a precise reference plate on top. The removable upper part of the reference point unit fits precisely to this plate and can support various adjustment tools.

A theodolite at the reference point is used for the initial determination of the geometry of the telescope system. After setting the mirror support stands, the position and rough orientation of the mirror mounts on the support structure is determined optically. The distance of each mount from the center of curvature is then measured by a laser distance meter (DISTO) on the reference point and mechanically adjusted to an accuracy of ± 1mm.

A mechanical system coupled to the reference point is used for the alignment of the position and the orientation (inclination) of the diaphragm system and corrector lens annulus. An accuracy of ± 2mm in position and ± 2mrad in orientation is easily achieved. In a similar way the position of the camera body is defined and set with a precision of about ± 1mm.

After the mounting of the mirror segments, a laser pointer on the reference point is used for the precise optical alignment of the axes of all mirror elements. The position of the returning laser beam can be determined to ± 1mm corresponding to an alignment of the optical mirror axis of better than 0.2 mrad.

All these tools have been tested very successfully during the installation of the prototype bays and the first two telescopes. Karlsruhe will provide the reference points and adjustment tools for all further telescopes with no more than minor changes in the design.

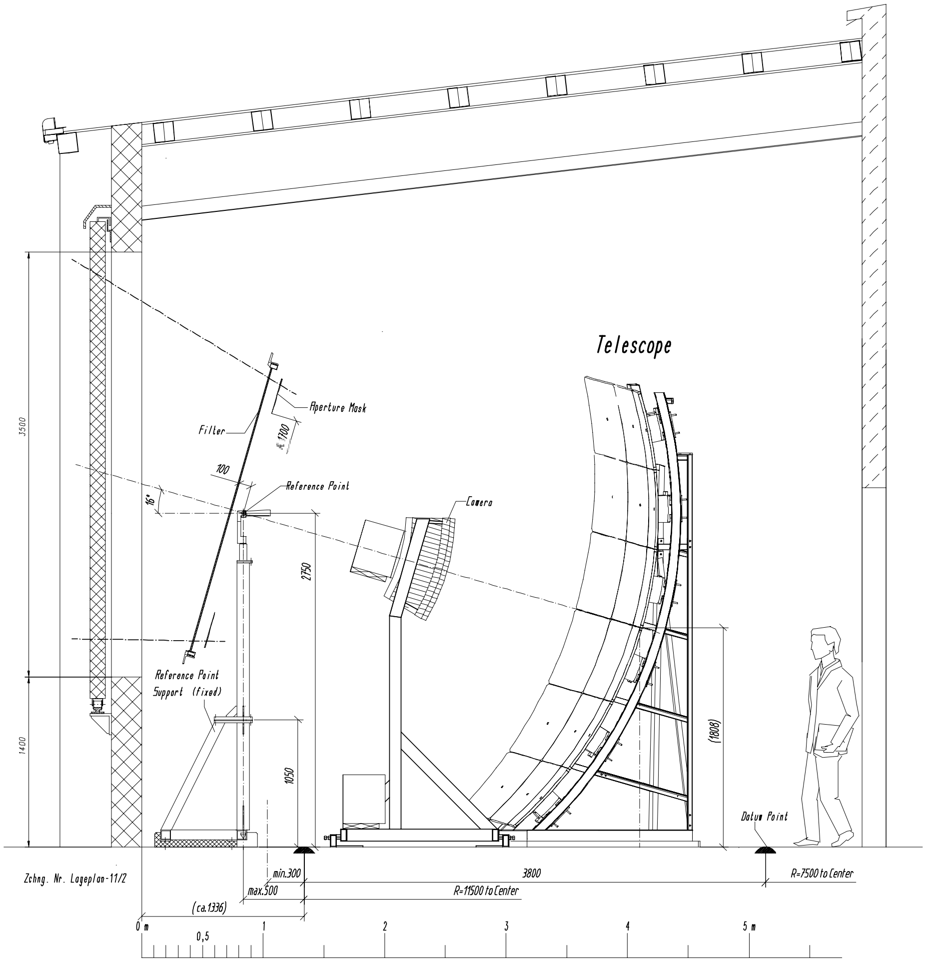

Figure 1.11 The reference point defines the center of the telescope geometry. The orientation of the telescope is defined by datum points on the ground and the 16 degree elevation of the central line of sight.

1.1.4.1.4 Camera System

1.1.4.1.4.1 Camera Body

The main parameters of the camera are fixed by the reference design of the optics which is based on the Schmidt system without corrector plate.

(a) **Geometry:** The pixel surface must lie on the focal surface, i.e. the spherical surface where the circle of least confusion has minimum size. The radius of the focal surface, R_{foc}, is 1.743 m. On this focal surface the spot is rather well defined with a diameter of 15 mm corresponding to an angular size of 0.5^{O}.

The pixels should be hexagonal. Hexagons with side to side distance of 45.6 mm, corresponding to angular size of 1.5^{O} were chosen. Taking 3 pixels with one vertex in common, the angle between the center of the staggered pixel with respect to the line connecting the other two pixels centers is $\Delta\phi = 1.5^{\mathrm{O}}\cos30^{\mathrm{O}} \sim 1.3^{\mathrm{O}}$. The pixel centers are placed on the spherical surface by following the procedure shown in Figure 1.12. We use a *xyz* cartesian reference system. In the *xz* plane, pixel centers are placed at a distance R_{foc} from the origin. The first center is placed at $+\Delta\theta/2$ with respect to the *z* axis. The other pixel centers are obtained with increasing (decreasing) $\Delta\theta$ steps. Twenty pixels correspond to 30^{O} azimuthal aperture. The following row of pixels is obtained with a rotation of $\Delta\phi$ around the *x* axis. To produce the correct staggering, the pixel centers are moved by $\Delta\theta/2$ with respect to their previous position. The other rows are similarly obtained.

Once the pixel centers have been defined, the pixel hexagonal shape is determined by positioning six vertices. The angular positions of the vertices are obtained by moving in steps of $\Delta\theta/2$ and $\Delta\phi/3$ with respect to the pixel center as in Figure 1.12(b). Equal steps in angle produce different linear dimensions depending on the pixel position on the spherical surface. Thus, pixels are not regular hexagons, and their shape and size vary over the focal surface. However, differences of the side length are smaller than 1 mm, and are taken into account in the design of the light collectors.

The camera is then composed of 440 pixels, arranged in a 20x22 matrix (Figure 1.12(c)). The corresponding azimuthal range is 30^{O} with an elevation angle coverage of 28.6^{O}.

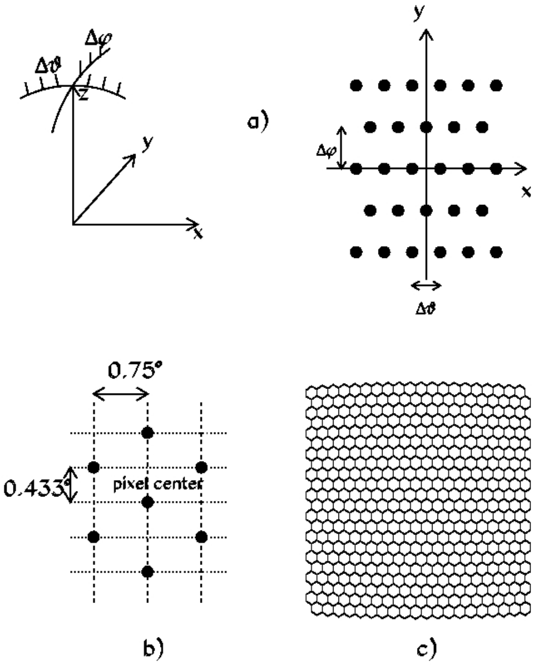

Figure 1.12 Geometrical construction of the FD camera: (a) pixel centers are placed on a spherical surface in steps of Δθ and Δϕ; (b) positioning of the pixel vertices around the pixel center; (c) the camera with 440 pixels arranged in a 20x22 matrix.

(b) **Mechanics:** The camera body was constructed according to the geometry previously described. It was produced by numerically controlled machining of a single aluminium block. It consists of a plate of 60 mm uniform thickness and approximately square shape (930 mm horizontal x 860 mm vertical), with outer and inside surfaces of spherical shape. The outer radius of curvature is 1701 mm, while the inner radius is 1641 mm. Photomultiplier tubes are positioned inside 40 mm diameter holes which are drilled through the plate, corresponding to the pixel centers. Holes (3.2 mm diameter) drilled in the camera body at the pixel vertices, with the angular coordinates shown in Figure 1.12, are used to secure the light collectors in place. A picture of the camera body is shown in Figure 1.13. The camera body has area of about 0.8 m^2 and obscures the geometrical aperture of the diaphragm by 35%.

1.1.4.1.4.2 Camera Support

Mechanical Rigidity and Obscuration: The support of the body of the camera should ensure mechanical stability over long periods of time. Unavoidably it will produce additional obscuration of the mirror's field of view. The support designed for the prototype telescope has a cross-sectional area less than $0.1m^2$ (about one tenth of the camera itself) which we consider acceptable. It consists of a simple and robust two-leg steel support. A drawing of the support structure is shown in Figure 1.14. Note that the power and signal cables run inside the two legs of the support (C-shaped steel beams 5 cm wide) without producing additional obscuration.

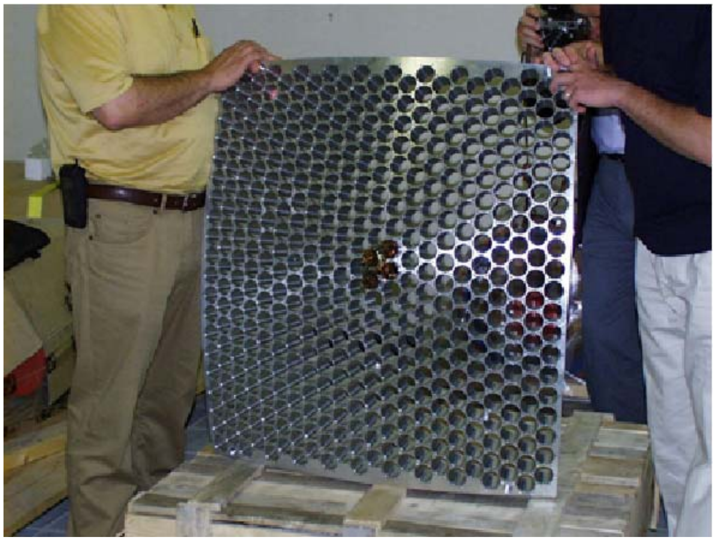

Figure 1.13 Picture of the camera body.

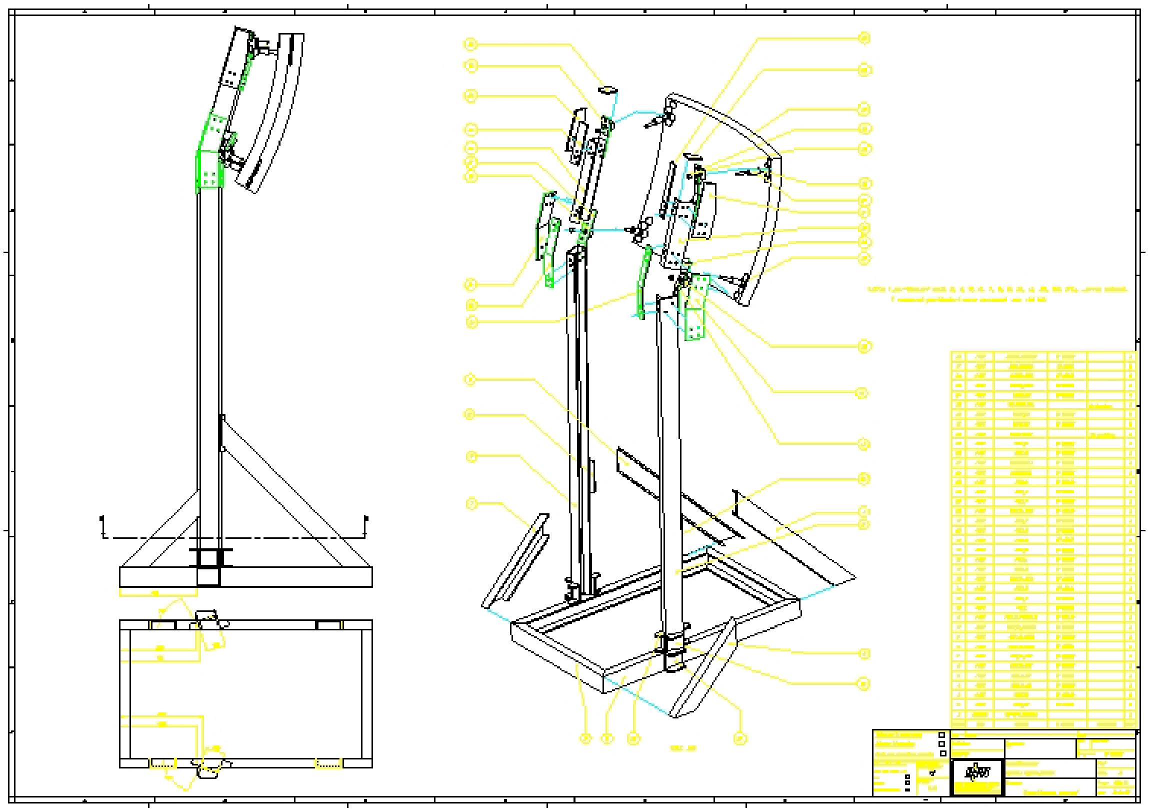

Figure 1.14 A drawing of the camera support.

1.1.4.1.4.3 Mechanical Precision and Alignment

(a) **Precision:** The spot size increases by about 15% when the longitudinal distance from the center of curvature changes by ± 4 mm [1]. A deterioration of the spot at the 10-15% level is acceptable.

The accuracy on the longitudinal position of the pixels on the focal surface should be better than ± 3 mm. The overall uncertainty in the positioning of the pixels has two contributions:

(i) Point-to-point internal accuracy of the pixels on the camera body. The mechanical precision for the prototype camera body is at the level of ± 1 mm both in the longitudinal and transverse directions. This is in fact due to the positioning of the PMTs and of the light concentrators. The intrinsic accuracy of the rigid metal frame of the camera body is ± 0.1 mm.

(ii) Accuracy of alignment of the body of the camera on the focal surface. This requires mechanical adjustments of the camera body to better than ± 2 mm.

(b) **Alignment - Mechanical Adjustment:** The basic requirement for the alignment of the camera is that the pixel surface should be placed at the correct longitudinal distance with respect to the center of curvature of the mirror (the reference point), and that the telescope axis should pass through the camera center.

Several mechanical adjustments were included in the design:

(i) the base of the support is placed in a rigid frame on the floor. Screws are provided on the sides of the frame which allow horizontal displacements of the support on the floor by ±5 cm.

(ii) four screws placed at the base of the support allow vertical displacements of the support with respect to the floor level by ± 5 cm.

(iii) four screws which fix the camera body to the support legs can be used for finer adjustments.

The camera is first aligned in the horizontal plane by using a digital level-inclinometer with a precision better than 0.05^{O}. The inclination with respect to the floor is similarly obtained. The camera center is placed along the telescope axis, defined by a line on the floor from the survey, with a plumb. Then, the nominal distance from the reference point is obtained by a precision rod measuring the distance to the back surface of the camera in several points with a precision of 0.1 mm. A laser distance-meter with a precision of ± 1 mm is also used for the same purpose.

The precision of the alignment of the camera was checked by a theodolite survey. Also, measurements of the mirror spot size on the pixel focal surface were performed, which confirm the specifications.

1.1.4.1.4.4 Light Collectors

The design of the FD camera involves a matrix of hexagonal pixels covering a field of view of approximately 30^{O}x 30^{O}, appropriately arranged over a spherical focal surface. Hexagonal PMTs (Photonis XP3062) were used to instrument the camera. Even if their hexagonal shape represents the best approximation to the pixel geometry, a significant amount of insensitive area is nevertheless present. In fact, some space between the PMTs is needed for safe mechanical packaging on the focal surface. Moreover, the effective cathode area is smaller than the area delimited by the PMT glass envelope. In order to maximize light collection and guarantee a sharp transition between adjacent pixels, the hexagonal PMTs are complemented by light collectors.

The requirements to be fulfilled by such light collectors are:

- good matching of the hexagonal pixel geometry,
- sharp transitions between adjacent pixels,
- almost complete recovery of the light falling on the insensitive regions.

(a) **Geometry:** The basic element for the pixel light collector is a *mercedes star*, with three arms at 120^{O}. We position a *mercedes* on each pixel vertex, so six *mercedes* guarantee the light collection for a given pixel. An illustration of the geometrical structure is given in Figure 1.15. The arm length is approximately half of the pixel side length. The arm section is an equilateral triangle. The base length of 9.2 mm is designed to match the photocathode inefficiency, ~2 mm for each adjacent PMT, plus the maximum space between PMTs glass sides, of the order of 5 mm. The triangle height is 18 mm, and the corresponding angle at the vertex is 14.3^{O}.

We optimized the geometry of the light collectors taking into account the characteristic features of the FD telescope. In fact, the Schmidt optics of the telescope produces a light spot of 15 mm diameter on the focal surface, with light ray angles of incidence in the interval between approximately 10^{O} and 30^{O}. The upper limit is determined by the aperture of the diaphragm, while the lower limit results from the shadow of the camera. We performed a Monte Carlo simulation of the FD telescope optics, where light rays are traced from the diaphragm up to the PMT photocathode, including reflections on the *mercedes*. We chose the geometry of the *mercedes* to maximize the light collection efficiency. The highest light collection efficiency, averaged over the FD focal surface, was found to be 94%, assuming a reflectivity of 85% for the surface of the light collectors (aluminized mylar). We validated the Monte Carlo simulation by performing a dedicated measurement of the camera uniformity (see below).

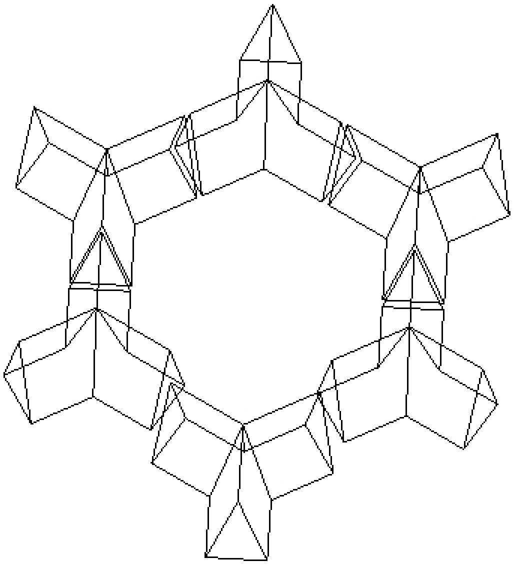

Figure 1.15 Six *mercedes* positioned in order to form a pixel. Each *mercedes star* has three arms at 120^{O}; the arm section is an equilateral triangle of 9.2 mm base length and 18 mm height.

(b) **Mechanics:** The *mercedes* are produced by plastic injection moulding. Each *mercedes* must be precisely positioned on the spherical focal surface. For this purpose, the camera body has 3.2 mm diameter holes corresponding to the positions of the pixel vertices. Each mercedes is held at its center by a bar, approximately 10 cm long. The bar is fixed on one side at the bottom of the mercedes, and on the other side it is threaded. The bar is passed through the hole on the camera body, and a tapped cylinder is screwed on the bar thereby holding the mercedes in position. A picture of a few light collectors and PMTs mounted on the camera body is shown in Figure 1.16. Note that the pixels are defined on the focal surface where the top edges of the *mercedes* divide one pixel from its neighbors. The PMT cathodes are therefore recessed behind the focal surface.

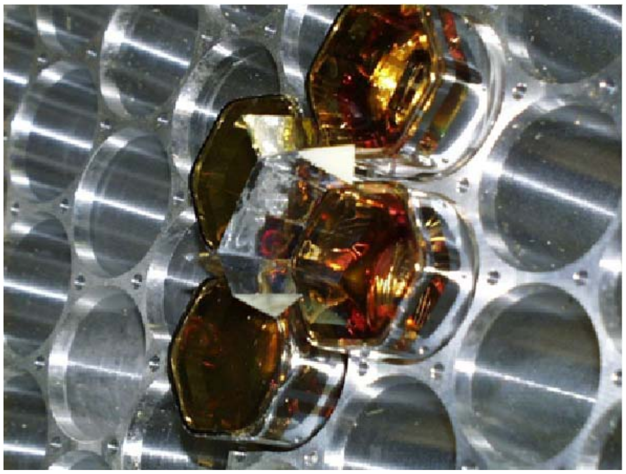

Figure 1.16 The mounting of light collectors.

(c) **Reflectivity:** The mercedes surfaces are covered by a reflective material. Aluminium guarantees the best reflectivity in the range of interest of the nitrogen fluorescence light (300-400 nm). A reflectivity >80% should be adequate for our purpose. Several options have been considered, such as aluminized mylar, adhesive aluminium foils and standard aluminium evaporation. All guarantee good reflectivity.

For the prototype camera, the reflective surface is obtained by gluing aluminized mylar on the *mercedes* surfaces. The mylar foils are slightly longer than the *mercedes* arm, in order to accomodate the pixel side length variation over the focal surface.

(d) **Camera uniformity:** We performed detailed measurements of the response to light of the FD camera with a set up which closely simulated the optics of the FD telescope [5]. A small version of the full size camera body held seven Photonis hexagonal phototubes XP3062, arranged in a *sunflower* configuration. A light diffusing cylinder which simulated the FD optics was moved over the *sunflower* surface in steps of a few millimeters. The light from the exit hole would hit one or more PMTs depending on its position over the surface. For each step, the signal of each photomultiplier was measured, and normalized to the value obtained when the light spot was positioned over the center of the PMT. Then, the sum ε of the normalized signals was calculated. For full light collection efficiency, ε is expected to be close to unity.

We took a first set of measurements without the light collectors, placing the exit hole of the light diffusing cylinder very close to the PMT photocathodes. Afterwards, the *mercedes* were mounted on the small camera body and we repeated the light scans placing the exit hole of the light diffusing cylinder very close to the edges of the light collectors. One example of results from a scan is shown in Figure 1.17.

In the measurements performed without light collectors, we observed significant losses of light at the pixel borders, with up to a 70% loss at a pixel vertex. Also, we measured a non-uniformity over the photocathode surface of at most ±10%. The non-uniformity is particularly evident at the edges of the PMT, and has a similar structure for different PMTs. It is related to the shape of the electric field collecting the photoelectrons and to the position of the first dynode.

On the other hand, the light collectors are efficiently recovering the light loss. The uniformity within a given pixel is also improved, since light rays which were hitting the photocathode borders are now redirected by reflection off the *mercedes* into the central region of the photocathode.

We determined a complete efficiency map of the *sunflower* equipped with light collectors. From these measurements, the light collection efficiency averaged over the FD focal surface was found to be 93%.

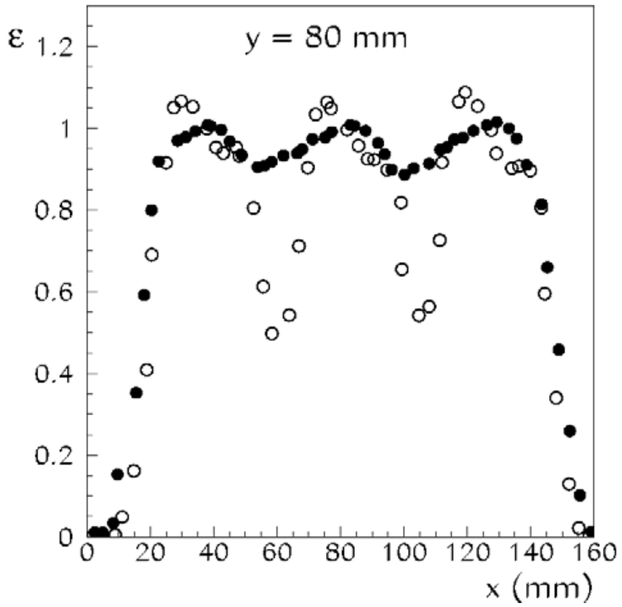

Figure 1.17 Measurement of the light collection efficiency, with a light spot moved along a line passing over three pixels. The full dots represent the measurements performed with the *mercedes*, while the open dots represent the measurements without the *mercedes*. In limited regions of the photocathode the light collection efficiency can be greater than one, since ε is normalized to the average light collection efficiency integrated over the photocathode surface.

1.1.4.1.4.5 Photomultiplier

(a) **Shape and size:** The pixels of the camera lie on the spherical focal surface. They are hexagonal in shape. Therefore hexagonal PMTs are to be preferred because the system of Winston cones for optical coupling between pixel and photocathode becomes much simpler. The specifications of the overall optical system require pixels of 1.5^{O}. This corresponds to hexagonal pixels with side-to-side distance of 45.6 mm. The maximum external size of the PMTs must be somewhat smaller to allow the required configuration of the camera on the focal surface, the axis of each PMT being aligned with the center of curvature of the mirror.

(b) **Uniformity of response over the photocathode:** All commercial PMTs have some non-uniformity of response over the cathode. It is generally a slowly varying function of the distance from the center of the cathode. We require that the non-uniformity should be in the range of good commercial tubes, within ±15%. We must keep in mind that the size of the light spot for a point source at infinity is about one-third of the size of the pixel and therefore the uniformity of response is not a critical parameter.

(c) **Spectral response:** The reference design value considers a quantum efficiency that averages 0.25 in the range 330-400 nm. This corresponds to standard bialkali photocathodes. We allow a reduction of not more than 10% below this value.

(d) **Gain:** The nominal gain for standard operation will be around $5x10^4$-10^5. Therefore an 8 stage PMT should be adequate.

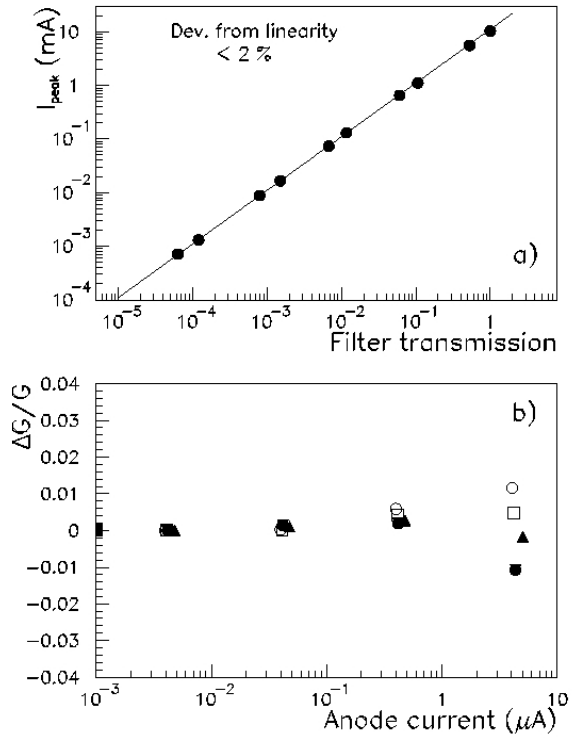

Figure 1.18 Measurement of (a) PMT linearity and (b) gain variation vs average anode current for four PMTs.

(e) **Linear dynamic range:** This property is actually more related to the divider chain than to the PMT itself. In any case we require that the tube, operated at nominal gain (see directly above), should have linear response within better than 3% over a dynamic range of at least 10^4 for signals of 1μs. The upper limit of the signal can be fixed at an anode current of 1 mA (10 mA) for signals of 1 (0.1) μs width, which corresponds to $6x10^4$ photoelectrons for a gain of 10^5.

(f) **Moonlight tolerance and longevity:** The gain of a tube deteriorates during operation as the integrated charge increases with time. Apparently the half-life of a tube (the time for reduction of the gain to one half) is correlated with the integrated charge collected at the anode. We require that the integrated anode charge corresponding to the half life of the tube not be less than 350 C.

(g) **Single photoelectron:** Even though the standard operation of the PMT will not require the measurement of single photoelectrons, the PMT should have some single photoelectron capability, which guarantees a good resolution for the tube. No specific peak to valley requirement is needed, the evidence for a peak being sufficient.

The hexagonal photomultiplier XP3062 from Photonis was chosen as the detector PMT. A detailed study of its characteristics is available in [6]. Figure 1.18 shows an example of a measurement of the PMT linearity, and of the gain variation as a function of light intensity.

1.1.4.1.4.6 Photomultiplier Unit

The PMT, the base and the preamplifier will be a physically single unit. We have adopted a solution with flying leads on the PMTs.

In the prototype design, the leads are soldered to a small circular printed circuit card that contains the HV divider chain. A second card mounted axially, close to the divider chain card, contains the preamplifier circuit and some additional circuitry. A third card is needed to house the connector for HV, LV and signal distribution. The present design, involving three printed circuit cards, is imposed by the space needed for the additional circuitry of the anode current measurement and the electronics test pulse. The card diameter is 32 mm, which allows the mechanical mounting of the PMT units on the spherical camera body.

For mass production we recommend the design where a circular card containing the HV divider chain is soldered to the flying leads of the PMT at the factory. The preamplifier card could be mounted either axially or orthogonally and integrated at the factory according to our design and prescriptions. A test of the unit (PMT+base+preamplifier) should be made at the factory with our supervision, using the PMT unit test system developed by us. Control tests on samples of the production will be performed in the collaborating institutions.

1.1.4.1.4.7 Backplanes, Cables and Connectors

High voltage for the PMT base and low voltage for the preamplifier/driver are needed for each tube. Also, differential signals from the PMT preamplifier are driven in twisted pair cables up to the front-end boards.

In the solution adopted for the FD prototype, cables are distributed through backplanes positioned in the camera shadow. Each backplane supplies HV and LV to 44 PMTs. The differential signals are grouped into multi-pin connectors. Also, the facility for a test pulse signal to the preamplifier/driver is provided.

(a) **Cables and Connectors (PMT to backplane):** A single cable brings HV and LV to the PMT from the backplane, and drives the differential signals out of the preamplifier. Eight wires are used in the current configuration: two for the differential signal (twisted), two for positive and negative LV (twisted), two for HV and ground (twisted), and two for the test pulse signal and additional ground. A compact (1.3 x 0.5cm) 10-contact connector is used at both ends of the cable. Two contacts near the HV are left free for further insulation. The cable length is 35 cm. The assembly has been produced by 3M. HV insulation was tested up to 2 kV.

(b) **Backplane:** The camera backplane is a printed circuit card of rectangular shape (22 cm x 32 cm). The card is composed of six layers: one HV and one LV distribution layer, one signal layer sandwiched between two ground layers, and a test pulse layer. HV from one input connector is distributed to 44 PMTs. The low voltage distribution is analogous. A fuse for overcurrent protection is included in each distribution line. Differential signals from 11 PMT units, corresponding to half of a pixel column, are grouped into a low profile 26-pin connector. Each card has four of these connectors. The grouping was chosen in order to avoid crossing of signal lines and HV/LV lines, therefore minimizing crosstalk. The 440 PMTs of a FD camera are served by ten backplanes. The space between backplanes (~ 15 cm) allows access to photomultipliers and light collectors.

(c) **Cables and Connectors (backplane to Analog Board):** A round shielded cable with 11 twisted pair signal wires, ground and test pulse wires is plugged into each of the four connectors on the backplane. Two of these cables, from two corresponding upper and lower backplane cards, are joined into one single connector at the Analog Board (AB). Thus, the 22 pixels of each pixel column are mapped into one AB as specified by the FDE group.

A special support, which closely follows the spherical shape of the camera body, holds the boards and cables in the shadow of the camera, *i.e.* inside the pyramid with a vertex on the common center of curvature of the mirror and camera and sides at 15^{O}. A picture of the back of the camera with boards and cables in place is shown in Figure 1.19.

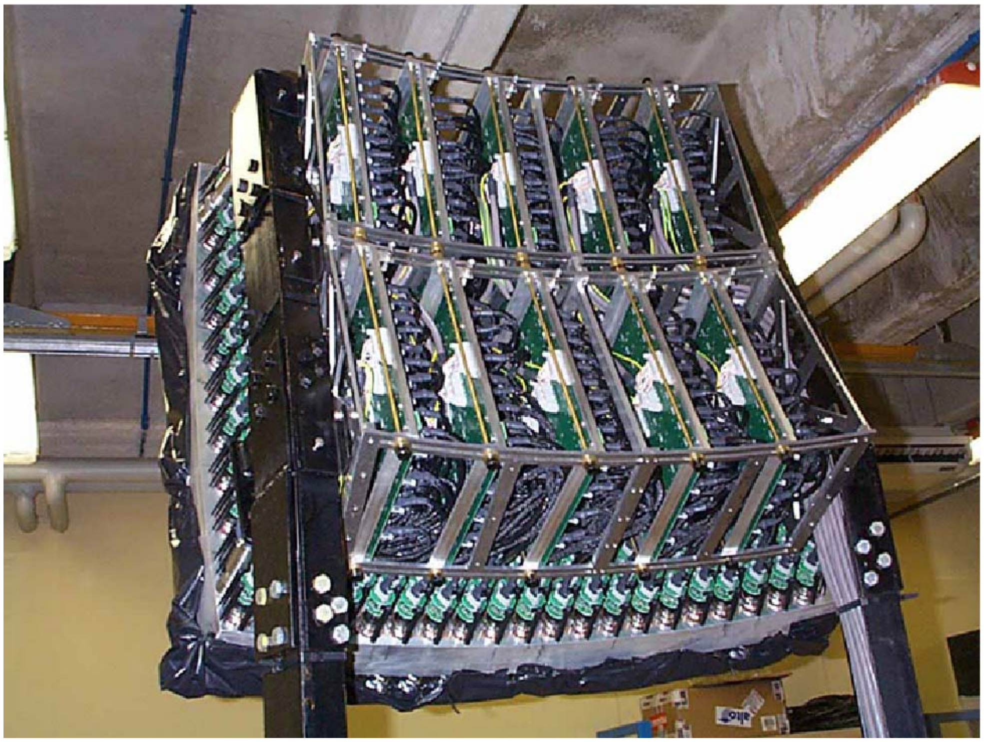

Figure 1.19 Picture of the back of the camera, showing the distribution boards and cables.

1.1.4.2 **Buildings**

Each eye will be housed in a single building. The central eye will consist of 12 telescopes. The perimeter eyes will have only 6 telescopes. The Los Leones perimeter eye was the first to be constructed. The ground plan of the 7m high single story building is shown in Figure 1.20. The radius of the building is 14m. The 6 telescopes point radially outward through 6 windows of 3m (w) x 3.5m (h) each at the perimeter of the building. Attached to each window is the aperture system on the inside and two sliding doors on the outside. The rear part of the central area contains the data acquisition room, a small laboratory room and a room for calibration equipment. Above these rooms is a gallery providing space for equipment needed for calibration and atmospheric monitoring. All rooms, the telescope bays and the gallery are connected to the data acquisition room through a Local area Network (LAN), the data acquisition room has an optical fibre ETHERNET link to the communication tower located at the south perimeter of the eye area. The light sources in the calibration room deliver light to the telescopes by optical fibre. Many details had to be considered about how the telescope bays are partitioned from each other, how the lighting should be arranged, cable tray locations, etc. The layout of the building at Los Leones turned out to be a satisfactory solution. Based on the experience gathered during the installation and operation of two prototype telescopes in the Los Leones building, only minor modifications are required for the design of future buildings.

1.1.4.3 Heating, cooling, and humidity control

The building temperature should be maintained at 21±3 degrees Centigrade. This is partly because the PMT gain varies by approximately 0.5% per degree. If we maintain a temperature of 21^o, the PMT gain will not change due to temperature, and a 3^o deviation causes only a 1.5% gain variation. This will not be a significant contribution to our calibration uncertainty. Other electronic components may change characteristics under large temperature changes. The specified range will prevent that. Perhaps the strongest constraint on temperature variation is mandated by the optics. The mirror shape will change a small amount with temperature. To keep the spot size small, we need to keep the temperature constant to within $\pm 3^o$ C.

For the sake of the electronics, the relative humidity should not exceed 70%. Experience with the prototype detector will tell us whether or not we need to incorporate humidity control in the eye buildings. Probably the building interior will rarely have such high humidity at night in the desert when the weather is suitable for observations.

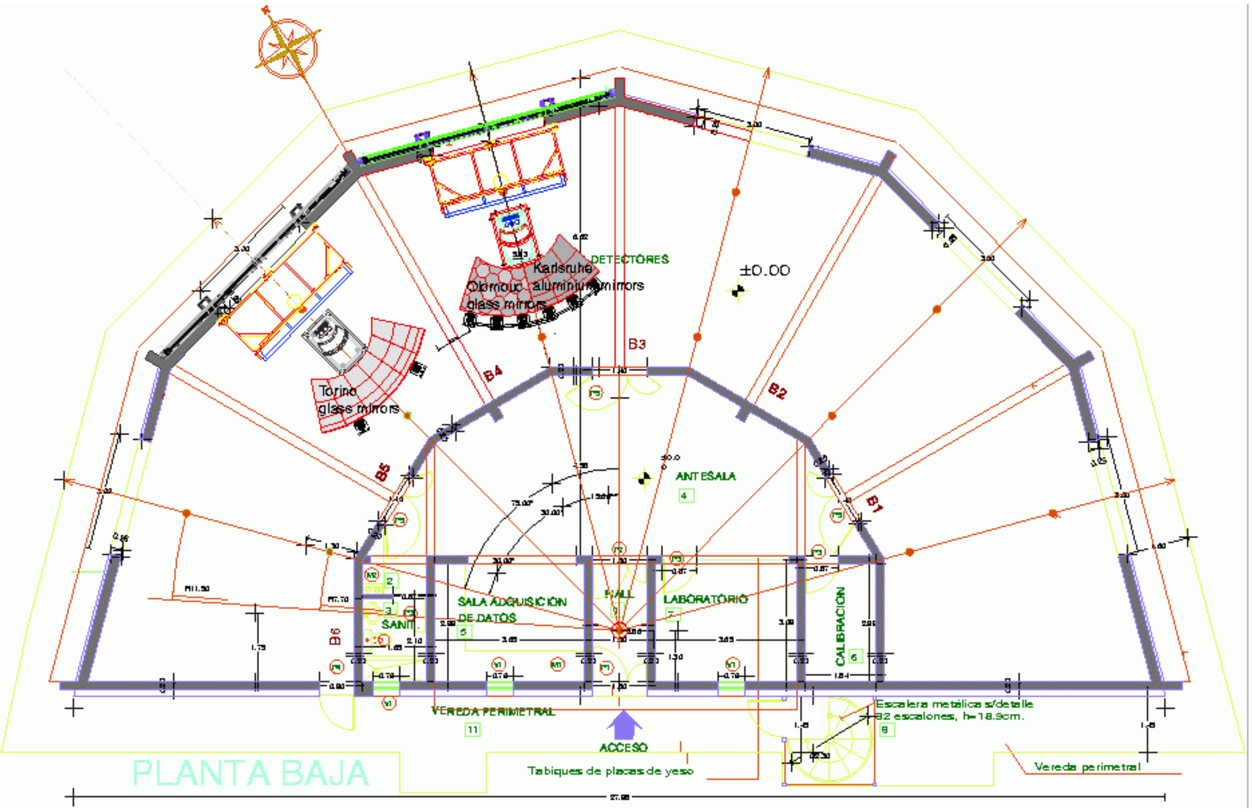

Figure 1.20 Layout of the FD building at Los Leones with prototype telescopes in bay 4 and 5.

1.1.5 Options and Development Work

1.1.5.1 Corrector Plate

From TDR Version August 2000: This design option exploits the possibility of reducing the spherical aberration, which is not eliminated by the diaphragm, by putting a corrector plate at the center of curvature of the mirror, turning the FD into a true Schmidt camera. This approach can be reversed and the use of a corrector plate is then seen as a way of increasing the diaphragm aperture while keeping the spot size under control, thereby increasing the effective light collection area of the detector, which increases the S/N ratio.

The first option is a corrector plate of Type II [7] having:

(a) radius: 1.13m (compared with a baseline design diaphragm radius of 0.85m)

(b) thickness of the center of the plate, $T(0)$=10 mm

(c) tolerance: +/-1 mrad on the normal to the surface of both mirror and corrector plate.

The material would be UV-transmitting acrylic (refractive index 1.49). Such a corrector plate would increase the effective light collection area by 90% while keeping the spot diameter under 0.6^{o} [1,2,8]. The cost would be under US$500 per corrector plate. The fabrication technique is under study. (**September 2001:** This option has been abandoned).

Alternatively, there is an option of using a corrector ring or annulus. The possibility of correcting for spherical aberrations and/or increasing the diaphragm radius while keeping the spot size controlled, also reducing fabrication difficulties and costs, prompts the study of this alternative design with the Schmidt correcting device having the shape of a ring covering the outer region of the diaphragm.

For this option,

(a) inside diameter: 1.7m

(b) outside diameter: 2.2m

(c) shape: Type II (see above)

Here the spot diameter is kept under 0.6^{o} while increasing the light collection area by almost 40% [9]. (**September 2001:** Progress on this option is described in section 1.1.4.1.2.2)

An alternative corrector plate method is the Maksutov-Bouwers design in which the corrector plate is a thick miniscus lens. The Puebla group have studied 4 different variations [10]. In these designs, the corrector plate does not disrupt the spherical symmetry and there is no chromatic aberration introduced. Like the other Schmidt corrector plates, it remains to be demonstrated that it is practical to incorporate such a lens in a camera of this large size that must operate for many years. (**September 2001:** this alternative has been abandoned).

1.1.5.2 Interference filters

From TDR Version July 2000: Wide band interference filters are an interesting alternative to absorption type filters used by the Fly's Eye and HiRes [11]. Such interference filters can be designed to have a nearly flat transmittance of 85% from 320-410 nm. We have done angular dependence tests on some interference filters not designed specifically for Auger. For a shift of 25 degrees in incidence angle, we have observed a 12 nm shift of the transmittance curve in the case of ZrO_2 SiO_2 16-layer structure with transmittance around 85% in the UV region and up to 600nm, while the transmittance drops above this wavelength.

In the case of a 16 layer structure of a WO_3MgF_2 filter, we have achieved an average transmittance of 74% in the range 350-400nm. The transmittance curve shift for a 15^o angle is less than 6 nm and the peak transmittance value is roughly invariant. By redesigning the layer thicknesses, we hope to achieve a steeper drop of transmittance above 415 nm. This can be done by adding about 4 layers of film on the other side of the substrate. At any rate, the average transmittance in the range 415 to 600 nm is about 9.5%. One has to take this average value of transmittance in the visible range to consider the effect on the S/N ratio. In the range above 600 nm, where the transmittance is rising again, there seems to be no concern since the PMT quantum efficiency (Philips XP3062) is greatly reduced. At any rate, by adding 4 layers of coating, the transmittance in this red range can be reduced to a certain extent if it is considered necessary after detailed Monte Carlo study.

The mechanical stability of the wideband filters depends on the construction method. Of the two most widely used methods, electron-beam deposition and reactive DC sputtering, the former produces more porous thin film multilayers. This may be prone to humidity attack if a special protection procedure is not followed. The effects of humidity could be significant if the filter has significant porosity due to the construction method and in the absence of protective coating. The second method gives better quality filters (less porous). However, it is normally a slower method and most probably more expensive and needs stricter control of the oxygen flow in the process chamber.

We hope to study both methods, and in particular we would like to have more filter samples produced by sputtering to assess the merits of this method.

For the sake of mechanical stability of the filters, we suggest that they are produced, if we use the e-beam deposition method, by substrate heating. In this case, a specific crystal phase dominates which leads to more favorable mechanical compatibility of the heterostructure to be chosen (most probably ZrO_2SiO_2). These thoughts are supported by work of Dobrowofsky et al. [12].

Strains can produce long-term aging in the filters and thus they should be well understood. A method for measuring the strains and stresses must be selected ensuring it is accurate, easily available, inexpensive and fast. One may examine the possibility offered by Raman scattering techniques [13].

Cost considerations are quite intricate. If some institutions participating in Auger have the infrastructure (coating plants) to produce wide-band interference filters, then the filter may cost less per given area than if the coating equipment needs to be purchased. The same is true for other types of filters such as absorption filters. If they can be produced by private companies or by research institutes in a way that meets the technical specifications, then this is better than if only one or two companies exist which give poor satisfaction to the specifications for the fluorescence detector. From the existing data on the absorption filter of HiRes, it seems that the filter approaches Elbert's maximum "improvement factor", but this maximum performance factor evaluated for an "ideal wide band interference" filter is perhaps somewhat underestimated. This is the opinion of E. Fokitas, since it may be possible to produce interference filters with UV transmittance better than the 80% assumed by Elbert. It cannot be excluded that interference filters of around 85% transmittance between 320-420nm are possible.

September 2001: The development of a suitable interference filter is too far behind schedule to be a realistic alternative to commercially available absorption filters which have already been tested successfully in the prototype systems. Further development of this filter option has therefore been abandoned.

1.1.5.3 Filter at the camera

Positioning the optical filter in the diaphragm (ie the reference design) has some clear advantages:

(a) We need a window there and we don't want additional light losses (at least 10% for any window without anti-reflective coating).

(b) The range of incidence angles extends only to 21^o at the corners of our field of view (versus a cone of 27^o half-angle for a pixel's view of the illuminated mirror portion).

The alternative of putting the filter directly in front of the camera also has some important advantages:

(a) Less filter area is required (less than $1m^2$ versus $2.3m^2$, or $3.8m^2$ with corrector annulus).

(b) Every pixel has the same distribution of incidence angles. (This is strictly true only if the filter follows the camera curvature. The cone is not centered on normal incidence if the filter is a plane in front of the camera.)

(c) The filter is not subjected to outdoor temperatures and abrasives.

(d) The filter is decoupled from the corrector plate option.

However, the filter in front of the camera should be made of only one piece of approximately 90cm x 90cm, which is not a standard commercial size. In fact, several pieces of glass would introduce at their borders inefficiencies on the camera.

The requirement of a spherical shape for a single glass piece implies additional cost for the production, and care for the glass thickness.

Instead of a plane sheet of filter in front of the camera, a filter could be cut for each PMT and bonded to the PMT face, thereby eliminating additional surface losses in the filter. It should be noted that, in this case, there are some large incidence angles due to photons that have reflected off the mercedes walls. It should be verified that the filter is effective also at large incidence angles.

If the filter is not placed at the diaphragm, a window of UV transparent glass must be introduced. The cost of the glass and the mechanical structure to hold it in place should be taken into account.

The option of taking the filter out of the diaphragm does not show a clear cost or physics advantage. It should be considered only if a deterioration of its performance due to environmental damage is observed during the engineering phase.

1.1.6 Prototype Plans and hybrid engineering

1.1.6.1 Objectives

The engineering phase is intended to be a learning experience in which we discover flaws in the design, find the best design, develop optimal fabrication methods, refine the analysis procedures, and demonstrate that the hybrid shower detection capability meets the project's requirements. Our goal is to construct a world class fluorescence detector that measures air shower longitudinal profiles with high sensitivity. It may be useful to state some specific aspects of this goal:

(a) **Optics demonstration.** Independent of event triggering and longitudinal profile measurements, we wish to prove that the telescope achieves the expected quality of optical performance. One way to do this is to cover the camera with a stretchable white material, then fly a bright light around in the field of view with an airplane. The spot should be clearly visible on the white focal surface (if the optical filter is not present), and a normal video camera can document the optical performance. Captured still frames can be used to measure the effective spot size at different parts of the field of view. This should verify that the spot is circular and independent of position in the field of view, and not larger in diameter than 1/3 of the pixel diameter. (This general procedure was used successfully to test a Schmidt diaphragm at the dual mirror test stand in Millard County.) An alternative to the airplane and bright light is to make multiple CCD camera time exposures during the transit of a bright star or planet across the telescope's field of view. The star or planet moves less than 0.1^{o} during a 20-second CCD integration, and that may provide ample signal-to-background for determining the image of the point source.

(b) **Laser profiles.** A pulsed laser beam mimics an upward-going shower in the sense that light is emitted (scattered in this case) from a narrow segment that moves along the axis at the speed of light. The longitudinal profile seen by the telescope generally decreases with altitude because the beam attenuates and the density of scatterers decreases with altitude. Wispy clouds or smoke plumes show up as bumps on the longitudinal profile. If the laser pulse is produced by a lidar system, the amount of scattering is recorded by the lidar as a function of altitude. The longitudinal development measured by the telescope should agree with what the lidar records. (Some difference might be expected if the total phase function changes with altitude, and that can occur as Rayleigh scattering becomes dominant over aerosol scattering.) The first objective is to see a continuous longitudinal profile that tells us that the pixel-to-pixel calibration is sensible and that we are recording sensible signals.

(c) **Event trigger tests.** Laser pulses can also be used to test the trigger sensitivity of the telescope. On a very clear night, the amount of light scattered from a pulse can be reliably calculated as simple Rayleigh scattering. By measuring the pulse energy, the light flux at the detector can be well estimated. In this way, one can approximately simulate a shower of a given energy at any distance. This allows a quite rigorous demonstration of trigger sensitivity. Assuming a 15-km attenuation length, a laser beam pulse at 350nm requires 21 μJ/EeV to simulate the light production by an air shower at its maximum size.)

(d) **Shower-detector plane reconstruction.** By varying the position and pointing direction of such a pulsed laser beam, we can evaluate the accuracy of the telescope in determining the geometry of the shower-detector plane. A roving laser scope will be used for this. A lens in front of the laser can be used to make the beam diverge as a crude simulation of a shower's lateral distribution.

(e) **Timing tests.** For a known laser geometry (produced with the laser scope as above), one can calculate exactly the time when the center of the spot passes each pixel center. his should be compared with the pulse-center time determined from each pixel's FADC trace. Alternatively, one can calculate from the pixel trigger times at what instant the laser must have fired at its known location. A GPS and flash detection system at the laser site could be used to test those predictions. Note that this is a good test for hybrid reconstruction accuracy. Picking out the correct axis within the shower-detector plane relies on getting a prediction from the FD pixel times for the shower front arrival at any ground position. We can demonstrate our ability to do this accurately using pulsed lasers in this way.

(f) **Monocular shower detections.** The telescope will observe a large number of air showers, mostly lower energy showers landing near the detector. The reconstruction of those showers will be handicapped without surface array information. But the shower-detector plane distribution and the light intensity distribution are calculable from the known isotropic cosmic ray intensity.

(g) **Hybrid showers.** Most important is to demonstrate that we do indeed measure the expected number of showers in coincidence with the engineering surface array. For the one prototype telescope operating with a 10% duty cycle with the 40-tank engineering array, Fick's simulations give the following expectations for the event rate per year above a given energy:

Energy (EeV)	0.5	1	3	5	10	30
Events/year	683	386	78	31	9	1

(h) **Options testing.** It should be emphasized again that the purpose of the prototype is to optimize all aspects of the FD detector. We will compare different types of mirror segments. We will test a Schmidt corrector plate to find out if it can increase our light-collecting power without degrading our spot size. We will compare different atmospheric monitoring techniques and different detector calibration procedures, so we can focus our resources on the most worthy. We will test and refine all aspects of the detector electronics. We will enhance the data acquisition system and improve the detector simulation and analysis procedures. We will work out any bugs in the communications system and hybrid triggering and data merging. We will find out what features are needed in the eye buildings that have not been anticipated.

1.1.6.2 Prototype building

The prototype telescope will be housed in the building being constructed for the first fluorescence station at Los Leones.

1.1.6.3 Organization, subtask responsibilities, and work breakdown

The FD prototype telescope has been a European initiative since its inception. A collaboration of Italian institutions and the Karlsruhe groups are supplying strong support for the rapid development of the telescope itself. The entire FD engineering phase of the project is still a broad international effort, however. The division of tasks and leadership responsibilities can be expected to change over the years of the detector construction. Levels of support in different countries have not yet been determined. From experience with the prototype detector we will learn the most efficient ways to take advantage of our international collaboration.

Paul Sommers (Utah) was the task leader for the fluorescence detector during the design, prototype development and installation phase assisted by Jonny Kleinfeller (Karlsruhe) as coordinator of the FD and FDE tasks to complete the prototype telescopes. Hartmut Gemmeke (Karlsruhe) was one of the co-leaders for fluorescence detector electronics until recently.

From April 2001, the task leaders for the fluorescence detector are Jonny Kleinfeller (Karlsruhe) and Paolo Privitera (Roma). Matthias Kleifges (Karlsruhe) and Daniel Camin (Milano) are the present co-leaders for the fluorescence detector electronics tasks. Principal subtask leaders are Hans Klages (Karlsruhe) and Rosanna Cester (Torino) for the mirror system and optics overall, Giorgio Matthiae (Roma) and Paolo Privitera (Roma) for the camera system, and Roger Clay (Adelaide) and John Matthews (University of New Mexico) for calibration and atmospheric monitoring. Carlos Escobar (Campinas) is in charge of developing the aperture system and all its optical components, except for the optical filter which is the responsibility of Rosanna Cester (Torino). Norberto Fazzini is in charge of the telescope buildings. Additional subtasks may be warranted to deal with buildings and infrastructure, diaphragm optics, simulations and analysis, operations and safety, etc.

Responsibility for delivering the various components for the engineering phase are summarized below:

(a) Shutter - Krakow

(b) Diaphragm - Campinas, Karlsruhe, Krakow

(c) Corrector annulus - Campinas, Czech Republic, Karlsruhe, Puebla

(d) Optical filter - Torino

(e) Reference point and mechanical alignment tools - Karlsruhe

(f) Mirror support - Karlsruhe, Torino

(g) Mirror mounts - Karlsruhe, Torino

(h) Mirror segments - Czech Republic, Karlsruhe, Torino

(i) Optical alignment and quality control - Czech Republic, Karlsruhe, Torino, Puebla

(j) Camera system - Catania, Roma

(k) Building - Argentina

(l) Furniture and installation equipment - Karlsruhe

(m) Slow control - Karlsruhe

(n) Calibration - Catania, Colorado, Louisiana State, New Mexico, Utah

(o) Atmospheric monitoring - Adelaide, CBPF, Chicago, Ljubljana, Michigan Tech., New Mexico, Torino, Utah

(p) Detector simulations and data analysis - Adelaide, Campinas, CBPF, Czech Republic, Karlsruhe, Roma, Torino, Utah

(q) Electronics - see FDE section of TDR (section 1.2)

Institutional responsibilities for the various components may also be subject to change based on our experience during the engineering phase of the project. The present agreements for production are:

(a) Diaphragm (with shutter and corrector ring) - Campinas

(b) Optical filter - Torino

(c) Reference point and mechanical alignment tools - Karlsruhe

(d) Mirror support - Karlsruhe, Krakow, Puebla

(e) Mirror mounts - Czech Republic, Karlsruhe, Krakow, Puebla

(f) Mirror segments - Czech Republic, Karlsruhe

(g) Optical alignment and quality control - Czech Republic, Karlsruhe

(h) Camera system - Catania, Roma

(i) Building - Argentina, Karlsruhe

(j) Slow control - Karlsruhe

(k) Calibration - Athens, Catania, Colorado, Louisiana State, New Mexico, Utah

(l) Atmospheric monitoring - Adelaide, Athens, CBPF, Chicago, New Mexico, Ljubljana, Torino, Utah

(m) Detector simulations and data analysis - Adelaide, Campinas, CBPF, Karlsruhe, Krakow, Roma, Torini, Utah, and the whole collaboration.

(n) Electronics - see FDE section of TDR (section 1.2)

1.1.7 Four sites at Pampa Amarilla

1.1.7.1 Layout

The reference design layout is shown in Figure 1.21. The surface detector area is approximately 3000 km^2 with fluorescence detectors on the perimeter on hills called Leones, Morados and Coihueco. A fourth eye is near the center. That eye will view a full 360^{O} of azimuth, while the three perimeter eyes will view 180^{O} of azimuth towards the array.

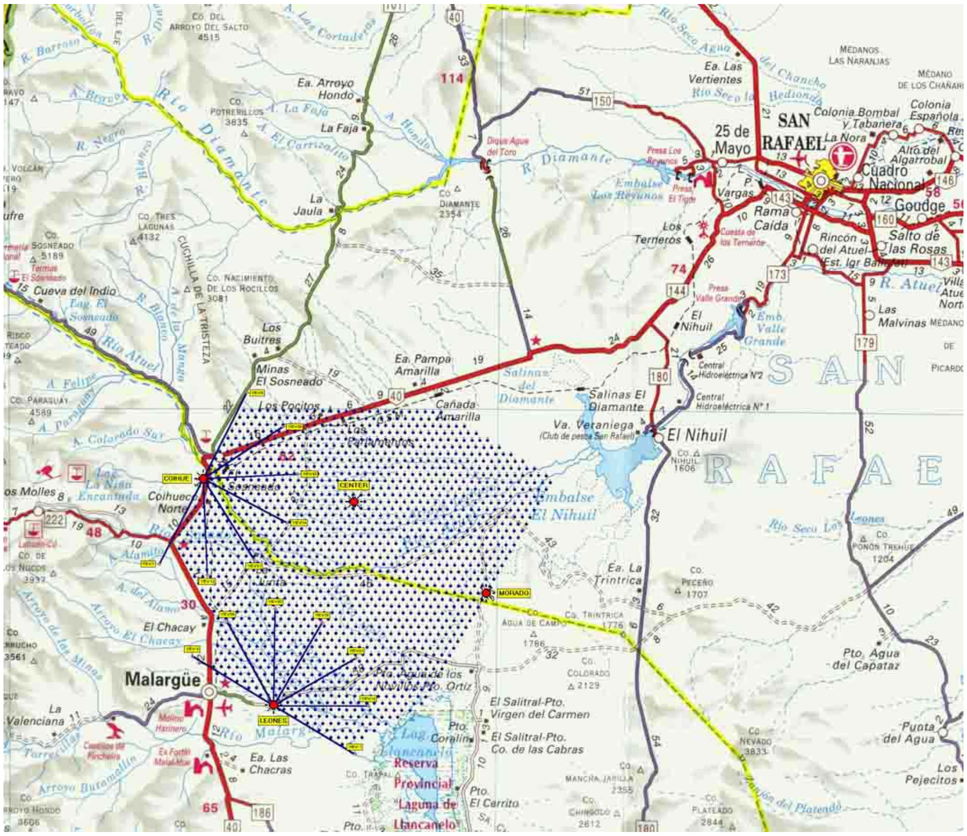

Figure 1.21 The planned arrangement of the 4 fluorescence detectors at the southern site. Three perimeter sites are situated at Los Leones, Coihueco and Los Morados. Each of these sites view 180^{O} of azimuth. The central site views a full 360^{O} of azimuth. The array shown covers an area of approximately 3000 square kilometres - the spacing of the surface detectors is 1.5 km.

1.1.7.2 Schedule

Construction of the full observatory should commence immediately after the 2-year engineering phase, which began with the ground-breaking on March 17, 1999. Construction of the first eye would then begin in the spring of 2001, and the southern hemisphere observatory should be completed in 3 years (spring of 2004).

1.1.8 Quality assurance, hazard mitigation, and safety

1.1.8.1 Optical testing

Verifying the optical quality of the Auger telescopes is an important task. Calibration work may emphasize an end-to-end calibration which folds together all the optical and electronic components. We need to know precisely the quality of the optical components separately also. Procedures are needed for measuring the optical filter's transmittance as a function of incidence angle and wavelength. How much variation is there over its area? Procedures are needed for measuring the optical quality of each mirror segment. The Puebla group demonstrated a new Ronchi tester at the Morelia meeting. We also need to quantify the alignment accuracy of the mirror segments. It would be good to have a system that allows alignment (and measurement) with the camera in place, rather than relying on light returning to the optical center of curvature. The mercedes reflector efficiencies can be measured in a laboratory. We plan to use star transits or other techniques to monitor their efficiency *in situ*.

1.1.8.2 PMT testing and database recording

The typical PMT characteristics are known from the specifications provided by the manufacturer and by our laboratory tests. The manufacturer shall provide for each tube the following information: photocathode sensitivity at the wavelength of 337 nm, photocathode sensitivity with a Corning blue filter, high voltage needed for a gain of 10^5, and anode dark current at a gain of 10^5. In addition, we have defined a test procedure that is applied to each PMT when it is delivered by the manufacturer. The test is performed on the PMT unit, *i.e.* the PMT with the voltage divider and preamplifier cards soldered onto the flying leads, with an automatic PMT test system [14]. In particular, we check the linearity of the PMT unit and the photocathode uniformity. We measure the gain vs. high voltage, which is needed for a proper grouping of the PMTs with similar gain. The relative PMT gain and the relative photocathode sensitivity at different wavelengths are also measured. We plan to perform these tests at the factory before shipping the PMT units to the Observatory. A fraction of the PMT units will be tested in the collaborating institutions.

The information for each individual PMT unit is collected into a database. The database will also track the PMT characteristics after installation, including calibration measurements performed *in situ*.

1.1.8.3 Failsafe mechanisms

The PMT photosensors have a lifetime measured by the anode charge collection. It is essential that they not be exposed to strong light when the high voltage is on. Under normal operating conditions, the diaphragm will be open only during the dark of night. The shutters will not be opened before the end of twilight after sunset and will close again before the start of twilight in the morning. The shutters will be electrically-powered mechanical devices, however. They may fail because of electrical failure or mechanical jamming. A sensor (perhaps embedded between mirror segments) should automatically switch off high voltage if a significant amount of light persists for an appreciable length of time.

Even without high voltage, the camera can be damaged by high light levels. If direct sunlight is focused on the camera, it could burn up despite the optical filter in the diaphragm.

Another battery-operated sensor should be mounted outside the building. It should detect the shutter position as well as light level. If it is light outside and the shutter is not closed, then it should cause the release of a curtain that falls behind the diaphragm to prevent the outside light from reaching the mirror.

1.1.8.4 Safety equipment and operation procedures

The fluorescence detectors will conform to the Project's safety standards for buildings, electrical equipment, fire prevention, etc. Special attention is needed for the eyes because they are expected to be run remotely with a lot of high voltage and electronic equipment concentrated within a single building. We require strict adherence to safety standards for wiring, conduits, circuit breakers, etc. Smoke detectors should be installed with the capability of shutting off all non-essential power and broadcasting alarms.

The detector operating instructions will emphasize safety issues so as to minimize the possibility of accidents. Personnel should work in teams of 2 or more persons at remote sites.

The use of high-power UV lasers constitute a severe danger of eye damage both for Auger personnel and unwitting bystanders. In particular, safeguards are essential to avoid any possibility of blinding an aircraft pilot in the area. The use of beam divergers might solve the problem. If not, a simple radar system may be warranted to identify any aircraft in the danger volume.

A simpler method has been suggested. The idea is to mount a photosensor with about 10^o field of view on the laser. Whenever the sensor detects a light flash (possible airplane strobe), it disables the laser for one minute. A laser pulse would then only be possible if the solid angle around it has been clear of airplanes for at least one minute. High-power UV lasers should be mounted in such a way that their beams can never hit the eye of bystanders at ground level.

1.1.9 Calibration System

1.1.9.1 Reference Design Specifications

1.1.9.1.1 End-to-end calibration

The reconstruction of air shower longitudinal profiles and the ability to determine the total energy of a reconstructed shower depend critically on being able to convert an ADC count to a light flux for each pixel that receives a portion of the signal from a shower. To this end, it is highly desirable to have some method for evaluating each pixel's response to a given flux of incident photons from the solid angle covered by that pixel, including effects of diaphragm area projection, optical filter transmittance, mirror reflectivity, pixel light collection efficiency and area, cathode quantum efficiency, PMT gain, pre-amp and amplifier gains, and digital conversion. While this response could be assembled from independently measured quantities for each of these effects, the FD calibration group is persuing an alternative method in which the cumulative effect is measured in a single end-to-end calibration.

The technique being developed is based on a portable light source that will mount on the external wall of the fluorescence detector building, filling the diaphragm of a mirror with a uniform pulsed flux of photons and triggering all the PMTs in the camera array. One portable light source will be stationed at each FD building. Cameras will be calibrated one at a time.

This source consists of a pulsed UV LED embedded in a small teflon sphere, illuminating the interior of a 2.5 m diameter cylindrical drum, 1.25 m deep. The sides and back surface of the drum are lined with Tyvek, a material diffusively reflective in the UV. The front face of the drum is made of thin sheet of teflon, which is diffusively transmitting. A silicon detector mounted near the LED monitors the relative intensity of each flash.

The geometry of the source and drum is arranged so that the intensity is independent of position on the diaphragm and uniform over the range of the camera's solid angle. These uniformities of intensity and angular emission are measured in a laboratory using a CCD camera, viewing the drum from a distance of 15 m. Pictures are recorded for several angles of emission from the drum, in the range of the telescope field of view. Software has been been developed for comparing the relative intensities of regions of the drum surface. Current drum geometry gives non-uniformities of less than 5%. The largest non-uniformity is a decreasing intensity with radius on the drum face. While perfect uniformity is desirable, non-uniformities which are small and well mapped over the surface of the drum can be accommodated in analysis.

Ideally, this calibration would occur at many wavelengths in the N_2 spectrum, between 300 and 400 nm, and at several intensities. The design discussed above uses the single wavelength of the UV LED (375±12 nm). It is planned that, as the calibration sophistication evolves, fiber optics will be used to pipe light to the teflon sphere, allowing selection of frequency and intensity from a light source such as a monochromator or filtered xenon source. Currently, the pulses are variable in width, from 500 ns to 7 μs.

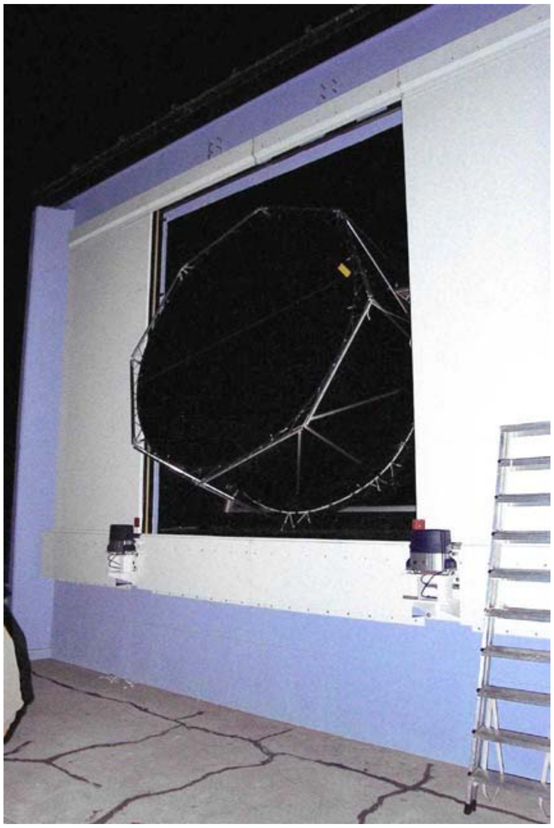

Figure 1.22 Drum calibration device mounted on the outside of the building at Los Leones.

1.1.9.1.2 Calibrating the Drum Using the Central Calibration Facility

While the uniform light source described above provides a means of determining relative responses of the pixels in a telescope, measuring the energy of an air shower requires an absolute calibration of pixels. To accomplish this, the drum calibration must also be absolute.

To establish this absolute calibration, a small optics lab will be established at the central Auger assembly building. The basic lab components will include a molecular deuterium UV light source, a diffraction grating monochromator, beam splitter, and a NIST-calibrated UV silicon detector. This Si detector will be the reference standard for the calibration. The lab components will be used to transfer the NIST calibration from the Si detector to a PMT and then to the drum. (The low sensitivity of the Si detector makes it unusable for directly calibrating the drum.)

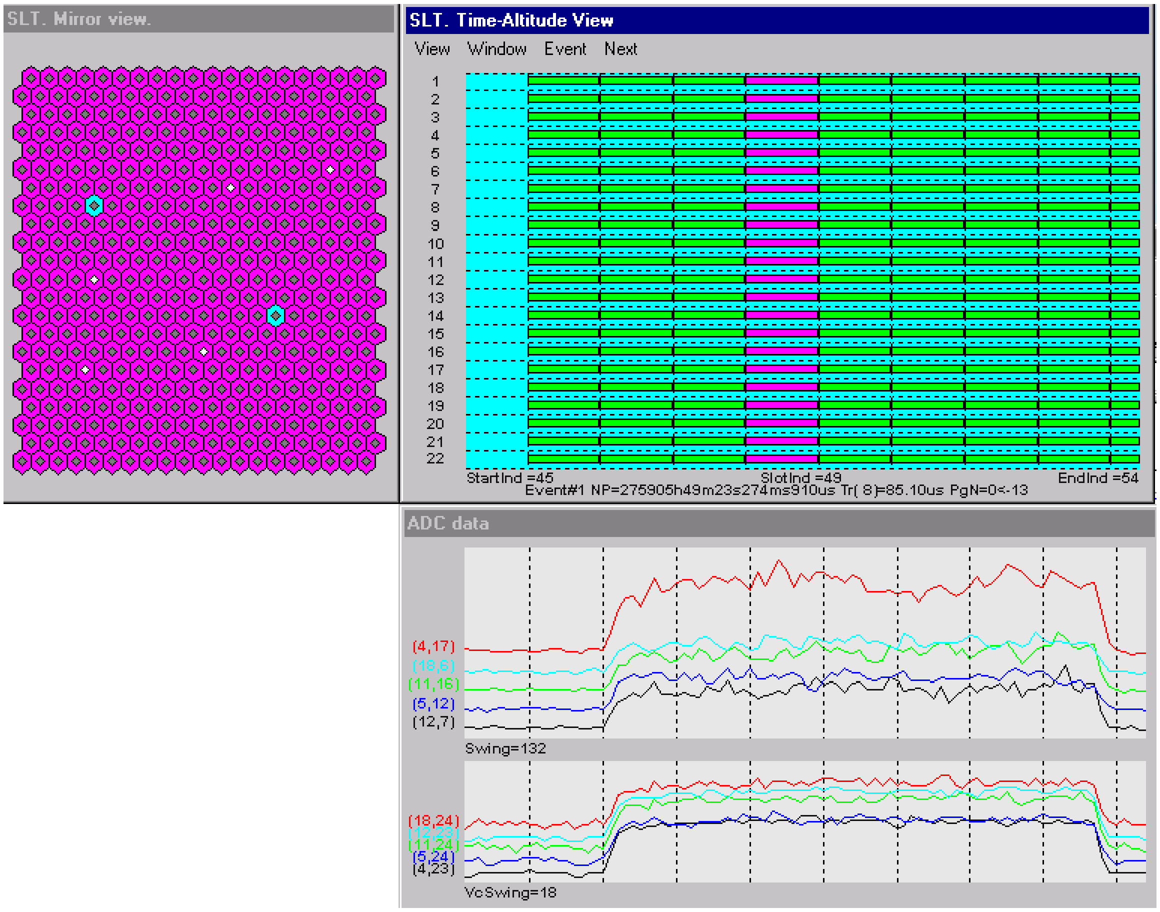

StartInd =45 SlotInd =49 EndInd =54
Event#1 NP=275905h49m23s274ms910us Tr(8)=85.10us PgN=0<-13

Figure 1.23 The online display from the data acquisition software showing the results of a single 7 μs pulse from the calibration drum when mounted in the mirror aperture. At the top left is shown the pixel array, indicating that all pixels in the camera (except two known dead channels at this time) went above threshold. Top right contains timing information for the triggers in each row of pixels. Bottom is the response from several randomly selected pixels in the camera (dotted pixels in top left) for the seven 1 μs ADC bins. Such events can be written to disk at about 10 Hz; several thousand events at 5 pulse widths from 0.5 to 7 μs have been written to disk for analysis.

The first step in the calibration will be made using techniques paralleling those used by NIST [15], where the detector to be calibrated is compared to the known standard detector under identical conditions. The monochromator will scan UV wavelengths between 300 and 400 nm using the molecular deuterium source as input. The beam splitter sits at the monochromator output. With the Si reference standard and the PMT monitor viewing the two beams from the splitter, detector outputs as a function of wavelength can be compared. (To allow for the ~10^6 difference in detector sensitivity, a neutral density filter is required on the PMT beam.) A ratio of the outputs (including the measured nuetral density filter factor) at a given wavelength gives the calibration of the detector relative to the standard at that wavelength.

The uncertainty in the calibration of the PMT will include the uncertainty in the UV Si detector calibration, provided by NIST. The wavelength-dependent efficiency uncertainties are given in Table 1.2.

wavelength (nm)	uncertainty (%)
200	13.02
250	1.36
300	2.06
350	1.68
400	1.46
450	0.38
500	0.38

Table 1.2 NIST wavelength-dependent efficiency uncertainties for the UV Silicon detector.

Once the PMT response is known, it can be used to calibrate the (low) intensity of the drum. If the PMT is placed far from the drum, photon incidence angle effects are minimized. It has been shown in the lab that the response of a suitable PMT to light emitted by UV LED pulses in the drum can lead to measurements which are good (statistically) at the 1% level.

The uncertainty in the overall calibration is expected to have contributions from uncertainties in the stability of the LED-monitoring Si detector in the field, the uniformity of the diffuse surface of the light source, and the cumulative uncertainties of calibrating the drum relative to the UV Si calibration detector through use of the PMT. Of these, the first and the second, which can be minimized in software, are expected to be small. The last is expected to dominate the overall uncertainty. Since each of these is expected to be less than 5%, a total absolute uncertainty on the order of 8% or less is expected.

1.1.9.1.3 Relative Night to Night Calibration

The end-to-end calibration using the flat field drum illuminator (described above) will be done on a periodic but not on a nightly basis. To track the PMT response between end-to-end calibrations, a relative optical calibration system provides light pulses to three computer-selectable places in each FD telescope:

- at the mirror center with the light directed at the camera;
- at the middle of the 2 sides of the camera with the light directed at the mirrors;
- at the entrance aperture with the light directed at a reflector (TYVEK screen or TYVEK targets on the telescope doors) to direct light back into the telescope entrance aperture.

The light is distributed from a programmable light source (at each FD site) via optical fibers. Typically the optical fibers end with a diffuser to equalize the light directed to the PMTs. The geometrical projection effects (for the fiber/diffuser at the mirror center) can be calculated, thus this source provides a relative calibration of the camera pixels within a single camera.

The programmable light source provides light at different intensities and/or wavelengths using neutral density and/or interference filters respectively. The light source is a xenon flash bulb with a characteristic pulse time of ~ 1μs matched to typical fluorescence signals in the PMTs. The high pulse to pulse stability of a xenon light source results in light calibration signals with RMS widths < 1%. Light source intensities are monitored and recorded in the calibration data base.

1.1.9.2 Options and Development Work

The prototype telescope will be a test bed for numerous calibration ideas. The flat field drum illuminator concept is one example of an attempt at end-to-end calibration. Other schemes may turn out to be superior to this.

1.1.10 Atmospheric monitoring

The observed light intensity, I, from a shower is reduced from the light intensity of the fluorescence source, I_0, by geometric and by transmission factors. The relevant transmission factors are T^m and T^a corresponding to *molecular* and *aerosol* scattering of the light in the atmosphere between the air shower and the fluorescence detector(s). There are also higher order corrections from multiple-scattered light and scattered air Cherenkov light (that increase the observed signal somewhat). Uncertainties in the source light intensity will arise from uncertainties in the (correction) factors. To minimize these atmospheric uncertainties, fluorescence experiments are located in dry desert areas with typically excellent visibility (*i.e.* small corrections).

The scattering of light in a pure or molecular atmosphere is from Rayleigh scattering. The scattering of light on much larger scattering centers in the atmosphere called aerosols is referred to as Mie scattering. In practice the Rayleigh scattering related corrections, while large, can be made with precision using conventional atmospheric data: the temperature and pressure at the fluorescence detectors, and the adiabatic model for the atmosphere. In contrast the corrections related to Mie scattering, while typically less than the Rayleigh corrections, are *a priori* unknown. Thus most of the atmospheric monitoring is focused on the aerosol (Mie scattering) component.

In a 1-dimensional model of the atmosphere (not un-typical of the night time atmosphere in large, desert valleys at locations well away from the valley walls) two quantities of the aerosols must be measured to make the transmission correction: the aerosol horizontal extinction length (at the altitude of the fluorescence detector sites) and the aerosol optical depth to height z above the fluorescence detectors. These will be measured using dedicated instruments. In all cases the measured quantities include both aerosol and molecular contributions. The aerosol values are obtained by subtracting the molecular (Rayleigh) contributions.

1.1.10.1 Reference Design Specifications

1.1.10.1.1 Weather recording

Automated weather stations will be located at each of the FD sites (eyes). They will provide a record of the local temperature, pressure, wind speed and direction, and humidity. The temperature and pressure are essential to define the *Rayleigh* atmosphere. Wind speed (and direction) are important for safety interlocks for the FDs. Humidity is relevant for the IR cloud cameras and provides information on the formation of fog.

1.1.10.1.2 Horizontal attenuation

The horizontal attenuation length will be measured at 1 hour time intervals and along 3 (independent) light paths across the Auger Southern array. Thus they will provide information on site and instrument-related systematic uncertainties in the horizontal extinction length. Each light path includes a Hg-vapor light source and a CCD based receiver. The receivers are ~50 km from the source to minimize the uncertainty in the horizontal attenuation length measurement from variations in the source brightness or photometer sensitivity. Measurements will be done at 4 wavelength between 365 and 546nm. These measurements, combined with the local temperature and pressure, will determine the aerosol horizontal attenuation length at 365nm and the wavelength dependence of the attenuation length.

1.1.10.1.3 Vertical aerosol profile

The observed fluorescence light signal must be corrected for the finite transmission of light from the extensive air shower to the fluorescence telescopes. To make this correction we need to know the cross section weighted, vertical profile of the atmosphere, and in particular of the aerosols. The plan is to use scattered laser light as a light source to monitor the atmosphere. By using steerable laser beams, the light sources can be positioned to make a measurement of the vertical optical depth versus height, *z*, above the fluorescence eyes. In practice this will be done using backscattered LIDARs. Backscattered LIDARs will be installed at each of the three fluorescence sites on the periphery of the Auger ground array. Each backscattered LIDAR consists of a pulsed, 355nm, laser beam and a receiver telescope. Comparison of the three LIDAR results will monitor site and instrument related systematic uncertainties in the optical depth measurements.

1.1.10.1.4 Aerosol phase function

The observed light from an extensive air shower includes both the air fluorescence signal plus some Cherenkov light (mostly in a few degree cone centered on the air shower axis). Through scattering of the Cherenkov light in the air, some of the Cherenkov light appears as a background into the fluorescence data. To estimate the fraction of Cherenkov light scattered on aerosols we need the aerosol extinction length, at height *z* above the fluorescence detectors, and the aerosol phase function (normalized aerosol differential scattering cross section) for scattering angles $\geq 10^{O}$ (from the initial light direction).

The observed light from an extensive air shower also includes a contribution of multiple scattered light. This will be true for the air fluorescence signal and for the Cherenkov background light. In making a correction, it is most important to know the Mie phase function at forward scattering angles where Mie dominates Rayleigh scattering.

In the constant composition, 1-dimensional model for aerosols, it is sufficient to measure the aerosol phase function at the altitude of the fluorescence detectors. The measurement can then be made using a near-horizontal, pulsed light beam directed across the field of view of one of the fluorescence sites. As each fluorescence detector views $\sim 180^{O}$ in azimuth, even a fixed direction light beam will allow the aerosol phase function to be measured over most of the range of scattering angles. This will be done using a dedicated light source located near two of the Auger fluorescence sites. In addition LIDAR beams, from one fluorescence site directed across the field of view (and at near grazing incidence to) adjacent fluorescence sites, provide a good measurement of the small angle aerosol phase function.

1.1.10.1.5 Cross Checks

To monitor and to help minimize systematic uncertainties, all of the atmospheric monitoring measurements are made in at least two independent ways. For example the horizontal extinction length measurement will be compared with horizontal LIDAR measurements. The aerosol optical depth measurement will be compared to measurements from a dedicated star monitor. In addition laser *side* scattered light from the LIDAR at one fluorescence site will be observed by the fluorescence detector at a different fluorescence site. A comparison of the predicted *versus* observed signal (as a function of time) provides the essential cross-check of the aerosol model and the ingredients of the model: the horizontal extinction length, the vertical profile of aerosols and the aerosol phase function.

In addition spatial variations in the aerosols are monitored using the 3 different horizontal attenuation length light paths and by the azimuthal variations in the backscattered LIDAR measurements at a given site and by differences in the vertical optical depth as measured at the 3 LIDARs.

1.1.10.1.6 Cloud Monitoring

The presence of cloud is a key factor in the operation of the FD system. It can determine the effective aperture of the system, and the presence of broken cloud between the shower track and an eye can distort the apparent longitudinal development of individual showers. Cloud can be detected at night in the absence of terrestrial light sources by its emission in the infra-red due to its higher temperature than the night-sky background. Apart from the highest and coldest cloud, such detection can be readily achieved for cloud at high at high elevation angles. Close to the horizon, particularly in humid conditions, detection against the warm atmosphere may be more difficult. The plan is to install infra-red (in the vicinity of 10µm) cameras at each of the FD eyes, and to scan the sky with them using a pan and tilt drive approximately every 10 minutes. They will provide each FD pixel with a cloud/cloud-free decision and, with a 0.2^{O} angular resolution, will be used collectively to triangulate sparse cloud over the array fiducial volume. A test image is shown in Figure 1.24.

Figure 1.24 A cloud image taken with a Raytheon Series 2000B camera from the top of the physics building in Adelaide - looking north-east. Its a pyroelectric 320 x 240 pixel camera sensitive to 7-14µm infra-red radiation. A negative image is shown - dark (cloud) areas are warm compared to white (clear sky) areas. The image shows cumulus cloud low over the Adelaide Hills - at least 10 km distant. Some closer cumulus is evident in the middle of the image. This foreground cumulus is in front of some higher altitude diffuse/cirrus type cloud (faintly visible in the upper centre of the image). On the left is part of the physics building and in the lower right a construction crane. The horizon is the Adelaide Hills.

1.2 FLUORESCENCE DETECTOR ELECTRONICS AND SOFTWARE

Overview

The organization of the electronics follows the geometric structure of the detector. One telescope system of 30º x 30º is readout by one front-end sub-rack with its associated Mirror-PC. Each sub-rack covers 22 x 20 pixels and contains 20 First Level Trigger (FLT) boards and one Second Level Trigger (SLT) board. The overall system consists of 30 Schmidt telescopes with 13200 channels to be readout. The telescopes are distributed over 5 fluorescence detector eye stations: the 3 perimeter eyes and two central eyes. Each eye stations is composed of 6 telescopes and covers a 180° x 30° sky region.

The contradicting requests of the experiment are a challenge for the design [16]:

- low price,
- good testability to achieve remote operation and to save operation costs,
- high reliability and robustness for 20 years of operation,
- absolute time correlation with the surface array stations of < 120 ns,
- flexibility of the triggers to be open to new physics.

The main tasks of the telescope electronics are to shape the PMT signals, digitize and store it, form a trigger based on the camera image and initiate the readout of the stored data. A computer network compresses the data, improves the trigger decision, gathers data of the same event from different telescopes and transfers it to the central computing facility of the experiment.

The concept for the front-end electronics, the data flow and the data processing rests upon the system requirements. The design uses reprogrammable FPGAs to obtain a *cost-effective* and *flexible* solution whenever possible. The large-scale integration of modern FPGA allowed a massive parallel solution for recognition of tracks and suppression of background. The supervision task and readout is carried out by low cost PCs under LINUX operating system. Using this concept we are able to fulfil the first and last request of our design goals, low price and flexibility.

This chapter of the report describes the electronics systems, the trigger, the computing facilities and the software associated with each of the front-end sub-racks. Figure 1.25 shows the block diagram of the eye electronics and readout system. Following the signal chain from the PMT to the central side the system consists of 4 main parts:

- camera with 440 PMT's and the head electronics as shown in Figure 1.26,
- front-end sub-racks, commercial 19” VME racks containing the analog and digital front-end boards,
- DAQ-subnet, linking the Mirror-PCs with the Eye-PC via a LAN switch, and
- Eye network to the telecommunication tower and the Field PC (used for slow control).

All these hardware parts and the software are explained in detail in the following subsections.

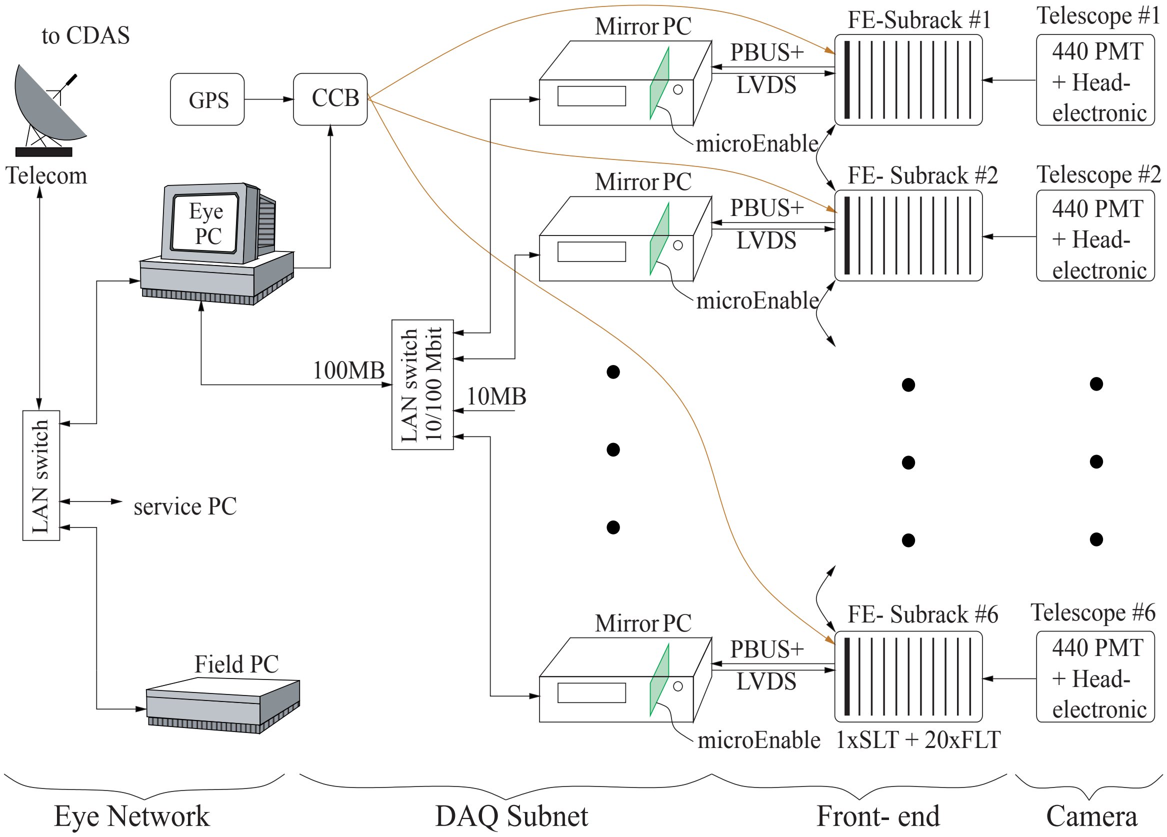

Figure 1.25 Readout scheme for the FD electronics showing the main components Eye Network, DAQ subnet and front-end sub-racks.

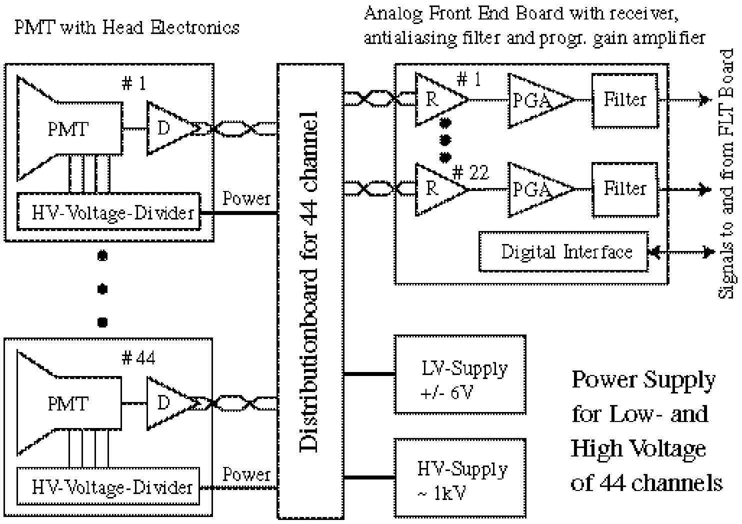

Figure 1.26 Block diagram of Head Electronics, Distribution Board (DB) and Analog Board (AB)

1.2.1 Hardware

1.2.1.1 Head Electronics

Overview

The Head Electronics (HE) is the first unit of the signal processing chain. It converts the FD signal current into a differential voltage pulse and the mean background current into a common-mode voltage level. Both the pulse and the DC level are conveyed to the Analog Board using a single twisted pair per channel.

The HE unit is mounted directly to the PMT (Figure 1.27) and its circuitry provides the following functionalities:

- PMT biasing
- Signal preamplification and twisted pair driving
- Rejection of common-mode noise
- Monitoring the DC component of the anode current
- Test pulse injection
- HV filtering.

The HE consists of three coaxially interconnected PCBs: the Bias PCB close to the PMT, the CM/Driver PCB in the middle, and the outer Interface PCB. All PCB's are two-sided, circular, 32 mm in diameter, and are interconnected using high reliability pin connectors.

A full description of the Head Electronics is given in http://pcauger02.mi.infn.it/documents.html.

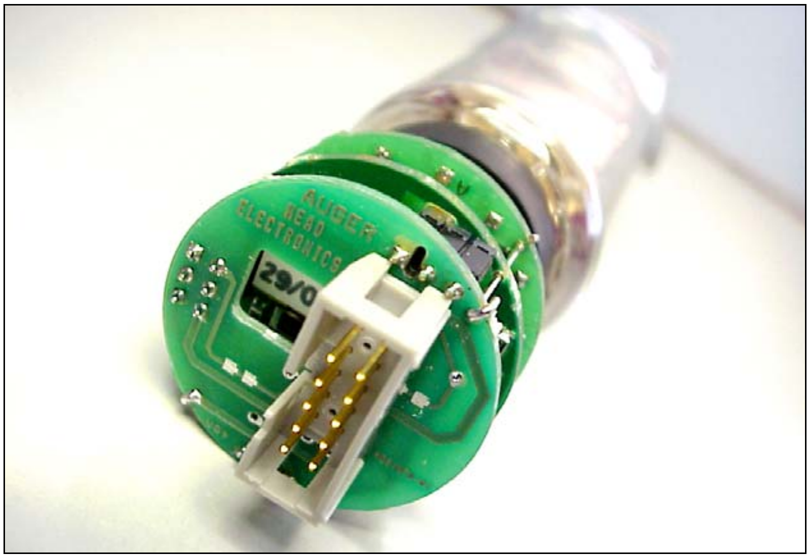

Figure 1.27 A Head Electronics unit connected to an XP3062 PMT. Each unit has a serial number for identification and tracing during its life. The units are connected to the Distribution Board via a ~30 cm cable.

The bias PCB

The PMT is biased using an active divider network equivalent to a 6.35 MOhm resistor. The active divider allows constant PMT gain even at large background currents, as well as reduced power dissipation. The low power consumption translates into a significant reduction in the cost of the HV power supply. In addition the lower operating temperature improves reliability. A comparison between the active divider and a conventional passive scheme is shown in Figure 1.28.

Signal preamplification and twisted pair driving

PMT signal current is converted into a voltage pulse by a load resistance of 500 Ohm so that the maximum signal at the driver's output is 5 V. A differential input, balanced output chip, MAX 4147ESD, reads the single-ended current signal from the PMT adding minimum noise. A differential input is used in combination with a symmetrical load resistor network to allow high rejection of common-mode noise, Figure 1.29.

The differential output is biased to a common-mode voltage of ~ 1.9 V. In this way the unipolar fluorescence signal takes better profit of the available linear region. The Maxim chip drives a twisted pair cable which, after traversing the distribution board at the camera, ends with a differential line receiver MAX4145ESD at the AB. Two diodes (not shown), provide protection against HV sparks at the anode. The HE can withstand short circuits to ground at the output without damage.

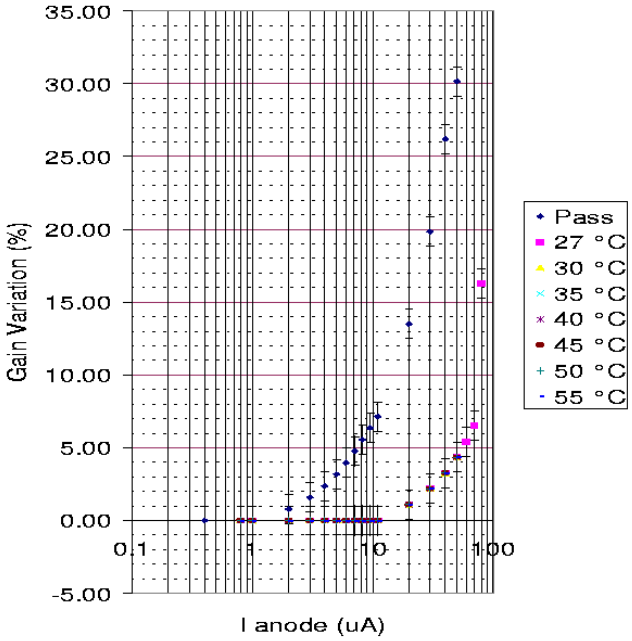

Figure 1.28 PMT gain variation for a passive bias network passing 270 μA and for an active one passing 144 μA, at different temperatures. At 20μA the passive network has a ~ 14% gain change while it is only 1 % with the active network.

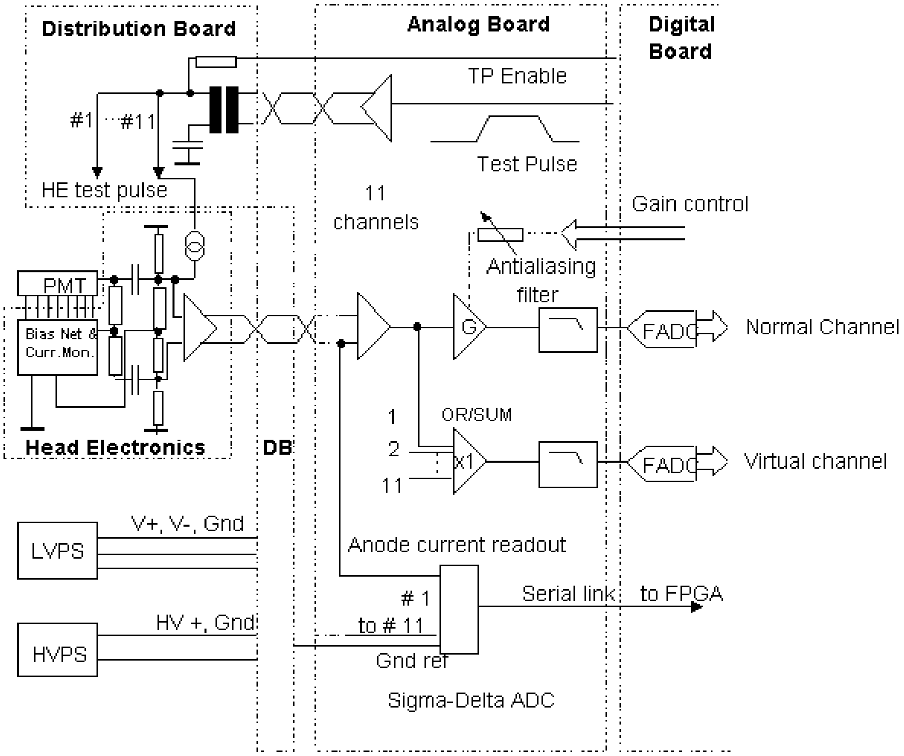

Figure 1.29 Block diagram of the Head Electronics unit and its connection to the AB.

Rejection of common-mode noise

Possible sources of common-mode noise are electromagnetic interference (EMI) generated by digital circuits and HVPS noise. Use of a symmetrical load resistor network allows, below 100 kHz, a ratio x 25 (28 dB) of common-mode noise rejection. In particular the low-frequency component of the HVPS is better rejected as, at low frequency, the HV filter is less efficient.

Monitoring the DC component of the anode current

The HE unit allows taking periodical records of the average background light in every pixel. This provides important information to perform the following actions:

- evaluate the sky quality (presence of clouds, atmospheric attenuation, presence of light sources).
- control the stability of the absolute pointing of the telescope pixels by tracking bright blue stars.
- evaluate the spot size by analyzing the signal of a star traversing the camera.
- explore alternative absolute calibration of the optics and PMT systems by simultaneous measurement of reference stars.
- evaluate the amount of coherent noise by correlating direct background measurements with baseline fluctuations.

The current monitor (CM) generates a voltage level linearly related to the average illumination in every pixel [17]. This level appears as a common-mode DC voltage at the twisted pair delivering the signal of that pixel. Four low-cost 16 bit sigma-delta ADC chips (AD73360) at the FEB read out CM pedestals and its deviations under illumination for all 22 pixels in a column with a 0.5 % resolution. The sensitivity to the background current is known with 1 % precision for every individual pixel. A typical plot of the DC voltage at the twisted pair for a bright star crossing the PMT field is shown in Figure 1.30. Stars of magnitude 5.4 are clearly visible.

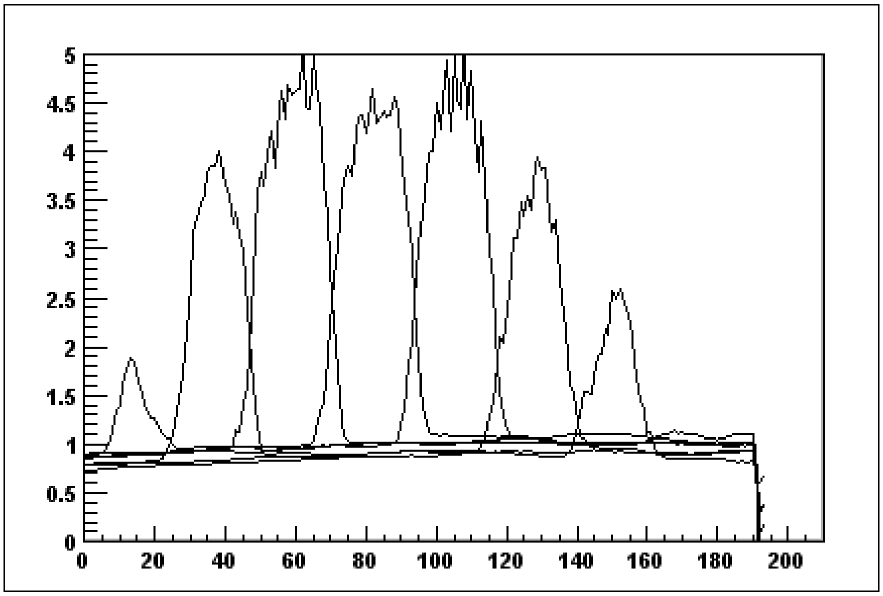

Figure 1.30 A bright star (Vega) crossing the FD Camera. The anode current in µA at different adjacent pixels is plotted as a function of time, with the time axis in units of 20s. The pulse width at half maximum was about 6 minutes. The pedestals of each pixel correspond to the dark sky light.

Test pulse injection

The HE includes a test-pulse (TP) input to allow the injection of a current pulse directly at the preamplifier's input. In this way an FD signal is emulated so that a clear distinction between the optical and electrical response to a real FD signal can be performed. The TP is produced by a pulse generator capable of generating any desired pulse shape: step, delta or a generic FD shape. A TP signal for every group of 11 channels is sent via a single twisted pair from the AB to the DB. There a pulse transformer drives the TP input of all 11 channels in parallel. The superimposition of the responses of all the 11 channels pulsed in parallel shown in Figure 1.31.

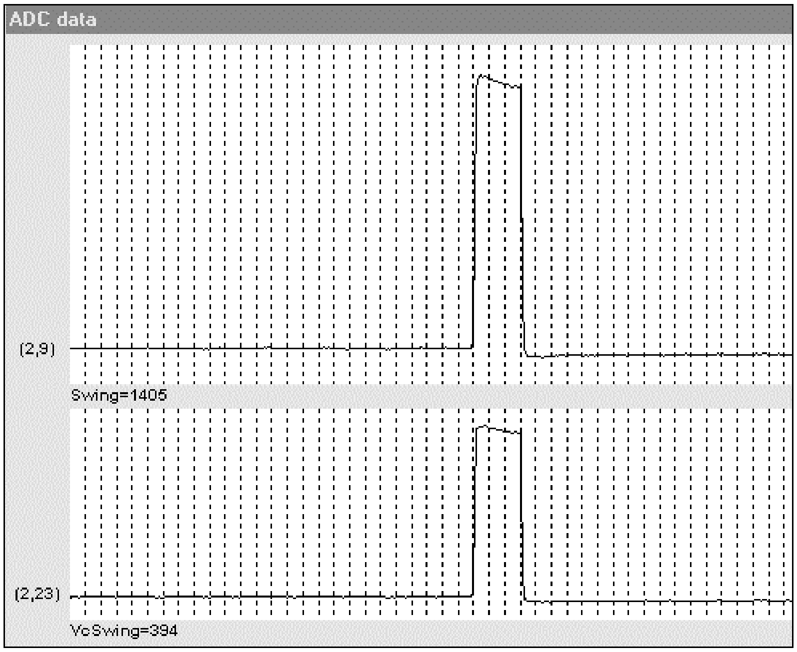

Figure 1.31 Response to a test pulse in the normal (top) and in the virtual channel (bottom). In the virtual channel 11 channels summed up are shown.

Interface HE -distribution board

The outermost PCB (interface PCB) accepts the cable coming from the Distribution Board; also it provides a mechanical protection for the circuitry against damage that may occur during mounting or servicing of the camera (Figure 1.27).

The Interface PCB is connected to the CM/Driver PCB via three Samtec low-profile connectors which provide HV, GND, +/-LV, GND, +Vout/- Vout and TP input. A 10pin 3M connector on the opposite side allows the connection to the Distribution Board. The mechanical rigidity is assured by locking the three PCBs of the HE together by two wires.

Quality assurance

The following measures are taken to assure uniformity of performance and reliability:

The HE unit uses feedback networks with high loop gain, which assures best uniformity. For the HE fabrication, IC's and discrete active and passive components of well-known producers (Maxim, Siemens, Toshiba, Zetex, Analog Devices, AVX, Philips) are used. Connectors were chosen from those which guarantee best reliability (Samtec). Resistors have a tolerance of 1 %. The only two electrolytic capacitors are Siemens Matsushita recommended for applications in extreme environments (high temperature). It is envisaged to substitute them by TDK high capacitance ceramic capacitors. PCB's comply with standard ISO 9002; components are mounted mostly using pick-and-place techniques, with the exception of some connectors.

Acceptance test

After production each unit is labelled and identified by its serial number and date of the batch production run. An acceptance test and a zeroing procedure were devised [18] to check and determine the dispersion of various critical parameters about their expected values in the fabricated lot. A significant deviation in a unit would be an early indication of possible failure and therefore such a unit would not be qualified. This is a more stringent criterion than looking for units that already exhibit a failure. Test jigs and related software have been developed and are performed using a semiautomatic set up. A database with all the records taken of every single unit is produced. A completely automatic set up for the test, to be performed by the producing factory itself, will be used during the HE mass production.

Table 1.3 below displays the statistics referring to the two last HE batches tested. Figure 1.32 shows a typical result of the acceptance test.

Table 1.3 Statistics for 811 HE units in the two batches, August 2000 and January 2001. Dispersions are quite low.

HE batches 35/00 01/01	I(-6) mA	I(+6) mA	Vout ped V	c.m. anode sensitivity mV/µA	c.m. cathode sensitivity mV/phel/100ns/ G=10^4	Eq Rgrid KOhm	R18 KOhm
average	11.45	34.11	1.91	60.67	0.97	26.03	267.75
stdev	0.45	1.12	0.03	1.67	0.03	0.81	
σ%	3.89%	3.29%	1.44%	2.75%	2.75%	3.13%	
max	12.43	38.91	1.98	64.95	1.04	27.93	680
min	9.75	31.13	1.78	57.93	0.93	24.11	140

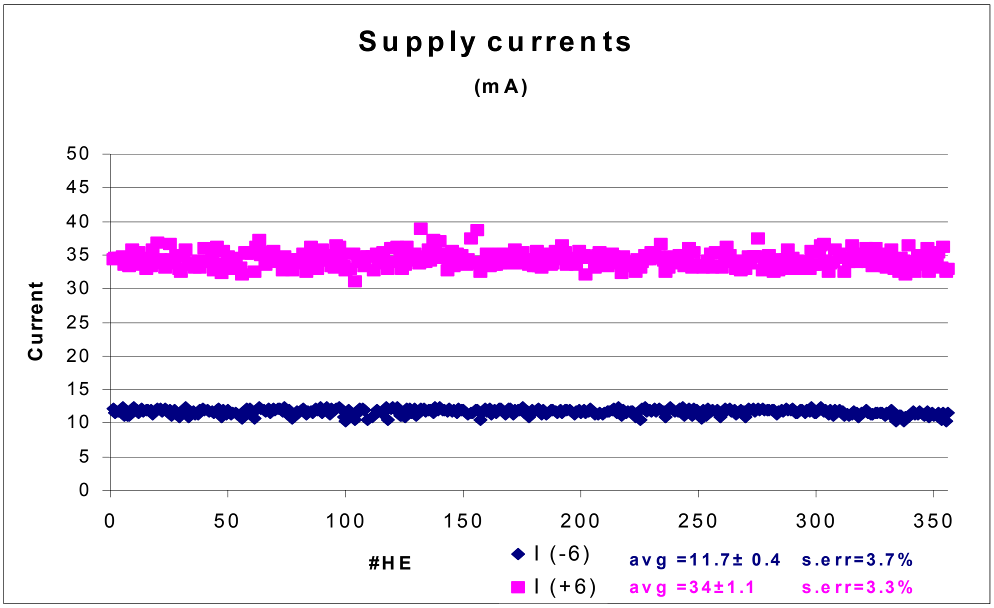

Figure 1.32 A typical plot of parameters determined at the acceptance test. The larger consumption of some units may be an early indication of failure therefore these units are not qualified.

Burn-in test

A burn-in test of all Head Electronics units is foreseen to accelerate age stressing and screen those units susceptible to die of infant mortality. The units are mounted onto a PCB, specially designed to provide both HV and LV bias (914 V nominal HV bias, ±6 V LV) and to monitor power supply current of groups of 11 units. The DC common mode voltage and the differential voltage at the HE output wires are recorded for all units. A HP 34970A scanner runs under control of a LabView Data Acquisition software. A climatic chamber (Votsch VT7010) will be used to control the temperature.

A first burn-in test was conducted in 40 units, half of which HV biased. This subset showed a continuous drift in the output pedestal voltage due to stress. At 25°C the value was almost constant (1.95 V), at 40°C the pedestal voltage drifted 27 mV in 18 hours from the starting value of 1.92 V; the drift increased at 60°C until, after 12 hours, it assumed an almost constant value of 1.7 Volts.

After the burn-in test all the units were still working. A total pedestal shift of 141 mV was measured. This value is totally negligible as the pedestal value is always measured at the beginning of data taking, in dark conditions.

Figure 1.33 shows the plot of the output pedestal voltage drift during the 125 hours the burn-in test lasted.

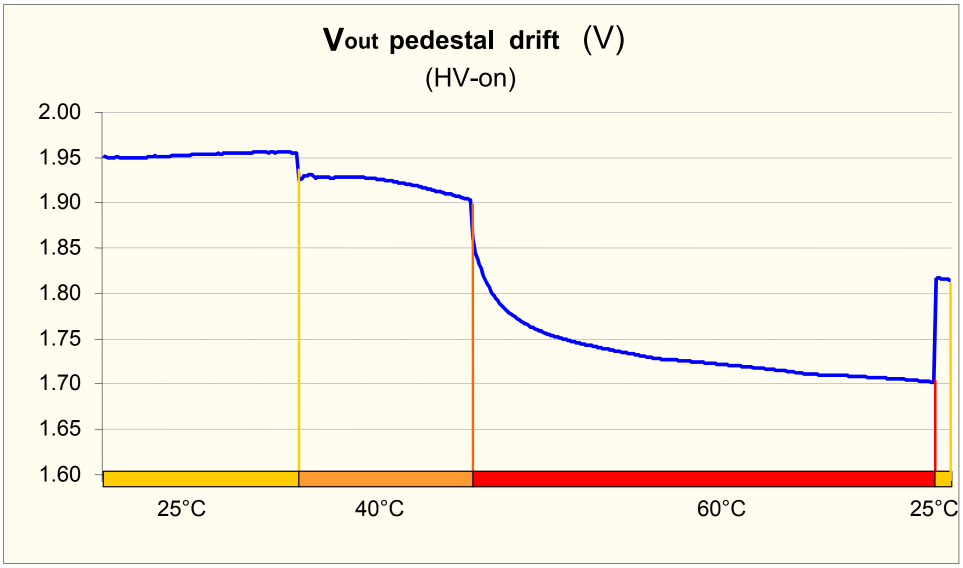

Figure 1.33 Drift of DC pedestal output voltage during the first burn-in test; the total burn-in time was 125 hours. A total shift of 141mV (7%) was observed after returning to 25°C.

Head Electronics specifications

Table 1.4 HE specifications

General:	
Low voltage supply	+6 V/34.0 mA -6 V/11.6 mA
HV supply current (for R9 = 100 K)	144 µA @ 914 V (equivalent resistance: 6.35MOhm)
Total power dissipation	406 mW @ HV = 914 V
Signal Driver:	
Output	Differential
Total output resistance	118 Ohm
DC common mode voltage	1.9 V @ Ia =0
Signal gain	500 mV/mA (RL = 500 Ohm)
Maximum current signal	5 mA
Bandwidth	1kHz->12 MHz
White voltage noise density level	9 nV/√Hz (f > 3 kHz) equivalent to: 18 pA/√Hz noise current at the anode.
Common-mode rejection ratio (CMRR)	28 dB from 1kHz to 100kHz
Current Monitor:	
Sensitivity (Rf=180K)	(61+/-1.7)mV/µA referred to anode current or 0.97 mV/phel/100ns/Gain/10^4
Anode current range	0- 25µA
Voltage Range	(1.90 +/- 0.02) V @ Ia=0 0.4 V @ Ia=25µA
Bandwidth	10 Hz
Noise referred to DC anode current	80 pA
Resolution with 16 bit Σ−δ readout	500 pA

Test pulse:	
Maximum amplitude	5 mA (for a 5 V external pulse, negative swing)
PMT Bias:	
Type of divider	Active
Divider current	144 μA @ 900V anode voltage.
Gain change	Negligible up to Ia = 10 μA; 2 % @ Ia = 20 μA 5% @ Ia = 50 μA
Maximum Voltage	Tested to 1500 V

1.2.1.2 Distribution Board

General

The AB and the HE units are interfaced via the Distribution Board and related cabling. The FD signal from each pixel is conveyed to the AB in differential mode. The mean PMT anode current (sky background) signal is sent to the AB as a common-mode voltage level using the same wiring. A test-pulse signal generated at the AB is sent to the DB where it is distributed to a group of 11 pixels in parallel.

HV and LV supplied to the PMT and HE pass trough the DB which provides protection against surges at the LV and to accidental reverse polarity in the LV and HV supplies.

The modularity is such that each DB serves four vertical pixel half-columns. An upper and a lower board are the minimum number required to read one complete column. Those two boards are related to four FEB's for a total of 88 channels.

The boards serve all four columns from the same side.

Cabling

AB to DB

A 26 twisted-pairs cable connects the AB to the DB. At the AB the cable plugs into the rear of the analog bus via a 64 pin connector (e.g. 3M 6964), using pin 1 to 26 and rows A and C. This cable is split in two and connected to the upper and lower DB's using two separate 30 pin connectors, of which pins 1 to 13 of both rows are used.

HE to DB

The connection between the DB and the HE is done via a single cable comprising 8 wires organized in twisted pairs:

signal Vo-, Vo+

HV, GND

Test, - 6 V

GND, + 6 V

The male connectors at the DB are implemented with 3M type 2x5 pins 2.54 mm pitch connectors. At the HE side, the same connector used at the DB is used in the Interface PCB which is the most external board of the HE.

Signal distribution

Pixel signals travel via twisted pairs in the cables and as balanced lines in the DB. The nominal impedance is 120 Ohm . Total lengths are reasonably equalized.

Test-pulse distribution

A test pulse is sent to a group of 11 channels of a DB, via one of the 13 twisted pairs. A second twisted pair transports the enable/disable and the GND reference signals.

At the DB, Figure 1.34, a pulse transformer receives the differential test pulse signal and drives in parallel the 11 TP inputs of the HE units in a column. Test pulses are disabled by default. For enabling, a –12 V level is sent from the AB to the DB via the Enable wire.

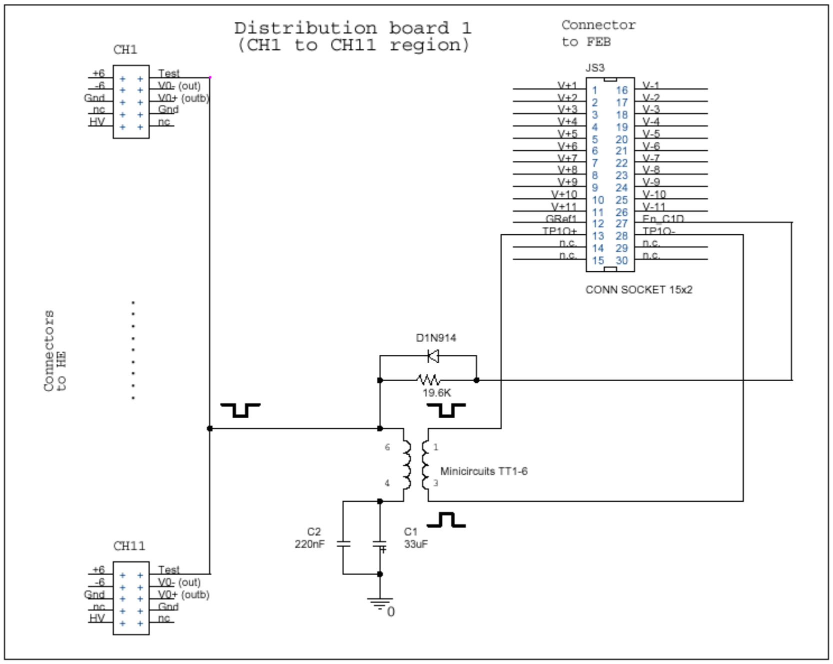

Figure 1.34 Test pulse distribution over 11 channels.

Protection

0.7 Ohm fuses are used for each LV line of the HE. They are mounted onto the DB. A 1W Zener diode at each LV leg per DB absorbs over-voltage surges. In addition the diode short circuits the power supply in case of accidental reverse-polarity connection. A HV diode provides protection against reverse-polarity in the HVPS (Figure 1.35).

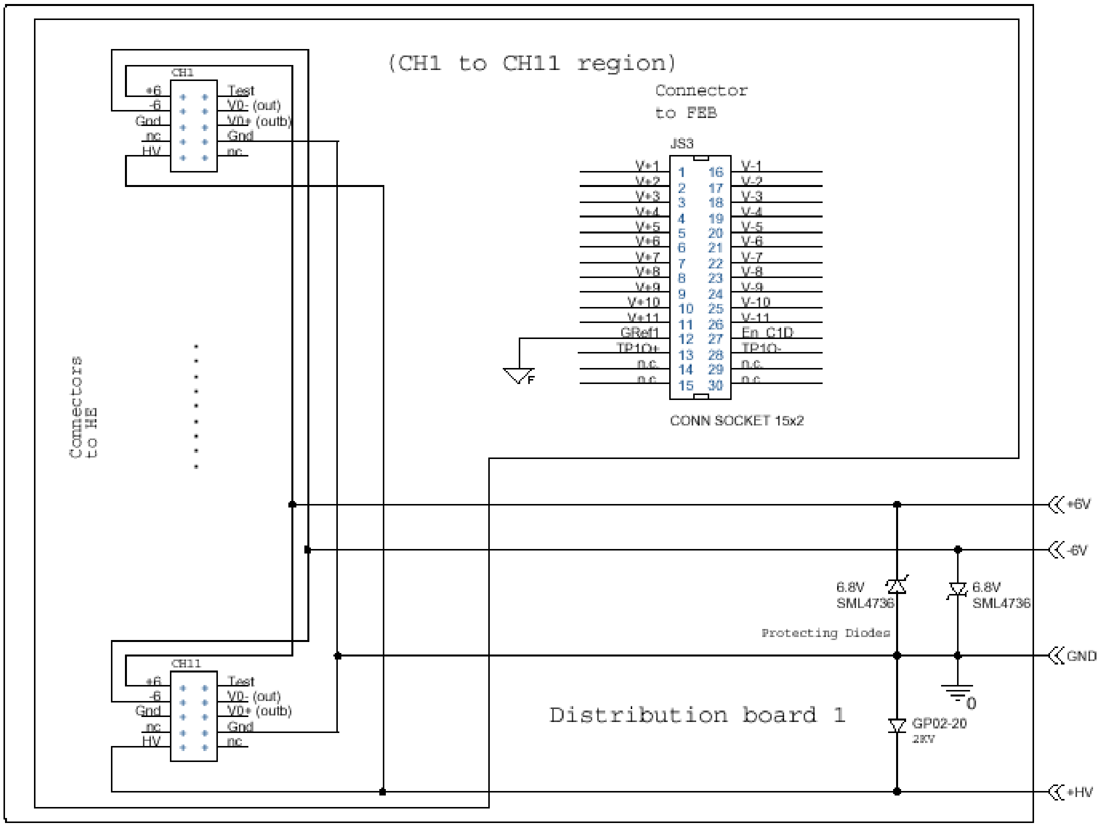

Figure 1.35 LV / HV distribution and protection devices.

Grounding

Each DB has four separate ground planes, one per column, each one associated with the AB reading that column. All four planes are connected together at one point as shown in Figure 1.36. Separate ground planes ensure minimum cross-talk and no ground loops.

A full description of the electrical HE-AB interface is given in http://pcauger02.mi.infn.it/documents.html.

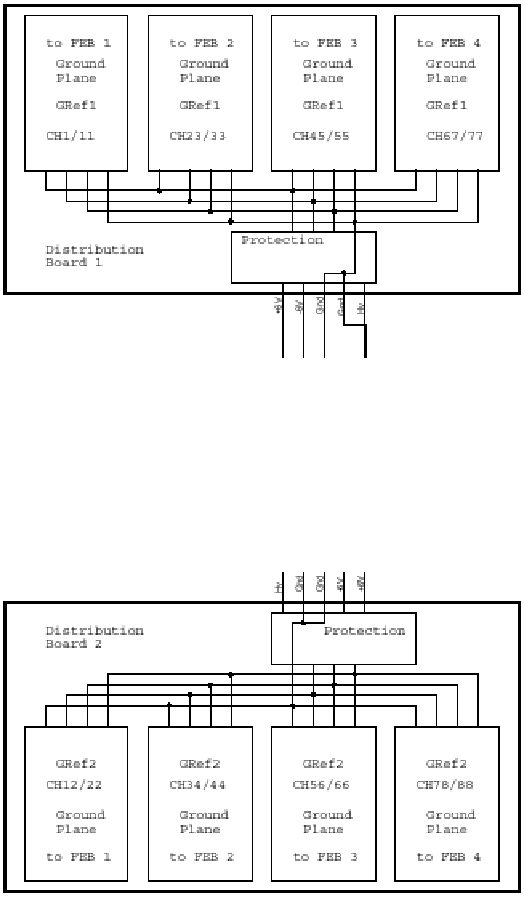

Figure 1.36 Each group of 11 channels has an associated ground plane. All four planes join at one single strip at the board.

1.2.1.3 Analog Board (AB)

Functional Overview

The Analog Board (AB) is located in the front-end sub-rack. It is connected via twisted pair cables to the Distribution Board and from there to the Head Electronics unit. The Analog Board processes these signals as described in the following and presents them to the ADC located in the First-Level Trigger (FLT).

The electronics blocks in the Analog Board [19,20] must:

a) receive the signals transmitted by the Head Electronics on the twisted-pair cables, performing a differential – to – single-ended conversion;

b) adjust the gain to compensate for the gain spread of the PMT's;

c) adapt the dynamic range of the PMT signals to the input dynamic range of the ADC;

d) provide an adequate signal filtering to prevent aliasing;

e) generate a test pulse to check the functionality of the whole electronic chain and perform its calibration ;

f) generate internal test patterns to test SLT functionality;

g) read out the DC level at the twisted pair cables, as it is linearly related to the background illumination at the pixel;

h) provide an adequate reliability for the operation on the site of the Auger Observatory.

Requirements

The requirements for the analog board are summarized below.

a) Mechanical requirements

   I) Number of channels per board: 22 (+2 Virtual Channels, see below)
   II) Board size: 3 U high, 220 mm deep

b) Operational requirements

   I) Operating temperature: 25 °C ± 3°C
   II) Power dissipation: < 350 mW per channel

c) Dynamic range

The system is designed to handle a 15 bit dynamic range of signals from the PMT's, with minimum signal corresponding to 3 photoelectrons in a 100 ns time slice. Considering a PMT gain of $3x10^4$, the amplitude of the PMT anode signals would vary between 144 nA and 4.7 mA. Simulations of EAS detection at the southern site [21] indicate that a 15-bit or even 14-bit signal dynamic range (our specification is 15 bit) might be acceptable, with a maximum signal amplitude of 98 k pe/100 ns (in fact it is 2^15 * 3 pe/100 ns). However, to make the dynamic pixel threshold adjustment scheme work properly, it is likely that the LSB will need to be about 0.75 p.e. The requirements on the signal dynamic range therefore require a compression scheme in order to work with a 12 bit ADC.

d) Noise performance

The analog processing has to preserve the shape of the signals (complying with the ADC antialiasing requirements), for timing and amplitude measurements, without introducing sizeable electronic noise.

We define an upper limit for the electronic noise, comparing it to the background sky noise: electronic noise, expressed in terms of noise current spectral density referred at the PMT anode, must be small compared to the current spectral density of sky noise. Referring the noise to an input current generator i_n in parallel with the PMT anode current signal, and by evaluating the power spectral density $\frac{d\overline{i_n^2}}{df}$ of this generator, we calculate the sky noise spectral density as:

$$\sqrt{\frac{d\overline{i_{sky}^2}}{df}} = 1.2 \cdot \sqrt{2qI_{sky}} \cdot G_{pmt} \cong 68 \frac{pA}{\sqrt{Hz}}$$

considering an average cathode background current $I_{sky} = 11.2$ pA, and a PMT gain of $3 \cdot 10^4$.

The factor 1.2 takes into account the excess noise due to the PMT electron multiplier.

e) Antialiasing filter specifications

According to the analysis carried out in [22], the order of the filter and its frequency cut should be chosen in order to minimize the residual error in the signal reconstruction from the samples taken by the ADC. As a design goal, the error has to be less than 5%.

f) Calibration requirements

Provision must be made for injecting a signal at the inputs of an arbitrary, remotely selectable set of channels. The signal amplitude and shape will also be remotely adjustable.

Circuit implementation

- Signal receiver

The differential to single-ended conversion will be done by a MAX4145 differential line receiver. Its noise contribution is small compared to the background sky noise, and its enable/disable capability will allow us to perform channel masking for trigger pattern simulations.

- Antialiasing filter

The analog channel outputs will be connected to ADCs which sample the signals at a 10 MHz frequency. It is well known that the samples accurately determine the signal if and only if the signal is limited in bandwidth within the Nyquist frequency (5 MHz). On the other hand, every practical filter limits the bandwidth only partially. In ref. [23] the residual error in the reconstruction of the amplitude from the samples is studied as a function of the filter order and of its cut-off frequency. It was shown that a 4th order filter with a 4.1 MHz cut-off frequency is adequate, considering the overall resolution requirements of the fluorescence detector. The frequency response of such a filter is shown in Figure 1.37.

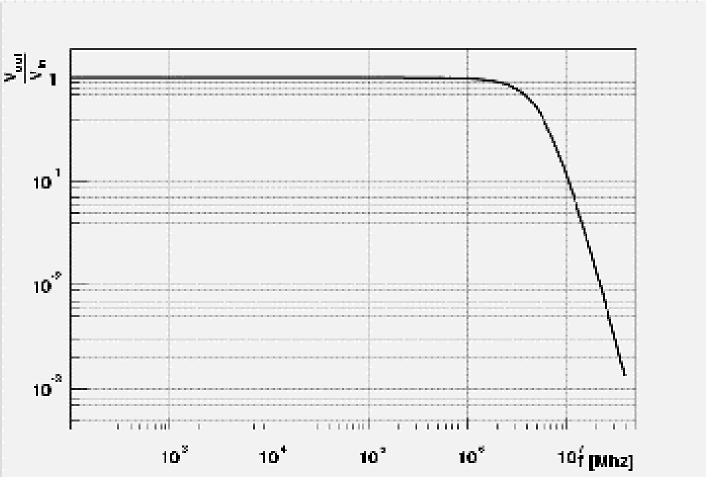

Figure 1.37 Frequency response of the anti-aliasing filter.

- Dynamic range adapter

To readout the 15-bit dynamic range signal with 12 bit ADC's, a dual gain system has to be implemented. Different solutions were discussed in ref. [24]. Two of them, not requiring custom chip developments, have been implemented in the first version of the prototype board:

the analog compressor and the virtual channel. The latter has been chosen because of its better characteristics in terms of power dissipation, circuit simplicity and noise performances.

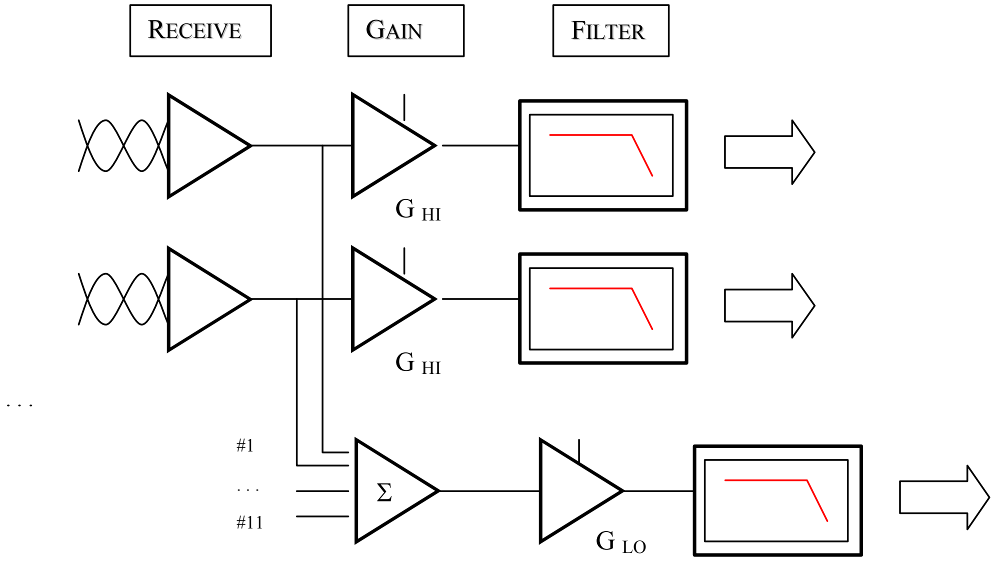

Figure 1.38 Block Diagram of the Analog Channel with the Virtual Channel for dynamic range adapting.

- Virtual channel

This dynamic range adapting scheme exploits the fact that the fluorescence detector signal appears sequentially in neighboring pixels. Large amplitude pulses (above 8192 p.e. per 100 ns, or 390 µA at the anode) will occupy, at the same 100 ns time slot, only one of 11 non-adjacent channels.

As shown in Figure 1.38, the Virtual Channel uses simple 12 bit linear channels with an amplification of 26 in the signal path to the ADC. At the same time, signals from 11 non-adjacent pixels, will be added in a summation (or OR) channel (Virtual Channel) and sent to a ADC. The minimum signal at the high gain Virtual Channel is 3 p.e. / 100 ns (4 LSB), so it saturates at about 3 kp.e. / 100 ns. This channel can be analyzed when any one of the group of 11 saturates. Compared to a normal channel, the noise at the VC will be $\sqrt{11} = 3.3$ times higher, but will be used with large signals only.

- Gain adjustment

A gain control capability is necessary to compensate for the gain spread of the PMT's. On the Analog Board this is accomplished by controlling the value of digitally programmable resistors at the gain stage. The system should be able to accommodate for a factor of 2 variation of the PMT gain above and below the nominal value, which is 26. The minimum and maximum values should be then respectively 15 and 37.

- Test pulse injection

The Analog Board includes two signal drivers of the same type used at the HE. Each driver is used to simultaneously send test signals to the input of 11 adjacent HE channels of the same column. The driver input receives a suitable pulse, which emulates a real fluorescence event. The test pulse can either be internally generated (and driven by the digital board) or provided by an external waveform generator. In the first case, amplitude and width can be remotely programmed as well as its time of occurrence. In addition, the disable feature of the receiver can be used with the correct timing, in such a way that triggering events can be simulated. The pixel selection capability can also be exploited to disable noisy or faulty channels during normal detector operation.

- Test Pattern Generation

This test mode allows evaluation of Second Level Trigger (SLT) functionality without requiring external hardware. A set of analog switches is used to inject a pulse of selectable amplitude and duration into the reference pin of the receiver. In this way, trigger patterns are generated and can be recognized by the SLT.

- Current monitor readout

The background illumination in every pixel determines the DC voltage at each twisted pair cable arriving at the Analog Board from the camera. In absence of background light the pedestal level is about 1.9 V. Before exposing the telescope to the sky, and at the end of each run, readout of pedestals is performed. When exposing to the night sky a deviation (reduction) of the DC level proportional to the illumination seen by the pixel will be verified. Every HE unit has a unique calibration factor determined with approximately 1% accuracy. Every pixel in the camera will have a sensitivity of (61 ± 1.7) mV/μA. The DC level is measured with 16 bit precision using 4 commercial Sigma-Delta ADC chips for all 22 channels in the board. The readout of these devices is performed by a cascaded serial link.

The current monitor system demonstrated extremely high sensitivity which allowed us to clearly identify the signal of dim (mag 5) stars traversing the camera focal surface. Nevertheless, the Critical Design Review committee has recently (August 2001) advised the collaboration not to include the current monitor in the full production to simplify the Head Electronics units. Improvement of the firmware which evaluates the baseline variance might demonstrate adequate sensitivity as well. A comparative test at Los Leones of both systems was recommended by the CDR and will be performed during the last quarter of 2001.

1.2.1.4 First Level Trigger (FLT)

Functionality of the FLT

The First Level Trigger (FLT) is the heart of the digital front-end electronics. Its main tasks are:

- digitize continuously the signals from the Analog Board,
- store the digitized raw data in memory for later readout,
- discriminate efficiently for each channel the fluorescence light above a certain threshold from night sky fluctuations and generate a pixel trigger,
- measure the pixel trigger rate for each channel,
- compensate changing background light intensities through automatic control of the pixel threshold to achieve constant pixel trigger rates and prevent increasing rates of random coincidences,
- transfer the pixel status on demand to the Second Level Trigger (SLT),
- support PC access to raw data memory and internal registers,
- calculate statistical data (Σx, Σx^2) of up to 65 535 ADC values per channel ,and
- provide a digital interface to the Analog Board in order to generate test pulses, set the gain of the analog amplifier stages and/or readout the actual PMT currents.

The organization of the FLT follows the geometrical pixel arrangement in 22 rows by 20 columns. The 440 PMT signals are processed by 20 FLT boards (one board per column) housed in a commercial 19” sub-rack with 22 input channels per board.

The first design of the front-end electronics as presented at the Preliminary Design Review consisted of a 9U high digital motherboard supplemented by two daughter boards, each holding the analog electronics of 11 channels. This design was abandoned due to the limited space on the daughter boards. Instead, the new solution separates the analog and digital part of the electronics into two boards, adjacent to each other and connected through three 50-pin connectors as shown in Figure 1.39. A detailed specification of the interface definition can be found at [25]. In addition, this new concept reduced the production costs and sped up the design, since the boards were developed concurrently and independently by the Italian and German groups.

All functions of the FLT are implemented in FPGA logic for high flexibility, cost-effectiveness and ease of operation. The large number of channels as well as the high connectivity made it impractical to use a single FPGA chip. Instead, functions common to all 22 channels are shared between 4 ‘slave FPGAs’ (Altera Flex 10K50) -- each handling 6 input channels as shown in Figure 1.39. More general functions of the board (like the communication with the PC and the SLT or the interface to the Analog Board) are implemented into a separate ‘controller FPGA’ (Altera Flex 10K100). This assignment of the functions to 5 FPGA is the cheapest solution and still leaves resources for future add-on functions.

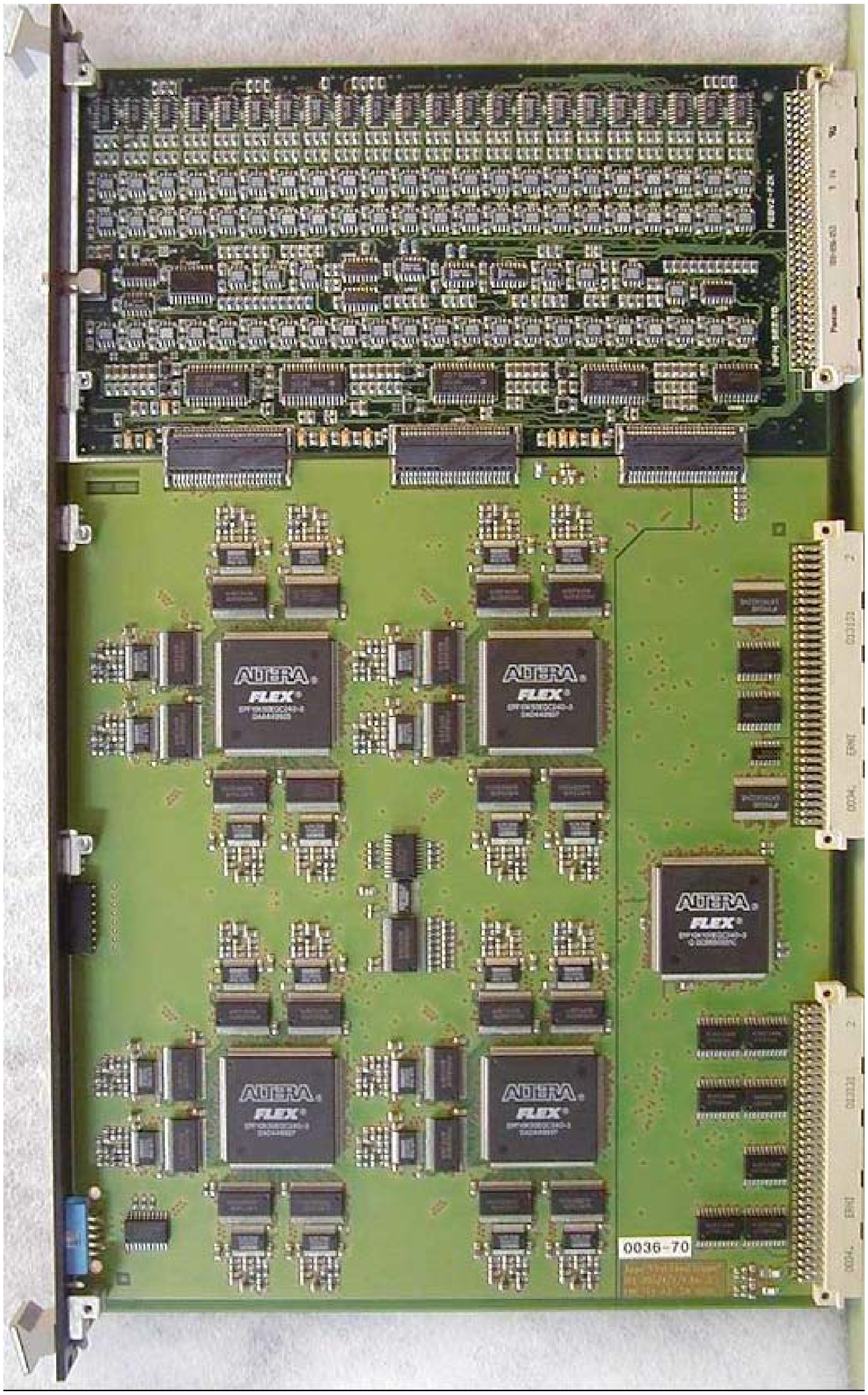

Figure 1.39 Photo of the First Level Trigger (FLT)(bottom) and the Analog Board (AB) (top).

Digitalization and Memory Management

Optimal measurements of the shower profile demand a 10 MHz sampling of the PMT signal. Therefore, a 12-bit ADC (Burr Brown ADS 804) continuously digitizes the analog signals every 100 ns. Together with the 4-bit status for ADC out-of-range, the threshold-changed flag, the pixel trigger state and the pixel status, this information is stored as 16-bit word in conventional 32K x 16 bit SRAM's. The address space of each RAM is divided into 32 pages of 1024 words as shown in Figure 1.40. For the final design we are considering use of 64K x 16 bit memories, as these are more common in the market and despite the bigger size they are lower in price. A drawback is a ca. 10% higher power consumption, and some small changes in the SLT to support 64 memory pages.

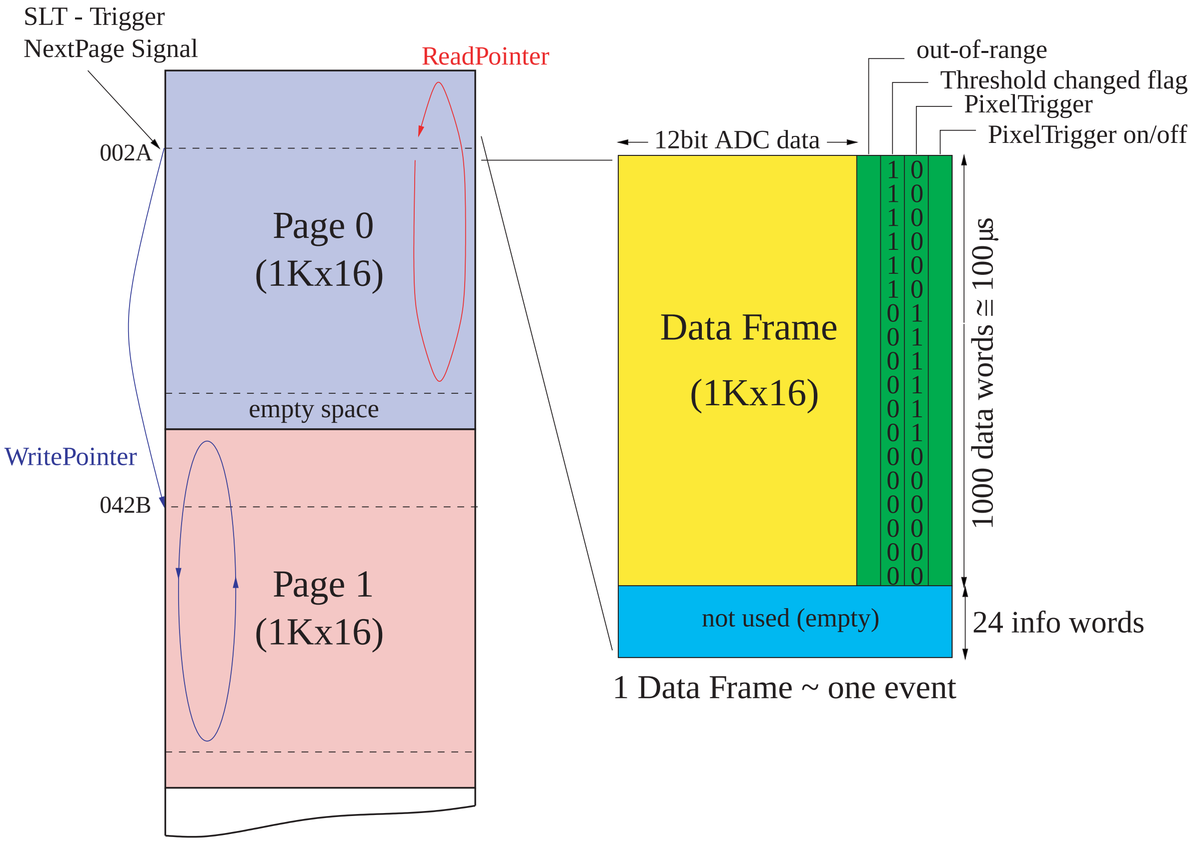

Figure 1.40 Memory architecture and data format of the FLT.

As long as there is no trigger generated by the SLT each page works as a circular buffer memory to hold the ADC values of the last 100 µs. When the SLT finds a track all boards synchronously switch to the same new page address provided by the SLT. By utilizing both slopes of the 10 MHz clock the FPGA can initiate read and write operations and emulate an expensive dual-port memory controller. In this way the system can continue to write into the new circular buffer without dead time while the event data is readout under PC control from any memory page.

Pixel Trigger

Another task of the slave FPGA is to build the pixel trigger for each of the associated 6 channels. The ADC values are integrated by calculating the moving sum of the last N samples as shown in Figure 1.41. The theoretical possible improvement of the signal-to-noise ratio for this most simple digital filter by a factor of √N is not achieved as adjacent ADC values are not statistical independent due to the anti-aliasing filter [26]. The default value for N is 10, but it can be set in the range 5 <= N <=16.

To simplify the logic only the lower 10 ADC- bits enter the summation. Overflow and underflow are handled by replacing the 10-bit value at the summation stage with 3FF or 0 respectively.

A pixel is marked as triggered, whenever the moving sum exceeds an adjustable threshold – a 14-bit value unique to each channel. When the moving sum falls below the threshold a retriggerable mono-flop extends the pixel trigger to a time of 5..30 µs. This time is the overlap coincidence time which is common to all pixels and is a programmable variable inside the FLT .

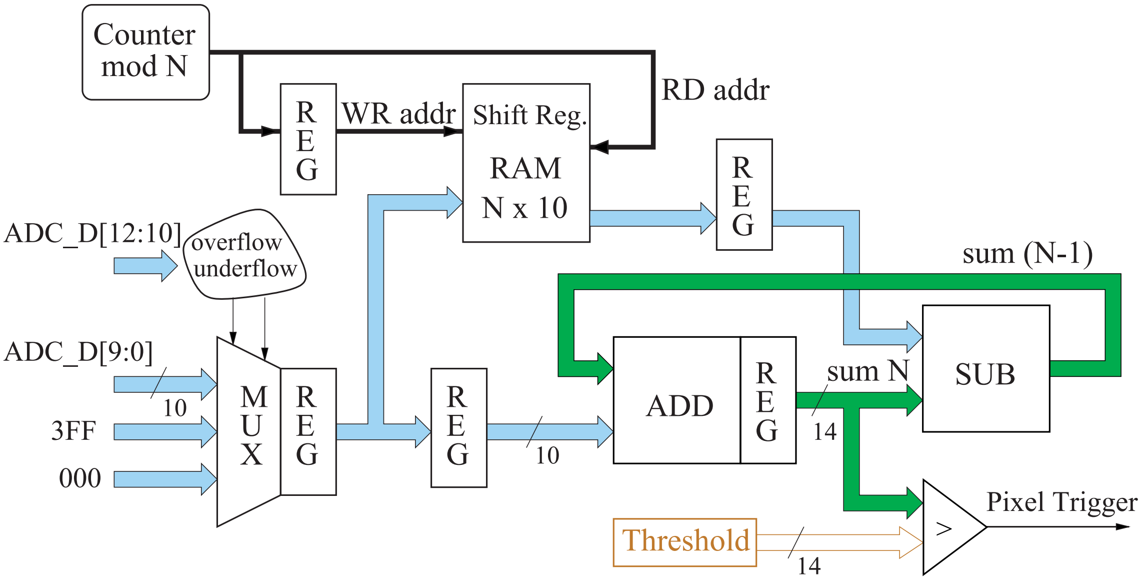

Figure 1.41 Scheme of digital filter for N data words used on the FLT to improve the S/N-ratio.

Hit Rate Measurement

The rate of pixel triggers (or hit rate) is measured in parallel by 15-bit counters for each channel in the control FPGA. Possible measuring intervals are 1, 2, 4, ...32 s long and are derived from the system's GPS-clock. After a measuring period the counter values are normalized to represent the rate in Hz and then stored in internal 10-bit registers to be readout by the Mirror-PC.

Threshold Regulation

The measured hit rate also serves as input variable for the adjustment of the threshold according to Figure 1.42. Six internal 10-bit FPGA registers hold regulation limits L1..L6 to define 7 margins. The latest hit rate is compared with these regulation limits sequentially for all enabled channels. Depending on the result of the comparison, the control FPGA will then cause the slave FPGA to increase or decrease the threshold by up to 15 units. The previous and the actual threshold are held in internal 14-bit registers and are accessible at any time by the PC. In order to relate the time of threshold change to the raw data, the 'threshold-changed' bit will toggle (see Figure 1.40).

To deal with defective and/or noisy PMT's the pixel trigger and the adjustment of the threshold can be disabled and re-enabled separately for each channel from the Mirror-PC.

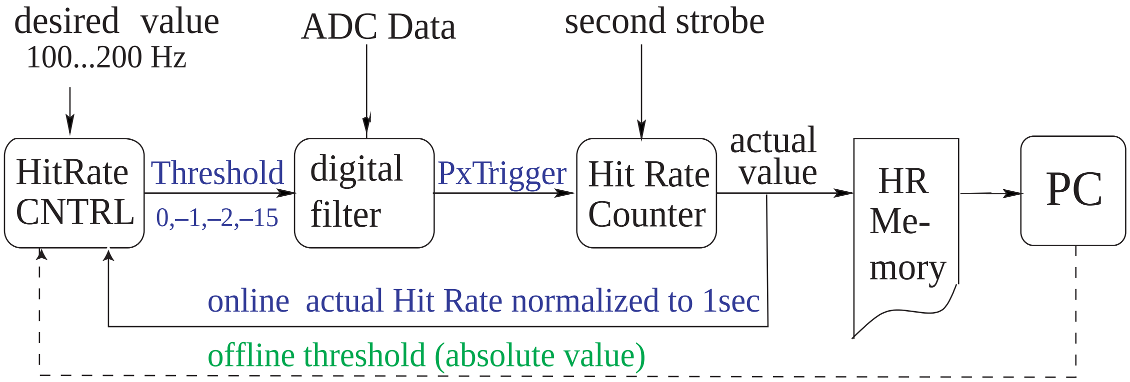

Figure 1.42 Control loop for regulation of hit rate by FPGA (online) and by PC (offline).

Calculation of statistical data

Measurements with the prototype in Rome proved that the DC brightness of the sky is an important experimental parameter that can be derived from the variance of the ADC data. Therefore the slave FPGA calculates periodically for each channel the sum (Σx) and the quadratic sum (Σx^2) of up to 65 535 successive ADC values according to Figure 1.43. With a multiplexer, one out of 6 channels is selected and the programmable offset ZMean is subtracted in order to do the arithmetic with 8 bits plus sign. ADC values with a distance of more than 255 LSB from ZMean are regarded as signals and discarded from the statistics. For all other values we add up all values (x_i = ADC – Zmean) and the square of x_i. The square x_i^2 is calculated using a memory look-up table (LUT). By use of an intermediate register we guarantee synchronous readouts of (Σx, Σx^2) values from Mirror-PC in order to calculate the mean and variance.

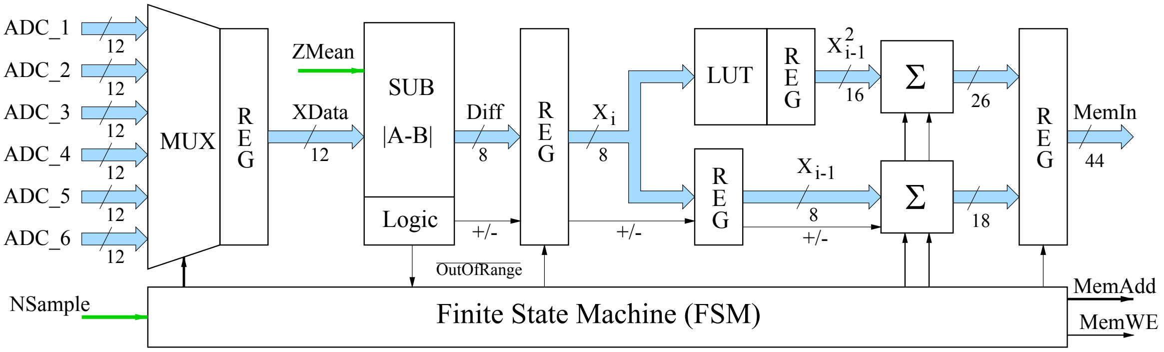

Figure 1.43 Scheme of statistics calculation implemented in each slave FPGA

Internal Bus and Backplane busses

The Analog and First Level Trigger boards are housed in standard 19" wide sub-racks of 9U height (Figure 1.39). They are interconnected via connectors P0 to the analog backplane on the top and via connectors P1, P2 to two VME backplanes in the middle and the bottom of the sub-rack. The analog backplane holds for each slot a VG-Connector to receive the PMT signals through twisted pair cables from the distribution boards. It also supplies 3 analog voltages along bus lines and provides the code for the (geometric) addressing of the FLT boards. Separate layers for the analog ground (AGnd) and Earth reduces the risk of EMC problems.

The front-end electronics uses 2 commercial VME backplanes (J1-type) as a physical layer to build up the 3 digital bus systems shown in Figure 1.44:

- The **Readout Bus** transfers data from the FLT and SLT to the PC or vice-versa. It is based on the VME bus as physical layer, but uses a simpler bus protocol named PBUS+ developed for the KASCADE experiment. The protocol [27] assumes multiplexed address and data lines and provides an asynchronous handshake mechanism for proper synchronization of a single master (the PC) and multiple slave(s) (the FLT and SLT). In addition, an interrupt mechanism (similar to VME) is implemented to inform the PC of event triggers or error conditions.

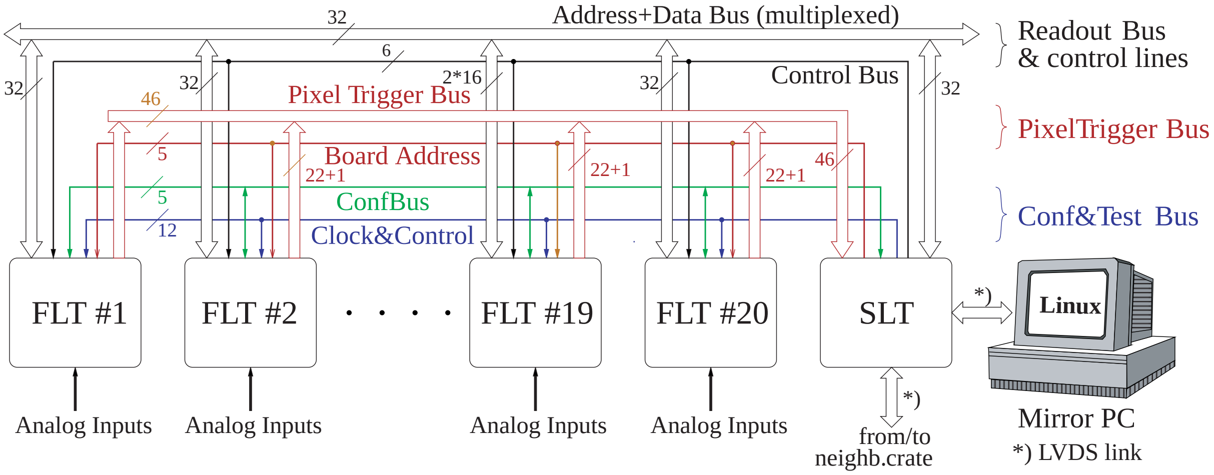

Figure 1.44 Interconnection of FLT and SLT via busses on digital backplane.

- The **Pixel Trigger Bus** transfers pixel trigger data from the FLT to the SLT. Every 100 ns the SLT addresses two adjacent FLT boards via 4 select lines and requests the pixel trigger data (44 bits plus 2 parity bits). The transfer is synchronous with the central 10 MHz clock.

- The **Test & Control Bus** distributes GPS derived clock signals (10 MHz and 1 Second-Strobe), a test pulse signal (see section 1.2.1.10), and signals to configure the FPGA's. In addition, the bus drives control lines like Inhibit (Inh) and Reset.

The controller FPGAs of the FLT and SLT listen continuously to the traffic on the readout and data bus. A coding on the analog bus allocates an ID from 0..19 for each FLT depending on the geometric slot position. If the PC addresses the board by its associated ID, the card will respond to the demanded action.

Most commands access only the internal registers of the controller FPGA. However, commands to readout the ADC data or the actual threshold level require access to the slave FPGA via internal busses. The readout load is dominated by the huge amount of ADC data. To increase the readout speed, two adjacent ADC words (32bits) are readout in parallel per cycle. The design provides two 16-bit wide data busses for inter FPGA communication (see Figure 1.45). These busses are not multiplexed and operate synchronously. Latest measurements showed a data transfer rate of 4 Mbyte/s on the PBUS+ and a event rate of 2 events/s with full pixel data readout.

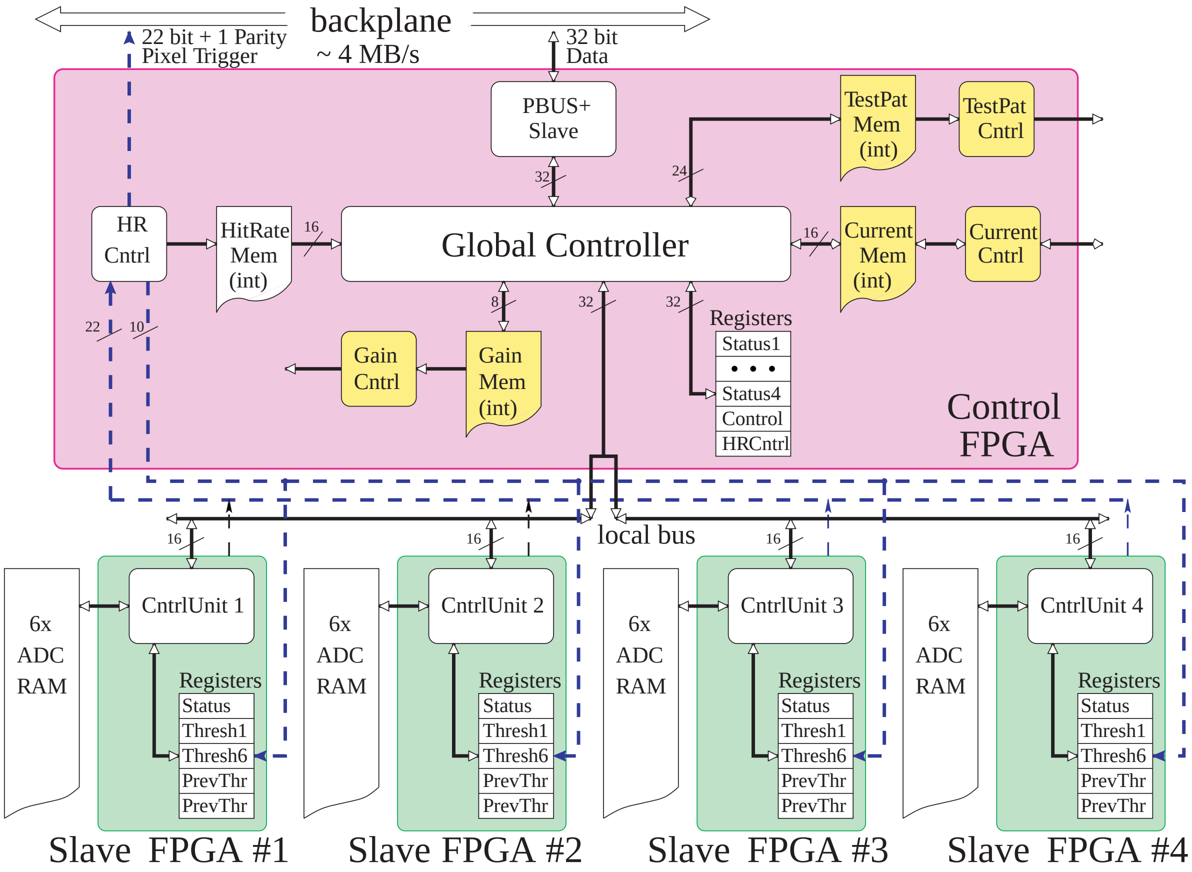

Figure 1.45 Structure of FLT: A local bus interconnects 4 slave FPGAs with the controller FPGA

Inhibit Signal

A centrally distributed inhibit-signal (Inh) (see 1.2.1.7) starts and stops the measurement for all pixels simultaneously. If the signal is present, no ADC data is stored in the buffer and pixel memory, but hit rate measurement, threshold adjustment and access by the PC is left unaffected.

The experience with the first 6 prototype FLTs proved that disabling the ADC clock signals does not reduce the power consumption of the units. The original design idea for a standby mode during idle times was therefore given up.

Digital functions for the Analog Board

Instead of using individual HV channels for each PMT, groups of 44 PMT's will be connected in parallel to the same high voltage source and the cost for a multi-channel high voltage supply are saved (see section 1.2.1.8). The drawback of this solution is that a programmable gain amplifier in the analog chain (see 1.2.1.3) is needed to balance out gain variations of individual tubes. The adjustment of the gain is based on digital potentiometers of type AD 8403. The controller FPGA drives a protocol to transfer a 10-bit value into any of these devices.

The prototype design allows us to monitor the DC anode current of each PMT (see 1.2.1.3). The digitalization of the current monitor (CM) signal is performed on the Analog Board by means of four sigma-delta ADC chips (AD73360). The controller FPGA supports a protocol to write into the AD73360 internal registers and to receive the converted current values.

During the early prototype phase we decided to use the virtual channel (VC) concept to adapt the 15 bit dynamic range to the 12-bit ADC resolution. The flexibility of the control FPGA allowed us to support also the compressor option of the first Analog Boards. The same is true for the control of test pattern generator (see 1.2.1.10), which is only available since version 2 of the AB. The controller FPGA drives switches for the test pattern generator on each channel.

1.2.1.5 Second Level Trigger (SLT)

The pixel trigger generated for each channel of the 20 FLT boards are read via the backplane into one Second Level Trigger (SLT) board per sub-rack. The functions of the SLT are shared between two FPGAs of type 10K100: the "Trigger FPGA" (T-FPGA) and the "Controller FPGA" (C-FPGA). They are both connected to a dual-port RAM, which works as a circular memory to store pixel trigger and other trigger information.

Functions of the T-FPGA

The task of the T-FPGA is to generate an internal trigger if the pattern of triggered pixel looks like a straight track produced by fluorescence light. The algorithm of the T-FPGA regards as a straight track the 5 fundamental topological types of pattern shown in Figure 1.46 (top) and those created by rotation and mirror reflection (in Figure 1.46 bottom).

Many tracks will not pass through the center of the pixel and the PMT may not record enough light to trigger. To allow for this situation and to be fault-tolerant against defective PMT's the algorithm requires only 4 triggered pixels out of the 5-fold pattern mentioned above. Taking into account that identical 4-fold patterns with a gap can originate from different 5-fold hole combinations, there are 108 different pattern remaining - so called pattern classes.

Instead of checking the full matrix for all 108 classes at once – which would be 37163 combinations – we have implemented a pipelined mechanism (see Figure 1.47), which searches for tracks on a smaller 22x5 sub-matrix. Every 50 ns the T-FPGA reads the pixel trigger of a FLT (22 pixels + parity) into a pipelined memory structure. While the full matrix is scanned in this way within 1 μs, a coincidence logic simultaneously analyses the contents of the pipelined memory structure to find track like patterns. It consists of 2102 4-input AND gates to check all patterns followed by OR gates to group combinations of patterns belonging to the same pattern class. A decoder evaluates from this a 7-bit result R and a class multiplicity m_c with the following meaning:

(a) if R=0, then there was no pattern found and $m_c = 0$,

(b) if 1<= R<= 108, then the logic has recognized at least one pattern of class number R and $m_c = 1$,

(c) if R= 127, then the logic found patterns of more then one class, i.e. $m_c >=2$.

In cases b) and c) an internal trigger signal is generated which is further processed by the C-FPGA.

The pixel memory

To avoid finding the same pattern twice, the T-FPGA logic demands a valid trigger in the leftmost column of the matrix. The pixel triggers of this reference column, a parity error bit, the status of the external trigger, the trigger status of adjacent telescopes, and the result R are stored in the pixel memory every 50 ns. This information is found to be most useful for the subsequent software trigger stage as it summarizes all necessary information to reject random triggers without the need for time-consuming raw data readout.

As the memory must be accessible for R/W independently at 20 MHz we use a dual-port, synchronous RAM of 64K x 32bit, which is divided in 32 memory pages of about 2000 words. This is the same organization as the circular memory in the RAM's of the FLT. As the page number of the pixel memory is always synchronous with the FLT page number, the memory management and readout is simplified.

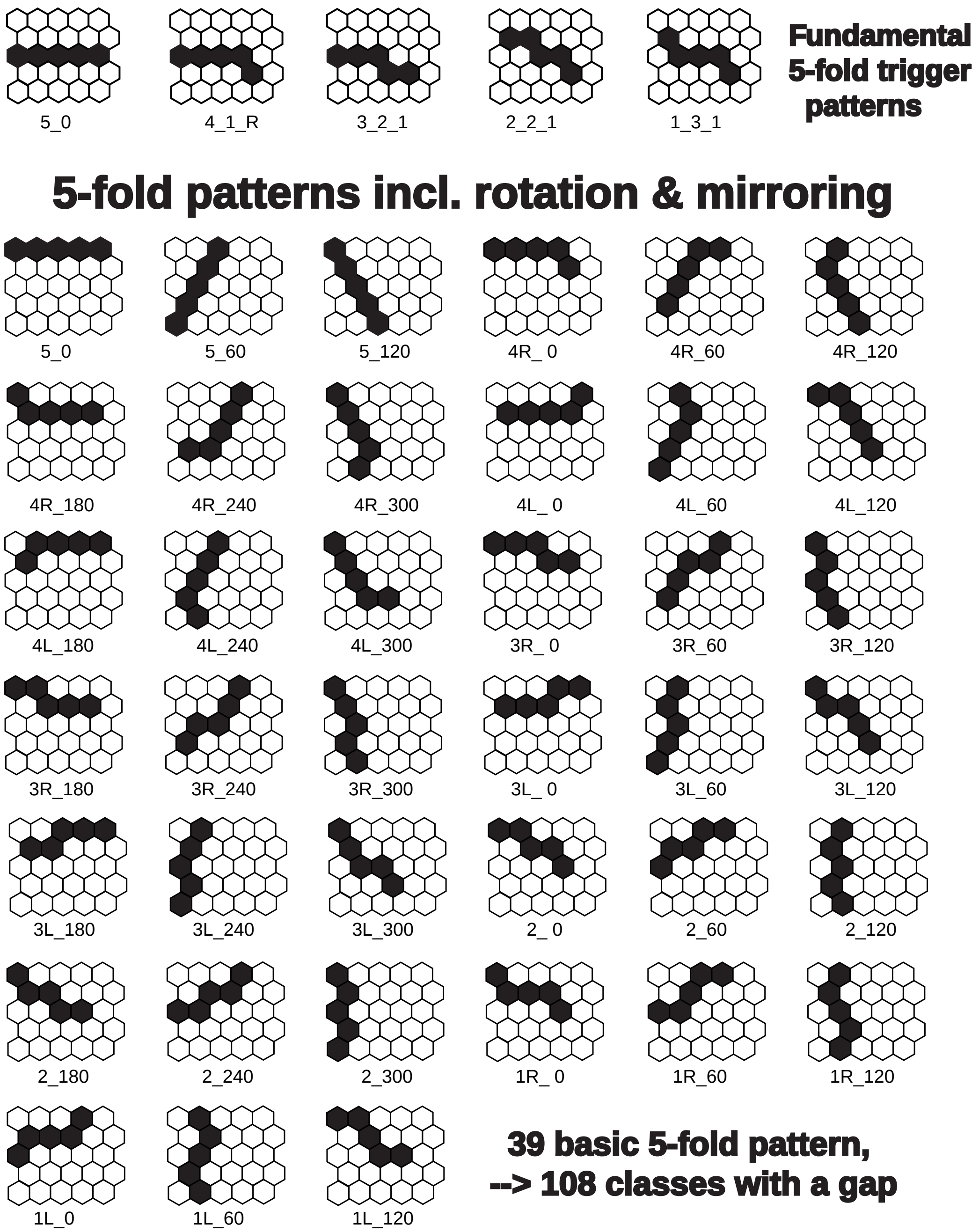

Figure 1.46 Fundamental types of 5-fold pattern (top) and all 39 basic pattern after rotation and mirror reflection (bottom)

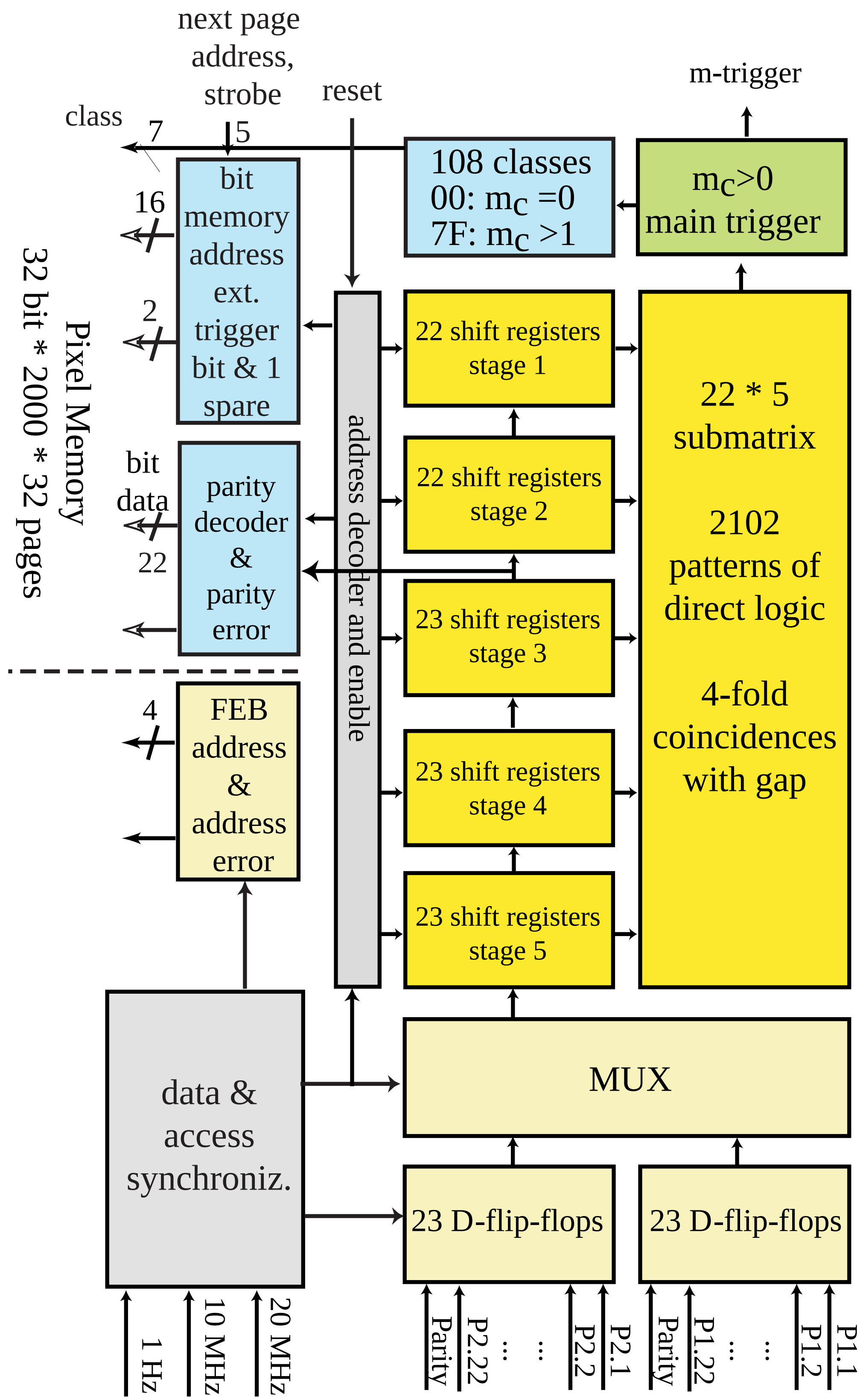

Figure 1.47 Pipeline architecture of the SLT T-FPGA

Functions of the C-FPGA

The C-FPGA is responsible for the following tasks of the SLT board:

- System synchronization: The SLT receives from the Clock Control Board (CCB) the 1s-strobe signal and the 10 MHz clock. These signals are distributed over the bus to the FLT boards and the T-FPGA to synchronize all system parts. Different delays of the FPGAs have to be compensated.

- Handle 5 different trigger sources in the trigger logic:

  1. internal triggers (ITrg) from the T-FPGA,

  2. triggers from the adjacent left and right telescope,

  3. external trigger (ExTrg) centrally distributed through the CCB,

  4. and software initiated triggers from the PC.

  When any of these triggers is present for the first time (and not disabled by the trigger mask register), the C-FPGA waits for a programmable time, e.g. t_l=70 µs. All further triggers during this waiting time are regarded as part of the same event. When the waiting time ends a next-page-signal (NxPg) is distributed to the FLT and T-FPGA to cause all cyclic memories to switch to a new page address.

  In addition ITrg signals are distributed to the adjacent left and right telescopes if pixels of the outermost 4 columns are involved. These systems can be programmed to acccept them as a trigger source even when they have no local internal trigger. In this way we solve the problem of how to trigger on short tracks across telescope boundaries.

- Time management: The C-FPGA keeps a 32-bit counter for the absolute time, which is preset at run start by the Mirror-PC with the number of seconds since 1980 [28]. It is incremented every second on arrival of the 1s-strobe. Another counter holds the sub-second time: 14-bits are used to code the number 0..9999 of 100 µs steps, 11-bits hold the number 0..1999 of 50 ns steps inside a 100 µs frame which represent the address used to write to the circular memories. The C-FPGA provides for each memory page internal registers storing the value of these time counters at the time a NxPg signal is generated and the first trigger occurred. For each trigger source participating in the event a control bit is stored.

- Memory management: A status bit defines any of the 32 memory pages to be either empty (=0) or full (=1). Based on this information, a decoder finds the lowest empty page address to be used as new page at the NxPg signal. The bit is set to 'full' for the old page with the NxPg signal. It is reset to 'empty' by the PC after readout of the raw data or in case of event rejection by the software trigger. In addition, the PC can set the status permanently to 'full' for those pages which are found to have faulty memory locations.

  If all pages are already full the data writing in SLT and FLT memory is stopped via an internal inhibit signal. When any page is set free by the PC, the data taking continues.

- Response to external trigger signal (ExTrg): The status of external light sources is coded in the external trigger signal and always stored in the pixel memory. The trigger logic can be programmed for the following modes:
  - normal: the ExTrg-bit will be recorded as usual, but the trigger is left unaffected.
  - inhibit: during the presence of ExTrg all internal & external triggers are inhibited.
  - active: every ExTrg signal acts like an internal trigger.
- Interrupt generation in case of:
  - a valid trigger is found, i.e. a NxPg is generated internally, or
  - the experiment is stopped, because all 32 memory pages are full, or
  - a parity error occurred reading the pixel triggers from the bus, or
  - receiving interrupts from any FLT, or
  - some slow control parameters are out of range.
- Slow control functions: The C-FPGA is connected to a multiplexed 8 channel 12-bit ADC (Max 530). The ADC measures periodically 5 analog supply voltages and the signal of 3 temperature sensors. The values are monitored to stay within individually programmable margins for each channel. They are accessible as well by PC and can be stored with the raw data.
- Test pattern generator: A part of the test pattern generator (see section 1.2.1.10) is implemented in the C-FPGA logic. The logic reserves memory space used to generate a chain of timing signals (TPuls) which start & stop test pulse generation on the FLT boards. A DAC (Max 197) is interfaced and used to generate a DC level equal to the amplitude of the pulses.
- PBUS+ slave controller: The SLT has to respond to the PBUS+ protocol to allow the PC access to the pixel memory and internal registers.
- Configuration EPROM: All FPGAs on the SLT and FLT boot in parallel at power up or on demand from the PC. The booted firmware is stored in 4 serial accessible EPROMS located at the SLT. A temporary overwrite of the booted firmware is possible with a special cable via the JTAG connector on the SLT or FLT front panel. At the moment an update of the boot EPROM is only possible via JTAG on the SLT.

Future options for the SLT

We are considering implementing a CPU board on the SLT with the full functionalities of the Mirror-PC. In this case the CPU card would boot from the network and Mirror-PCs would no longer be needed. The advantage of this concept is a cheaper, faster and more simple readout. On the other hand we have to prove that this CPU card does not increase the noise on the FLT boards and we would probably need an extra digital +5 V power supply.

1.2.1.6 Interface to PC via microEnable board

The PC accesses the front-end sub-rack via the microEnable board, which is commercially available from Silicon Software. The board is a PCI plug-in card with a single FPGA of the Xilinc XC 4000 series, 2 Mbyte fast SRAM and the ability to plug in self-made daughter cards. The description of the board with the specification is found at [29].

For our purpose we have developed a host transceiver module (HTXM) -a small daughter board, which contains the drivers/receivers for the LVDS twisted pair lines connecting the HTXM module with the SLT board. The protocol for data transfer between the front-end sub-rack and the PC will be the PBUS+ protocol as mentioned in section 1.2.1.4 (Internal Bus and Backplane busses).

The microEnable is sold with drivers for LINUX and WindowsNT. To work as the PBUS+ master controller the Xilinc FPGA has to be programmed in the VHDL or CHDL programming language. The correct operation as the PBUS+ master is verified by transferring data between two microEnable cards plugged into the same PC. Thereby, we can test other functions like interrupt handling, block mode transfer or data compression.

1.2.1.7 Clock and Control Board (CCB)

The clock and control board (CCB) will be used to distribute (TTL) timing and control signals among all telescopes of the same eye station:

- the 1s-pulse and the 10 MHz signal from a GPS clock module,
- the external inhibit signal (Inh) created on demand by the Slow Control System to start/stop the experiment and
- the external trigger signal (ExTrg) to indicate times during which the calibration system has produced light by a laser or Xe-lamp or signals are induced by a pulse generator.

The signals are transferred from the CCB to the front-end sub-racks via 15 m long twisted pair cables using low voltage differential signal drivers (LVDS) as shown in Figure 1.48. The LVDS technology avoids inter-telescope ground loops due to differential signals.

For the prototype and for test systems we will use the receiver GPS 167 from Meinberg [30], which has already been used successfully in the KASCADE experiment. However, for the final experiment we must use a GPS clock on which the evaluated satellites can be demanded to be the same as those used by the surface detector (SD). This guarantees that surface stations and FD always derive signals from the very same satellites and the relative time shift ΔT between both detector systems fulfils the requirement of $\Delta T < 120$ns.

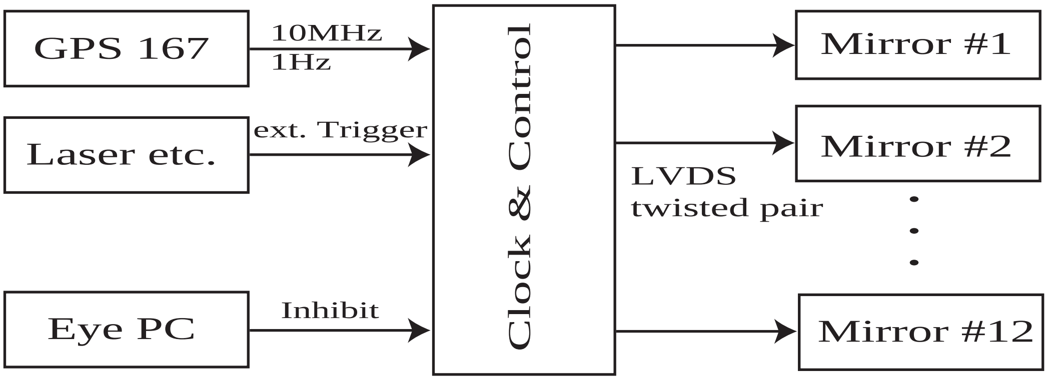

Figure 1.48 Connections of the CCB to GPS clock, front-end sub-racks, slow control and laser.

1.2.1.8 HV/LV Power Supply System

Overview

The HV/LV power supply was conceived as a modular system serving one eye (six telescopes). The system consists of a crate and multi-channel plug-in modules. The crate is located close to the center of the eye so that cabling with almost equal length arrives at the cameras.

General requirements for 6 telescopes:

N. of PMTs per telescope	440	total no. of PMTs	2640
N. of HEs per telescope	440	total no. of HEs	2640
N. of backplane per telescope	10	total no. of bplanes	60

Power requirements:

+ HV	up to	1150V + 20% max	up to	144μA + 20% max
+ LV	up to	6V + 15% max	up to	39mA + 20% max
- LV	up to	6V + 15% max	up to	11.6mA + 20% max

Power supply grouping:

N.1 Power supply HV line for 44PMs

N.1 Power supply LV line for 44 or 88 HEs

Cables & lines requirements:

HV LINE: about 15 m length ,cable with high voltage isolation

LV LINE : about 15 m length ,cable with min. Req. Ohm/Km resistance

Other requirements:

Modular and expandable system with capability to provide up to 6 telescopes power HV/LV power supply

Interactive interfaces

Low cost per channel

Table 1.5 HV and LV specs (based on real data of 500 observed HE's)

Parameters	**HV=OFF**	**+HV1=914V**	**+HV2=1150V**
+I HVmon. x 1PM	0	144µA	181µA
+I HVmon. x 44PMs	0	6.34 mA	7.97mA
+I HEmon.* x 1HE	15.94mA	34.28mA	39.0mA
+I HEmon.* x 88Hes	1.402A	3.016A	3.432A
-I HEmon.* x 1HE	11.59mA	11.59mA	11.59mA
-I HEmon.* x 88Hes	1.02A	1.02A	1.02A
* With +VHE = -VHE = 6V			

System configuration

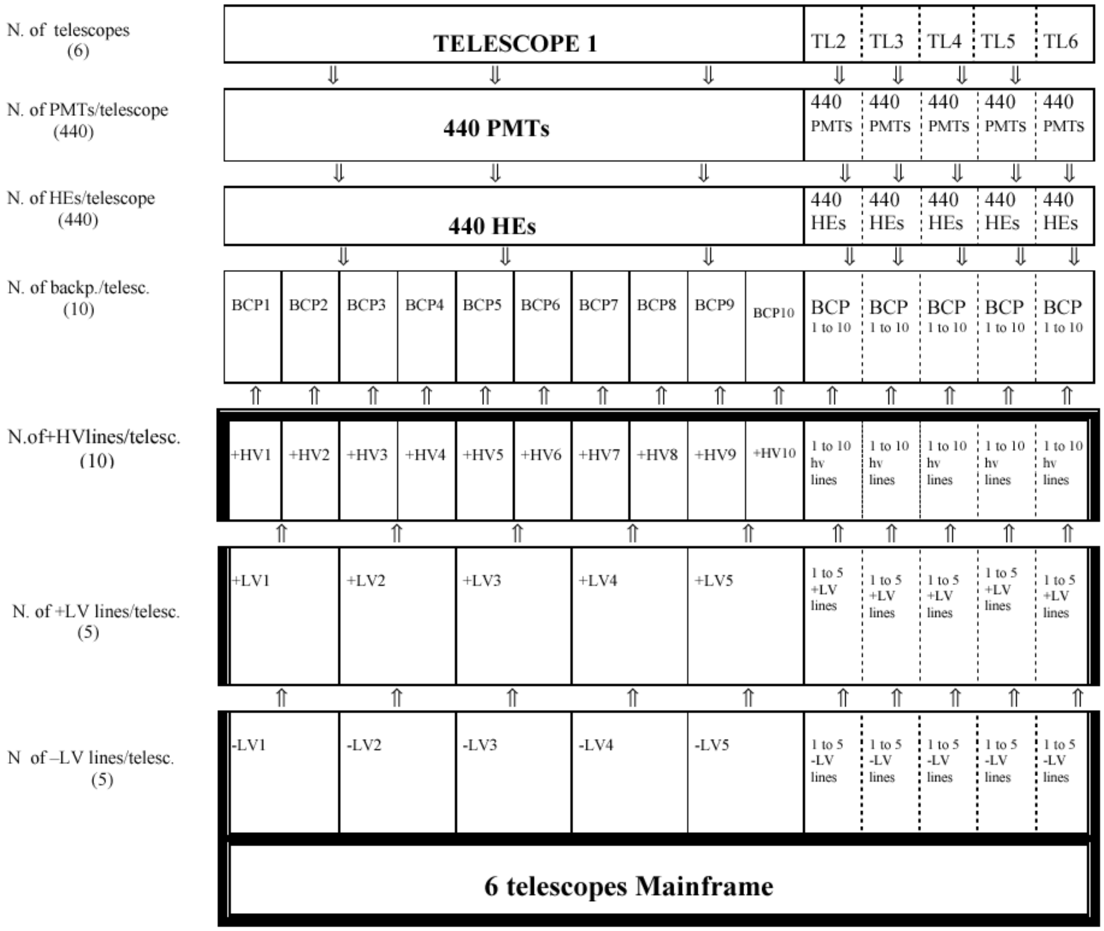

Cable specifications:

HV: 15 m RG58R with 11SHV-50-3-5 or equivalent on both sides

LV: 15 m flat cable 2.5 mm conductors Rmax (20°) 11 Ohm/Km

+LV line : equivalent resistance (15 m) 0.165 Ohm x Imax = 3.432A = 0.566V = max loss voltage line

- LV line : equivalent resistance (15m) 0.165 Ohm x Imax = 1.02A = 0.168V = max loss voltage line

Power requirements:

Table 1.6 Total power requirements (6 telescopes):

+HV	1150V	
+I HV	181 µA x 2640 = 0.478A	
HV x I HV	1150 x 0.4778	550W
+LV	6.6V	
+I LV	39 mA x 2640 = 102.96A	
LV x I LV	102.96 x 6.6	680 W
-LV	6.2V	
+ILV	11.59 mA x 2640 = 30.6A	
LV x ILV	30.6 x 6.2	190 W
Total power requirements		**1420W**

Single cell power requirements:

+HV = GROUPS OF 44PMTs = 181µA x 44 = 7.964 mA x 1150V = 9.16W

+HV = GROUPS OF 88HEs = 39mA x 88 = 3.432A x 6.6V = 22.6W

-HV = GROUPS OF 88HEs = 11.59mA x 88 = 1.02A x 6.2 V = 6.63W

CAEN solution for 6 telescopes

Modules required :

- 1 mainframe SY 1527 delivers 2250 W for the boards, conversion efficiency = 75- 80% = true power 1687 W (at 75%)
- 5 modules HV : use boards model A1735P modified 12 CHs 1.3kV 10mA*
- 10 modules for + and – LV: use boards model A1517 modified 6 CHs 7V 4A*

All the boards are 1:16 slot

* the real maximum power value must be fixed according to the total crate power.

Mainframe

Main characteristics:

- Allow the housing in the same mainframe of both high and low voltage,
- Housed in a 19” 8U crate with allocations of up to 16 single-slot units,
- Remote or locally controlled,
- Live insertion/removal of boards,
- Fast and accurate setting/monitoring of channel parameters,
- One µ-controller per slot, 14 bit resolution,
- Easy interfacing with communication via RS232, TCP/IP,
- Access and control of the system via intranet and telnet,
- On-line technical support available via internet.

Full performance is reported at www.caen.it.

1.2.1.9 Front End Crate Power Supplies

The low voltage supply of the front-end sub-rack

The concept provides 2 digital supply voltages: +3.3 V and +2.5 V and 4 analog supply voltages: +5 V, -12 V and two symmetrical voltages –5.2V and +5.2V respectively. The digital voltages are supplied through the digital backplanes, the analog voltages are injected through the analog backplane (connector P0).

Supply voltage	Imax [A] /sub-rack*	Source	Injection point/ connector
+ 3.3 V digital	< 25	DC/DC converter	backplane J2/P2
+ 2.5 V digital	< 5	DC/DC converter	backplane J1/P1
+ 5 V analog	< 20	DC/DC converter	analog backplane P0
-12 V analog	< 0.5	DC/DC converter	analog backplane P0
–5.2 V analog	< 12	DC/DC converter	analog backplane P0
+5.2 V analog	< 12	DC/DC converter	analog backplane P0

Table 1.9 Overview of supply voltage, maximum current, source and injection point (* latest measurements at full activity).

The choice for the low power supply system is mainly influenced by the need for high reliability, good electric performance, ease of maintenance and a reasonable price/performance ratio. The most important electrical specifications are a low ripple/noise for the analog supply and a high thermal efficiency for the digital supply.

We have selected the LAMBDA JWS 600-48 power supply (220V in/ 48 V out) to generate intermediate 48V DC power which is then transformed by individual DC/DC converters (LAMBDA PH300 series) near the sub-rack to the required voltages. As the efficiency ε of the DC/DC converters is higher than 80% harmful head dissipation is avoided.

Tests with the prototype proved that the ripple/noise specification of the DC/DC converters is also sufficient for the analog supply. At present the mounting of the converters to the sub-rack side walls is unfavorable and leads to long assembly times. In future we will therefore consider using commercial multi-voltage supplies with a lower number of voltage levels in a simpler scheme. We aim to do without the –12 V (used for the HE pulser only), generate the +2.5 from 3.3V separately on each FLT module and unify the +5.2V and +5V to a common +5V.

Grounding scheme

A ground point at the back of the camera body and at the backplane of the sub-rack are used as reference ground points. All ground lines originate from these ground points in a star-like fashion. Different parts of the readout chain are always linked via differential signal lines (LVDS technique) to avoided ground loops. The distribution of the AC power lines inside the FD building also follow a star-like pattern starting from a central supply point. The AC power lines for motors (e.g. for the shutter and the fail-safe-curtain) are kept separate from the 'clean' lines used for the sensitive front-end electronics.

1.2.1.10 Test Systems

The high number of channels, the complexity of the system and the expected time of operation of about 20 years require the use of modern tools for testing and trouble shooting. For this reason we have foreseen 4 independent test possibilities (see Figure 1.49):

- Electrical defects like short circuits and breaks will be detected during production tests. HPE will procure a needle probe for that purpose. In addition, nearly all connections on the FLT are tested with a RAM memory test. In contrast to our original design, we use the boundary scan mechanism [31] only to test the inter-FPGA connections. Therefore - and for loading the FPGA firmware - each FLT and SLT board is equipped with a JTAG connector at the front panel. As there are no JTAG compatible bus driver/ receivers with 3.3V supply available on the market we had to give up our original idea for a full FLT test by means of the JTAG boundary scan algorithm.
- The design provides several light sources for calibration purposes, which can be used to check the full signal path from the PMT to ADC. Details of the calibration are given in section 1.1.9. In addition, the group in Rome has developed the CAT light pulser system. A

matrix of 440 blue LEDs will illuminate the camera, each pixel by one LED pulse with individual timing and amplitude.

- A test pulse injection network located at the head electronics (HE) of the prototype allows us to inject a pulse at the very same node as the PMT. The response of the whole signal channel is therefore tested and disentangled from the response of the optical system, PMT included. The test pulse can have any desired shape allowing emulation of a real fluorescence signal. All other test pulsing systems deliver rectangular pulses with variable amplitude. The injection of test pulses to the HE does not require HV on, allowing operation with ambient lights switched on, which is useful during troubleshooting. (see section 1.2.1.1).

- An independent test pattern generator is implemented on the front-end boards to create pulses variable in width and amplitude at the input of each analog channel. The controller FPGAs will drive one analog switch per channel to couple a pulse into the analog chain. The pulse width, the number of channels involved and the sequence are parameters of the FPGA internal memory, and are determined by the PC in advance. The pulse amplitude is adjustable by a DAC at the SLT board.

  Due to space limitations the first prototype version of the Analog Board did not support the pulse generation. As a pattern generator was needed for trigger tests the Karlsruhe group has developed an *Analog Test Board* (ATB) which can be used in place of the Analog Board. It contained from scratch the switches and drivers necessary to generate pulses and - with version 2 - implements all functions of the Italian AB except for the current monitor readout and the support of the HE pulser. But these missing features are anyway not useful for tests without the connected camera.

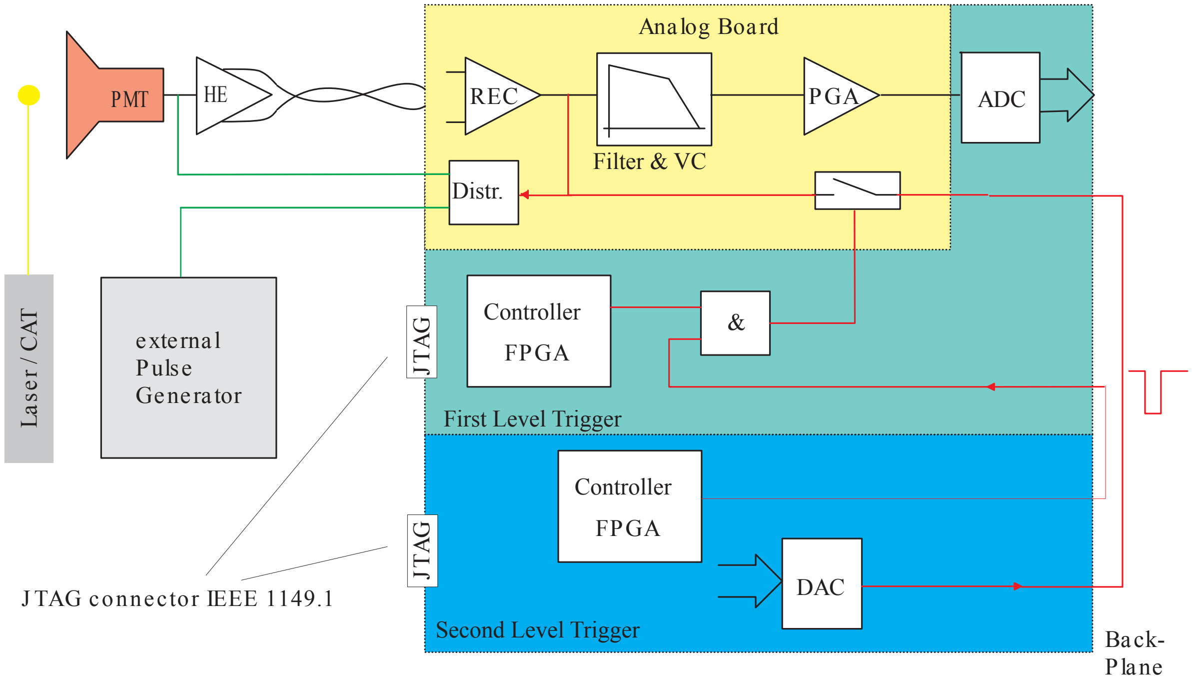

Figure 1.49 Test facilities for the electronics: tests by laser or CAT, by pulser at the HE and with the test pattern generator. Electrical tests are performed during production and by memory tests.

1.2.2 Software

1.2.2.1 Data Acquisition (DAQ)

The FD data acquisition system will be operated in three different modes depending on the way the data are generated and processed:

- processing and acquisition of real experiment data,
- processing and acquisition of real-like data, which are generated by external light sources for calibration reasons (e.g. laser shots, Xe flashes), and
- processing and acquisition of artificial data created by the various test systems.

The two last mentioned scenarios cover all test and calibration situations, if they use at least part of the light and data paths of the FD system.

The expected high event rate during tests and - especially the calibration operation - requires a fast and efficient readout system to transport raw data to the Mirror-PC. Therefore, the readout process is the central process around which all other data path related processes will be grouped. These processes are:

- readout of the data which is done in several steps,
- further processing and filtering tasks (e.g. several levels of software trigger), and
- filling of histograms, monitoring and event displays tasks.

Varying conditions demand a flexible and configurable system. Thus a framework incorporating the basic desired functionality provides skeletons to the application programmer which are easily extendable to achieve the desired behavior. The readout task, in addition, has different readout schemes which allow for an efficient readout adapted to the respective scenario.

The description of the trigger in the following section covers only the scenario of real experiment data acquisition.

1.2.2.2 Trigger

Every pattern recognized by the SLT will lead to an interrupt at the Mirror-PC. Simulations show that the trigger rate for 4-fold coincidences will be about 0.01 Hz at a coincidence time of $\tau = 20\ \mu s$ and at a mean pixel trigger rate of $f = 100$ Hz. Nearly all of these triggers are random coincidences, which must be discriminated against real showers.

An easy way to improve the SLT trigger decision is to check that all pixels participating in an event follow a space-time progression. For that purpose the trigger software reads the pixel memory contents and determines:

- module numbers of all involved pixels from the pattern class information,

- the time when the pixel has fired given by the memory address, and
- the sequence in time and in space of these pixels.

Events are rejected if the sequence in time and space are different. Accepted events are valid T2 triggers and cause the ADC data of the corresponding pixels and eventually of a certain number of pixels in the vicinity to be read from the FLT memories.

Events classified by the Mirror-PC as T2-triggers are sent to the Eye-PC. They are buffered there for maximum of 10 s and will be finally recorded only if a correlation with the surface array is confirmed by the central data acquisition system (CDAS).

If an event passes an even more stringent test of the space-time linearity (and other criteria like minimum energy, minimum track length to be defined during prototype phase) it is regarded as T3 trigger. In this case the energy of the event is expected to be above 10^{19} eV and the event data will be always transmitted to CDAS and merged with SD data. The logic has to make a decision within 5 s after the trigger has occurred.

1.2.2.3 Monitoring/Test

The monitoring of the detector status is a concurrent task to the readout process. Both have to share the CPU time and access to the FD electronics. Considering the higher priority of the readout we will optimize the configuration during the prototype phase.

Variables of every readout event are filled in histograms for the characterization of the detector, its operation and the data quality. Possible variables are for example:

- 2-dimensional representation of data rates for all pixels (e.g. the FLT hit rate or pixel readout frequency),
- mean energy per module or the total energy measured in units of ADC channels,
- absolute or relative time of the pixel hits,
- information stored in the pixel memory,
- threshold or other PMT specific variables.

The recorded histograms are available for online inspection and are also transferred to the central campus for storage and analysis. There an operator compares them with reference spectra and starts the necessary actions. When sufficient experience on the handling and judgement of these histograms has been gained automatic procedures will be applied on them in a later step.

1.2.2.4 Hardware Level Software

In the present design the library "fdhwlib" provides access to all features of the front-end electronics. The library is organized in three layers: the transport layer (PBUS), the register model and the application programmer's interface. The advantage of this layered architecture is that details of the actual implementation, like the register model or the coupling of the hardware, can be modified with fewer side-effects on the application programs.

The transport layer is defined according to the specification of the PBUS+ protocol. Main functions are read and write operations in single and block mode to registers and memory in the electronics. Semaphores synchronize the access of different processes. To allow a flexible use, this layer can also be accessed remotely using the pbus-daemon. This architecture enables us to use diagnostic tools remotely during normal operation of the DAQ system.

The register model allows us to steer all functions of the electronics easily. It is used for hardware tests, diagnostic tasks and to implement the application programmer's interface. The graphical diagnostic monitor is based on this layer.

The third layer provides the interface for the DAQ system, monitoring and other processes. The interface is designed according to the physical function of the camera. It is not necessary to know any details of the register model and the large variety of hardware test features is omitted.

1.2.3 FD Telescopes Control-System (Slow Control)

The operation of each Fluorescence Detector Telescope (FD-Telescope) has to be carefully controlled and supervised for safety reasons. This is the task of a separate control computer – the Field PC. It monitors and records selected variables, the status of devices, sensors and actuators, which are all part of the Slow Control System (SCS). The monitored data are stored in a database to facilitate access of other experiment computers, e.g. of the DAQ system. An application program running on the Field PC ensures that the experiment is only operating at safe environmental and valid infrastructure conditions.

1.2.3.1 Which parameters are to be monitored and controlled?

The SCS should monitor and supervise devices and installations in the telescope bays and in the telescope building. These are for each telescope bay:

- the shutter motors and the associated end switches,
- the fail-safe-curtain with its motor, magnetic brake and end switch,
- an indoor light sensor located close to each camera,
- switches for the AC power of the Mirror-PC and of the front-end sub-rack, and
- the UPS system of the shutter motors.

In addition the following devices and services are supported for the overall system of one building:

- status sensors for the 3 doors to the telescope bays,
- measurement of the indoor and outdoor temperature,
- interface to the HV system, especially control of the HV-interlock signal,
- interface to the LV system (not for the prototype),
- control of the AC power for the roof lights,
- nearby weather station (wind speed, humidity) and outdoor light sensor,
- interface to GPS clock to record time & date information and the 1s-strobe,
- control of the inhibit signal (Inh) to start & stop the DAQ on demand by Eye-PC,
- status of the central UPS for the computers and LAN system.

1.2.3.2 Technical implementation of the SCS

The sensors and actuators to be controlled are spread widely over the whole building. For practical reasons and to minimize the cabling effort we have implemented an electronic network controlled by the Field PC. It is the same approach as is widely used in industrial automation, the so called *fieldbus* technology. The fieldbus connects the controlling Field PC and its *programmable logic controller* (PLC) with peripheral input/output units. These I/O units are connected either directly via the fieldbus or via so-called *intelligent terminals* [32].

The advantages of the fieldbus concept are manifold:

- the use of commercial components avoids long development times,
- industry proven systems and components have a guaranteed reliability during the 20 years of operation,
- standard hardware interfaces can be used for many commercial sensor types and are installed very simple,
- debugging tools and test facilities are available.

As a basis for our development we had installed in Karlsruhe a Slow Control Prototype System. It used a PROFIBUS [33] masterboard as standardized in accordance with "Europäischer Feldbus Standard" (EN 50170) to establish the fieldbus connection and the Profibus/DP protocol (sensor- actuator applications) as a protocol profile. The principal setup of this system is shown in Figure 1.50. Special bus terminals connect the sensors and actuators to a *terminal bus* (K-Bus). A Fieldbus-Controller routes the K-Bus to the fieldbus.

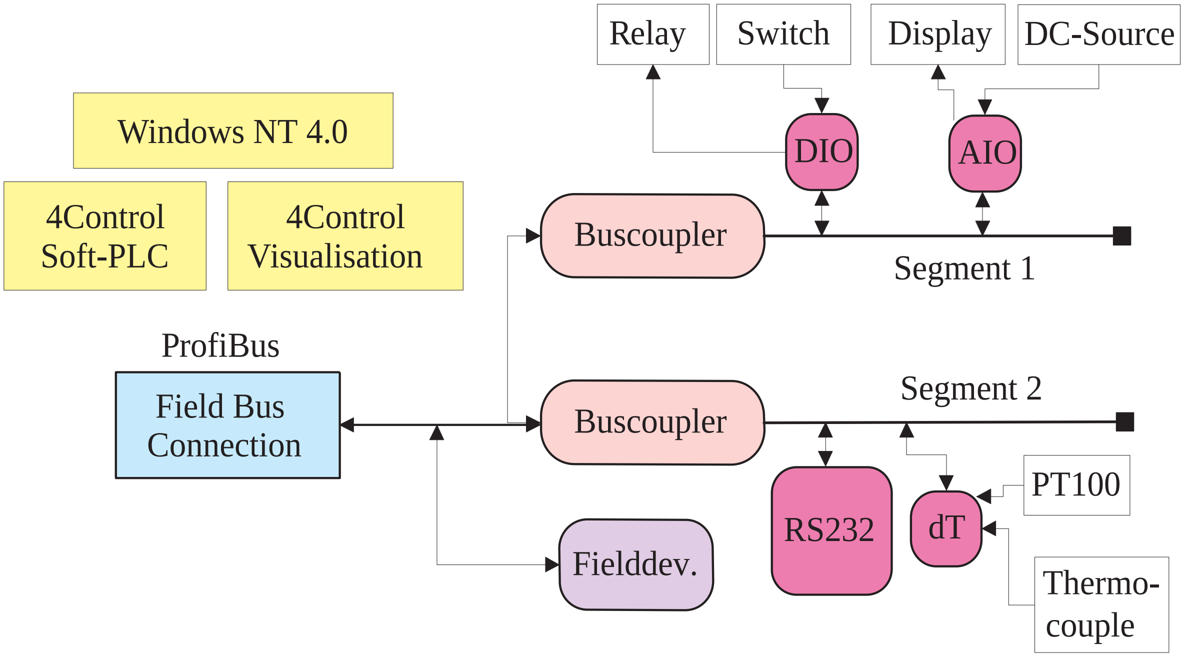

Figure 1.50 Configuration of the Slow Control Prototype Systems.

The positive experience with the prototype system was transferred into the design for the Slow Control System in Los Leones. We use the same development software and the already proven bus coupler (Beckhoff 3100 series) with I/O terminals of the following types:

- digital input terminals (24V or 5V; 2- or 4-wire mode),
- digital output terminals (24V or 5V, relay outputs (AC 230V); 2- or 4-wire mode),
- analog input terminals (differential +/-10V or single ended; differential 0 to 20mA; thermocouple and resistive temperature devices (RTD) inputs),
- analog output terminals (0 to 10V; +/-10V),
- terminals for Communication (RS232; RS485) and
- system terminals (converter 24V/5V; diagnostic and end terminals).

The modular design causes a fine granularity in the I/O system, desired for a first prototype. It allows us to extend the system with additional components as needed. In every segment the functionality of I/Os can be different. However, we install components of equal functionality in each bay and one or two extra segments for more general functions.

Development Software

As the hardware of the SCS are commercial components, the main effort goes into the development of the application software. We use the development software 4CONTROL [34] provided by Softing GmbH in Haar near Munich. 4CONTROL is a Win-NT based software system for the control, programming, operation and monitoring of common technical processes in production and process automation. The package includes the following features:

- real time capable Programmable Logic Controller (PLC) under Windows NT 4.0,
- IEC 1131-3 conformable programming and implementation system for structured text, function block diagram, sequential function chart and JAVA (as IEC 1131-3 extension) as programming languages,
- Intra- and Internet based instrumentation and visualization,
- auto-generation of images for operation and screen information,
- software interfaces to other applications, especially the OPC Interface [35], the SQL-Database Interface and open file formats (ASCII).

Detailed information can be found at http://www.4control.de/. For IEC 1131-3 standard refer to [36].

Most important for the SCS is that the software allows remote access to the process status of the Field-PC via LAN for remote operation, maintenance, alarm management, and visualization. The data exchange with computers over heterogeneous networks (LINUX) is possible.

1.2.3.3 Safety aspects

The main tasks of the SCS relevant to safety are:

- Protect the camera against damage due to high light exposure. It must be ensured that during measurements at HV = on conditions:
    1. the bay roof illumination cannot be switched on,
    2. the HV shuts down (HV-interlock), if the doors to the telescopes are opened or the light sensor detects a high light level and
    3. the shutters cannot be opened during day light.
- Protect the telescope against bad weather and direct sunlight. It must be ensured that the shutters are closed during wind speeds above a level that may destroy the aperture system. As direct sunlight would damage the camera (even without HV) the shutters must be closed or the failsafe curtain must fall down.
- Safe operation of the computer and shutter system, if the main AC power fails. The SCS and the computer system are protected by an uninterruptible power supply (UPS), which must ensure that in the case of a power failure the Mirror-, Eye- and Calibration-PCs shut down properly and the shutters are closed. The SCS system will stay in operation as long as possible, but must shut down itself before the UPS batteries are totally discharged. A safe power-on boot procedure must be established. For a safe boot of the computer system a certain UPS capacity level is mandatory.

Only a very reliable SCS system can fulfill its tasks. The components of our system are in operation in industrial production and plants for many years. They are not approved to military or medical grade and aerospace projects. However, by selecting the hardware carefully we can achieve a very high reliability. The Field PC from Softing GmbH has for example a meantime between failure (MTBF) of 8 years. More information about safety concerns in automation is given in [37].

1.2.4 Computing Facilities

The selection of the computing facilities for data acquisition and processing are strongly influenced by the need for scalability (to 6 or 12 telescopes), reliability during 20 years lifetime and remote controlled maintenance. All these requirements are fulfilled by commercial PCs with a good performance/cost ratio.

The chosen system consists of an Eye PC connected to 6 or 12 Mirror-PCs via a LAN subnet. Despite the rather low data rates of < 1 Mbyte/s during normal experiment conditions, this network is kept separate from the Eye network connecting the Eye PC with the telecommunication station and the slow control PC (see Figure 1.25).

1.2.4.1 Mirror-PC

The Mirror-PCs are commercial PCs running with an Intel P5- 233 MHz CPU and 256 Mbyte RAM. They operate diskless and with a passive cooling to increase the lifetime. The power supply will be selected to be very reliable. The Mirror-PCs can be switched on and off under remote control.

1.2.4.2 Eye-PC

The Eye-PCs are used for diagnostics and monitoring, short term data storage and the inter-telescope trigger analysis. As they are the only stations (except for the Field-PC) equipped with hard disks they serve as boot and file servers for the Mirror-PCs. In Karlsruhe the boot procedure was successfully tested by a small Eye-PC – Mirror PC test setup.

References

1 G. Matthiae and P. Privitera , “The Schmidt Telescope with Corrector Plate”, Pierre Auger Project Technical Note GAP-98-039, 1998.

2 R. Sato, J. A. Bellido C. and H. C. Reis, “Ray-tracing of the Schmidt Camera with Corrector Plate” Pierre Auger Project Technical Note GAP-99-012, 1999.

3 J.W. Elbert, “The HiRes filter and its effect on the aperture,” in Proceedings of the Tokyo Workshop on Techniques for the Study of Extremely High Energy Cosmic Rays (ed: M. Nagano) p.232, 1993.

4 R. Cester, D.Maurizio, E. Menichetti and N. Pastrone, “Evaluation of Commercial UV Glass Filters for the Auger Prototype Fluorescence Detector”, Pierre Auger Project Technical Note GAP-99-031, 1999.

5 P. Facal San Luis and P. Privitera, "Measurement of the FD camera light collection efficiency and uniformity", Pierre Auger Project Technical Note GAP-2000-010, 2000.

6 G. Matthiae and P. Privitera, "Study of the Philips Hexagonal PMT XP3062 for the FD Camera", Pierre Auger Project Technical Note GAP-99-001, 1999.

7 M. Born and E. Wolf “Principles of Optics”, Sec. 6.4 (Cambridge University Press).

8 H.C. Reis, C.O. Escobar, R. Sato and J.A. Bellido, “A Study of the corrector plates for the Auger fluorescence detector,” Pierre Auger Project Technical Note GAP-99-013, 1999.

9 R.Sato et al.,”Corrector ‘Plate’ with an Annulus Shape” Pierre Auger Project Technical Note GAP-99-014, 1999.

10 J. Castro-Ramos and A. Cordero-Davila, “Design of a Maksutov-Bouwers Camera for the Fluorescence Detector”, Pierre Auger Project Technical Note GAP-99-011, 1999.

11 E. Fokitis, S. Maltezos and E. Papantonopoulos, “Optical Filter Design by the Simulated Annealing Method for the Fluorescence Detector of the Auger Project”, Pierre Auger Project Technical Note GAP-98-022, 1998.

12 J.A. Dobrowofsky et al., Appl. Optics, 31 3784, 1992.

13 E. Anastassakis and E. Liarokapis, J. Appl. Phys., 62 no.8, 1987.

14 M. Ambrosio et al., "The FD camera PMT test system", Pierre Auger Project Technical Note, in preparation.

15 National Institute of Standards and Technology, Calibration Program, Gaithersburg, MD 20899-2330 USA.

16 H. Gemmeke, A. Grindler, H. Keim, M. Kleifges, N. Kunka, Z. Szadkowski, D. Tcherniakhovski, “Design of the Trigger System for the Auger Fluorescence Detector”, contribution to the 11th IEEE Real Time Conference, Santa F e, USA, 1999 IEEE-NSS 47 (2000) 519.

17 S.Argirò et al., Monitoring DC Anode Current from a Grounded-Cathode PMT, Nucl.Inst. Meth. A435,1999 pp. 484-489

18 D. Camin et al., "Fabrication of the First 150 Head Electronics Units - Results of the Acceptance Tests", GAP-99-043.

---

19 D. Camin and V. Re, “Analog processing of signals from the fluorescence detector”, GAP 1999-019.

20 S. Argirò et al, “The Analog Signal Processor of the Auger Fluorescence detector prototype”, Nucl.Instrum.Meth.A 461:440-448,2001

21 B. Dawson, “Amplitude Dynamic Range in Auger Fluorescence Electronics: Update for the Four Eye System at Nihuil”, GAP 99-038.

22 P.W. Cattaneo, “The Anti-aliasing Requirements for Area and Timing Measurements with the Fluorescence Detector Read-out Channel”, GAP 2000-062.

23 P.W. Cattaneo, “The anti-aliasing requirements for amplitude measurements with the Fluorescence Detector read-out channel”, GAP 2000-049.

24 P.W. Cattaneo, “Comparison of Different Solutions to the Dynamic Range Reduction for the Fluorescence Detector Front End Electronics”, GAP 1999-009 and P.F. Manfredi et al., “A bilinear analog compressor to adapt the signal dynamic range in the Auger fluorescence detector”, Nucl. Inst. Meth. A461 (2001) 526-529

25 Specification of Interface between Analog and Digital Board is available at documentation of Auger HPE group. www.hpe.fzk.de/projekt/auger/

26 M. Kleifges et al., “First Measurements with the AUGER Fluorescence Detector Data Acquisition System”, contribution to ICRC conference 2001, Hamburg

27 D. Bormann, FZK internal report, Specification HPE- 285/5/1-4.

28 Auger Collaboration, “Conventions for the Pierre Auger Observatory”, www.auger.org/admin/index.html. Click "Conventions" under "Project management".

29 Silicon Software GmbH at http://www.silicon-software.com ,”The microEnable FPGA-Coprocessor”.

30 The manual can be found at http://www.meinberg.de.

31 The boundary scan mechanism is documented in norm IEEE 1149.1.

32 See for example: http://www.beckhoff.com/english/busterm/default.htm or http://www.beckhoff.com/english/busterm/aufbau.htm

33 Profibus Home Page: http://www.profibus.com.

34 4CONTROL Datasheet, Sept. 99, Version 1.2, Softing GmbH

35 OPC Foundation: OLE for Process Control (OPC) Final Specification V2.0. OPC Foundation, P.O. Box 140524, Austin, Texas, 10/1998 or http://www.opcfoundation.org .

36 Standardization in industrial programming and control: http://www.plcopen.org .

37 Siemens Online Document: http://www.ad.siemens.de/safety. Click Regulations & Standards.